

Optimizing Chemical-Vapor-Deposition Diamond for Nitrogen-Vacancy Center Ensemble Magnetometry

by

Scott T. Alsid

B.S. Physics and Mathematical Sciences, U. S. Air Force Academy (2015)

Submitted to the Department of Nuclear Science and Engineering

in partial fulfillment of the requirements for the degree of

Master of Science in Nuclear Science and Engineering

at the

MASSACHUSETTS INSTITUTE OF TECHNOLOGY

June 2017

© Massachusetts Institute of Technology 2017. All rights reserved.

Author
Department of Nuclear Science and Engineering
May 18, 2017

Certified by.....
Paola Cappellaro
Esther and Harold E. Edgerton Associate Professor of Nuclear Science and
Engineering
Thesis Supervisor

Certified by.....
Danielle A. Braje
Assistant Group Leader, Quantum Information and Integrated Nanosystems
MIT Lincoln Laboratory
Thesis Supervisor

Accepted by
Ju Li
Battelle Energy Alliance Professor of Nuclear Science and Engineering
Professor of Materials Science and Engineering
Chairman, Department Committee on Graduate Theses

Optimizing Chemical-Vapor-Deposition Diamond for Nitrogen-Vacancy Center Ensemble Magnetometry

by

Scott T. Alsid

Submitted to the Department of Nuclear Science and Engineering
on May 18, 2017, in partial fulfillment of the
requirements for the degree of
Master of Science in Nuclear Science and Engineering

Abstract

The nitrogen-vacancy (NV) center in diamond has emerged as a promising platform for high-sensitivity, vector magnetic field detection and high spatial resolution magnetic-field imaging due to its unique combination of optical and spin properties. NV diamond magnetometry has enabled a wide array of applications from the noninvasive measurement of a single neuron action potential to the mapping μT -fields in μm -size meteorite grains. To further improve the magnetic sensitivity of an ensemble NV magnetometer, the growth and processing of the host diamond must be taken into account. This thesis presents a systematic study of the effects of diamond processing on bulk chemical-vapor-deposition diamond. In particular, NV charge-state composition and spin decoherence times are measured for diamonds irradiated with 1 MeV electrons at doses of $1 \times 10^{15} - 5 \times 10^{19} \text{ e}^-/\text{cm}^2$ and thermally annealed at temperatures of 850°C and 1250°C . The study provides an optimal range for diamond processing and shows the quenching of the NV center at high irradiation dosage from the creation of additional vacancy-related defects.

Thesis Supervisor: Paola Cappellaro

Title: Esther and Harold E. Edgerton Associate Professor of Nuclear Science and Engineering

Thesis Supervisor: Danielle A. Braje

Title: Assistant Group Leader, Quantum Information and Integrated Nanosystems
MIT Lincoln Laboratory

Acknowledgments

My time at MIT has been two of the most challenging years of my life, pushing my mental stamina far beyond anything I could have imagined. The support of many individuals, both in the local area and across the country, are the main reason for my accomplishments while pursuing this degree.

All of this would not have been possible in the first place were it not for the support of my sponsors. I am extremely thankful for the United States Air Force for allowing me to pursue graduate-level education for my first assignment as a commissioned officer. I hope to use the many skills I have learned here to assist my future colleagues when I begin my work as a physicist for the Air Force Research Laboratory in New Mexico. I am also thankful for the National Science Foundation and the MIT Lincoln Laboratory for funding my graduate education. The material in this thesis is based upon work supported by the National Science Foundation Graduate Research Fellowship under Grant No. 1122374.

Words alone cannot express how thankful I am for my two advisors, Dr. Danielle Braje of Lincoln Laboratory and Professor Paola Cappellaro of MIT. Having near-zero experimental experience when I started, they patiently guided me through how to take and present data, in addition to valuable life lessons on what being an experimental physicist is like. I look forward to continued mentorship from them.

I am highly grateful for the two technical staff members of Lincoln I frequently worked with, Dr. Linh My Pham and Dr. John Barry. Linh answered the many optics questions I had in my first year and taught me everything I know about characterizing NV centers in my second year. If I ever had a problem with the experiment that despite hours of troubleshooting I could not fix, Linh always knew the right fix and would explain it in a clear and pedagogical way. I will also miss hearing her insightful critiques on several movies, especially those from the DC and Marvel universe. I had the pleasure of working with John my second year, especially towards the end as we attempted to figure out EPR measurements and spend several hours at MIT on the weekends. Watching him troubleshoot the EPR machine and spectrometer taught me valuable lessons on how to take data efficiently and make sure all possible instrumentation errors are accounted for. Most importantly I am

thankful for their constant advice on how to be a professional experimental physicist, from teaching me to focus my attention on what is truly important for my experiment to always challenging me to consider all ways data acquisition/processing can be made more efficient.

I am thankful for sharing a lab bench with Erik Eisenach and one bench over with Christopher McNally. The constant stream of laughter and group lunches made every day at Lincoln worth enjoying. I wish Erik the best as he continues to get a doctorate at MIT and for Chris's future graduate school endeavors. The "graduates" of the Quantum Sensing Laboratory I am also thankful for; the assistance of Hannah Clevenson, Matt Trusheim, and Edward Chen were invaluable during my first year at Lincoln. I'm especially fond of Ed's intensity towards physics, epitomized by his quote "you are always at war with science".

Shifting to the MIT campus, I am unquestionably grateful for the time spent in the Quantum Engineering Group (QEG). I have fond memories of the late-night problem set parties of 22.51 and 8.421 with Calvin Sun and Yixiang Liu. I'm also thankful for the assistance of David Layden in 8.511 and 8.422 during my second year of classes. The insight and welcoming atmosphere provided by Mo Chen, Akira Sone, Ken Xuan Wei, Kasturi Saha, "professor" Alex Cooper-Roy, Ashok Ajoy, and Luca Marseglia made every interaction with QEG something to look forward too. I'm excited to see what research they will accomplish in the future.

Outside of QEG are several other fellow students I enjoyed spending time with. There's no one else I'd rather go through the course 22 modules with than Chris Wink and Malik Wagih. Those also involved lots of late nights trying to understand just what was really being asked in problem sets. I'm also happy to have met Jules Stuart ("153") of the ion-trapping group; I will miss his humor from working on solid-state class work and on MIT in general. Finally, I had the tremendous pleasure of taking both of Professor Wolfgang Ketterle's atomic and optical physics courses; from these I have gained an appreciation for AMO science and a baseline knowledge for my next assignment when I will work with AMO experiments. Professor Isaac Chuang, who co-managed the courses, introduced me to the flipped classroom paradigm with half of the course being on edX, a new and insightful learning experience I will not forget.

I've also been privileged to interact with the Air Force scientific community. I am end-

lessly grateful for the continued mentorship of my undergraduate advisor Lt Col Mario Serna, who helped me keep the bigger picture in mind with regards to MIT and the Air Force. I had the privilege of sharing my research with a few Air Force Research Laboratory sites; I am thankful for being allowed to present my research to Dr. Luke Bissell and Dr. Paul Alsing. I'm also honored that Dr. Spencer Olson and Lt Col Serna were able to listen in to my final thesis presentation from abroad.

Lastly, I am thankful for the wonderful friendships I have made at the MIT Baptist Student Fellowship and the continued friendships from my time at the United States Air Force Academy. And of course, I am extremely thankful to my family back home in Florida, to now include my brother's fiancée. They always encourage me to try harder and redefine what I consider my limits to be. In return, I hope I was able to convince them of the usefulness of the nitrogen-vacancy center!

Disclaimers

The research presented in this thesis is jointly supported by the National Science Foundation and MIT Lincoln Laboratory.

The views expressed in this thesis are those of the author and do not reflect the official policy or position of the United States Air Force, Department of Defense, or the U.S. Government.

This material is based upon work supported by the Assistant Secretary of Defense for Research and Engineering under Air Force Contract No. FA8721-05-C-0002 and/or FA8702-15-D-0001. Any opinions, findings, conclusions or recommendations expressed in this material are those of the author and do not necessarily reflect the views of the Assistant Secretary of Defense for Research and Engineering.

Any opinion, findings, and conclusions or recommendations expressed in this material are those of the author and do not necessarily reflect the views of the National Science Foundation.

This thesis is dedicated to my parents, Mark and Tracey Alsid, and to my brother Brett. I am forever thankful for their love and support.

Contents

1	Magnetometry and the Nitrogen-Vacancy Center	25
1.1	Introduction	25
1.2	Nitrogen-Vacancy Center Physics	26
1.2.1	Electronic Structure	28
1.2.2	Photoluminescence Spectra	29
1.2.3	The Neutrally-Charged NV Center	31
1.2.4	Spin-State Dependent Fluorescence and ODMR	33
1.3	NV Magnetometry	36
1.3.1	Magnetic Sensitivity	37
1.3.2	Optimizing Sensitivity	37
2	Diamond Processing	41
2.1	Overview	41
2.2	Diamond Processing	43
2.2.1	Synthetic Diamond Generation	43
2.2.2	Nitrogen Incorporation	45
2.2.3	Vacancy Production	46
2.2.4	Thermal Annealing	47
2.3	Diamonds used in this Thesis	47
2.4	Conclusion	50
3	Charge State Fluorescence Characterization	51
3.1	Overview	51

3.2	Charge State Dynamics and Magnetometry	52
3.3	Measurement Procedure	54
3.4	Charge State Fluorescence Measurements	55
3.4.1	Total Fluorescence vs. Irradiation Dose	55
3.4.2	Fluorescence Model	57
3.4.3	Total Fluorescence vs. Optical Power	59
3.4.4	Charge State Fluorescence Ratio vs. Irradiation Dose	62
3.4.5	Charge State Fluorescence Ratio vs. Optical Power	64
3.5	Conclusion	67
4	Coherence Time Characterization	69
4.1	Overview	69
4.2	Coherence Time and Magnetometry	70
4.3	Spin-Dephasing Time T_2^* Measurements	71
4.3.1	Measurement Procedure	71
4.3.2	Results and Limitations	73
4.4	Spin-Decoherence Time T_2 Measurements	74
4.4.1	Measurement Procedure	74
4.4.2	Results	76
4.5	Spin-Lattice Relaxation Time T_1 Measurements	78
4.5.1	Measurement Procedure	78
4.5.2	Results and Limitations	79
4.6	Conclusion	80
5	Analysis and Outlook	81
5.1	Overview	81
5.2	Sensitivity Figure of Merit	81
5.2.1	Modelling the Sensitivity	81
5.2.2	Sensitivity vs. Irradiation Dose	84
5.3	Outlook	86

A	Experimental Setup and Calculations	91
A.1	Experimental Setup	91
A.1.1	Overview of the Setup	91
A.2	Fluorescence Calculations	94
A.2.1	Power Density	95
A.2.2	Saturation Power	96
A.2.3	Imaging Region Calculations	96
B	NV Fluorescence Methods and Calculations	97
B.1	Charge State Data Acquisition	97
B.1.1	Measurement Procedure	97
B.1.2	Linear Combination of NV Spectra	100
C	Coherence Time Measurement Procedure	105
C.1	Electronics	105
C.2	Static Magnetic Field Alignment	106
C.2.1	Initial Considerations	106
C.2.2	(100) Diamond Geometry and Initial Field Alignment	107
C.2.3	CAW-ODMR Measurements	108
C.2.4	Laser Polarization-Assisted Field Alignment	109
C.3	Resonant Excitation and Field Projection	112
C.4	Rabi Oscillations	114
C.5	Polarization Time Optimization	115

List of Figures

1-1	The nitrogen-vacancy center in diamond.	27
1-2	Electronic energy level structure of the NV^- center in diamond.	29
1-3	Photoluminescence of the NV center. (left) Diagram depicting the optical and vibrational transitions that occur under optical excitation. Non-radiative decay by vibrational states coupled to the main ${}^3A_2 \leftrightarrow {}^3E$ NV^- transition result in a broad emission pattern from 637 - 800 nm at room temperature. (right) Photoluminescence spectra of the NV^0 and NV^- charge states, normalized to have the same area.	30
1-4	Currently proposed NV^0 energy level structure. The 575 nm ZPL transition is between a proposed spin doublet ground state and an optically excited spin doublet excited state. Experimental evidence also suggests the existence of a metastable spin quartet state.	32
1-5	Two-photon charge state conversion between the negative and neutrally charged NV center. At wavelengths below 477 nm ionization from NV^- to NV^0 is predominantly a one-photon process, as with recombination from NV^0 to NV^- below 422 nm.	33
1-6	Spin-state dependent dynamics of the NV^- center. The $ \pm 1\rangle$ excited states exhibit a higher branching ratio to decay via the non-radiative ISC transition. After decay to the 1E state, the $ 0\rangle$ ground state is preferentially populated, leading to spin polarization. The spin-dependent ISC and optical polarization lead to spin-state dependent fluorescence, where the emitted light intensity under optical excitation maps out the NV^- spin state.	34

1-7	Basic detection of an applied magnetic field through a Zeeman splitting of ODMR spectra. (a) The NV fluorescence is monitored as MW excitation is swept; when the MW is on resonance with a transition between the different spin projections of the 3A_2 state, the fluorescence decreases. (b) An applied magnetic field splits the degeneracy between the $ \pm 1\rangle$ states, giving rise to two ODMR dips. The distance between the dips is proportional to the projection of the field along the NV axis.	35
1-8	Modeled fluorescence data that is typically seen in magnetometry measurements. The contrast α in both curves corresponds to the deviation from the maximum fluorescence level that is caused by applied MW fields and the fluorescence β corresponds to the luminescence signal from the NV ensemble. For the DC (left) scenario T_2^* is a measure of the broadening of the lineshape, while in the AC (right) scenario T_2 characterizes the decay envelope.	38
2-1	The effects of diamond processing on NV ODMR lineshapes. (Left) A diagram of the diamond lattice showing a nitrogen-vacancy center (circled in green) along with other defects (circled in red) that interact with the NV center and broaden its resonance profile, such as single vacancies, substitutional nitrogen atoms, or ^{13}C atoms. (Right) Simulated ODMR curves for (top) a naturally abundant 98.9% ^{12}C diamond and (bottom) a isotopically ^{12}C pure diamond, where the effects of broadening from ^{13}C are eliminated.	42
2-2	Three Element Six standard grade diamonds used in this thesis with the same electron dose subjected to varying annealing temperatures. The change in color is due to the annealing out of different defects at higher temperatures.	50
3-1	Example photoluminescence spectra for Diesel ($1 \times 10^{15} \text{ e}^-/\text{cm}^2$, 1250°C anneal) at 10 mW of laser excitation. The PL signatures from the NV^0 and NV^- charge states are also shown to highlight the contribution of each charge state, as well as the overlap of the two spectra.	53

3-2	Total NV fluorescence vs. irradiation dose over four orders of magnitude for diamonds that underwent (left) 850°C annealing treatment (right) 1250°C annealing treatment.	56
3-3	Total NV fluorescence vs. irradiation dose for all diamonds at (left) 100 μ W of laser excitation before the objective and (right) 10 mW.	57
3-4	Sample model fitting for fluorescence measurements taken at 70 mW excitation power. Red corresponds to 850°C annealing and blue to 1250°C. Note that the two unprocessed diamonds are included in both data sets. The diamonds at doses exceeding 5×10^{18} e ⁻ /cm ² are also shown, distinguished from the main data set as these were not used for the fitting.	59
3-5	Fitting parameters for the fluorescence model as a function of laser power. The initial nitrogen concentration N_T is fixed at 0.15 ppm. For all plots, the error bars are extracted from the 68% confidence intervals obtained from the fitting; those associated with A are encompassed within the points.	60
3-6	NV fluorescence vs. optical excitation power of all diamonds annealed at 850°C for the (left) neutral charge state and (right) negative charge state. . .	61
3-7	NV fluorescence vs. optical excitation power of all diamonds annealed at 1250°C for the (left) neutral charge state and (right) negative charge state. .	61
3-8	Saturation model fitting for (left) Bohr (5×10^{17} e ⁻ /cm ² , 1250°C anneal) and (right) Lorentz (5×10^{18} e ⁻ /cm ² , 1250°C anneal). The NV ⁻ curve for Bohr is scaled for comparison with NV ⁰	62
3-9	Charge state fluorescence ratio NV ⁻ /NV ⁰ vs. irradiation dose over four orders of magnitude for diamonds that underwent (left) 850°C annealing treatment (right) 1250°C annealing treatment.	63
3-10	Charge state fluorescence ratio NV ⁻ /NV ⁰ vs. irradiation dose for all diamonds at (left) 100 μ W of laser excitation before the objective and (right) 10 mW. .	63
3-11	Charge state fluorescence ratio NV ⁻ /NV ⁰ vs. optical excitation power as measured before the dichroic mirror in the setup. (top) 850°C annealing treatment (bottom) 1250°C annealing treatment.	65

3-12	Photoluminescence spectra of the diamond Cannon ($5 \times 10^{19} \text{ e}^-/\text{cm}^2$, 850°C anneal) at all laser powers. Contrary to diamonds irradiated at a lower dose, the NV^- contribution to the PL spectra increases as a function of laser power.	66
4-1	(top) Ramsey pulse sequence used to measure spin-dephasing time T_2^* . (bottom) Example Ramsey curve from the diamond Rutherford ($1 \times 10^{16} \text{ e}^-/\text{cm}^2$, 1250°C anneal), where the calculated spin-dephasing time is $T_2^* = 719 \pm 41.6 \text{ ns}$.	72
4-2	Spin-dephasing times T_2^* as a function of dose measured with the Ramsey pulse sequence. Due to environmental factors that were not explicitly controlled, these values are to be seen as a lower bound of the intrinsic T_2^* of the diamond, not limited by external environmental factors. the dotted line indicate the expected ^{13}C -limited $T_2^* = 1 \text{ } \mu\text{s}$ [1].	74
4-3	(top) Pulse sequence used to measure the spin-decoherence time T_2 . (bottom) Example signal from the diamond Noddack ($5 \times 10^{16} \text{ e}^-/\text{cm}^2$, 1250°C anneal), where the calculated spin-decoherence time is $T_2 = 450 \pm 2.59 \text{ } \mu\text{s}$. The collapses and revivals in the signal are due to the Larmor precession of ^{13}C nuclei in the surrounding environment.	75
4-4	Spin-decoherence times T_2 for all diamonds as a function of irradiation dose.	77
4-5	(top) Pulse sequence used to measure the spin-relaxation time T_1 . (bottom) Example signal from a spin-relaxation pulse sequence, where the calculated spin-relaxation time is $T_1 = 5.4 \pm 0.0751 \text{ ms}$.	78
4-6	Spin-lattice relaxation times T_1 as a function of dose. All diamonds that had T_1 measurements under high laser excitation and experienced partial repolarization during relaxation are omitted.	79
5-1	Sensitivity figure of merit FOM as a function of long-pass filter wavelength λ_0 for Rutherford ($1 \times 10^{16} \text{ e}^-/\text{cm}^2$, 1250°C anneal) at 70 mW of excitation.	84
5-2	Optimum long-pass filter wavelength λ_0 as a function of laser power and irradiation dose for diamonds annealed at (top) 850°C and (bottom) 1250°C .	85

5-3	Relative sensitivity vs. irradiation dose over four orders of magnitude of excitation power for diamonds that underwent (a) 850°C annealing treatment (b) 1250°C annealing treatment.	86
5-4	Relative sensitivity vs. irradiation dose at all anneal temperatures for (left) 100 μ W and (right) 150 mW of laser excitation.	87
5-5	Example EPR spectrum for Ladd-Franklin (5×10^{18} e ⁻ /cm ² , 850°C anneal). While the signal ideally should have a flat baseline, the MW power causes a response from holding tube that needs to be subtracted.	88
A-1	Diamond characterization experimental setup (top) photograph and (bottom) schematic.	92
A-2	Diamond mount. (left) Vertical view of the objective-diamond assembly. Laser light reflects up to the objective in a cage mount where it focuses onto the diamond mount translation stage, which is adjustable to ensure that the confocal volume is at the top of the diamond near the MW loop for coherence measurements or near the bottom of the diamond for PL spectroscopy measurements. (right) Left: photograph of the diamond mount. The loop antenna is pressed against the face of the diamond and centered about the confocal spot to maximize MW uniformity. Right: diamond mount schematic with top and side views.	94
A-3	Profile of the laser beam right before being reflected off the dichroic. The D4 σ X and D4 σ Y give measures of the beam widths in the X and Y directions.	95
B-1	Experimental apparatus for PL spectroscopy (a) Spectrometer. A fiber is mounted to the entrance slit where the acquired NV fluorescence is diffracted and processed by the CCD camera. The position of the fiber can be adjusted in two dimensions. A micrometer allows fine adjustment of the spectrometer input slit. (b) Fiber shaker to eliminate modal noise in the acquired PL spectra.	98

B-2	Spectrum modification to correct for experimental artifacts. (top) Normalized photoluminescence spectra of the diamond Hilbert (5×10^{15} e ⁻ /cm ² , 1250°C anneal) at 1 mW optical excitation with and without the intensity calibration turned on. (bottom) Photoluminescence spectra of the diamond Anderson (1.6×10^{19} e ⁻ /cm ² , 1250°C anneal) at 300 μ W optical excitation with the fiber shaker turned off and on. Notice how the NV ⁻ zero-phonon line is resolvable with the fiber shaker on.	99
B-3	(Left) PL spectra for Bascom (5×10^{17} e ⁻ /cm ² , 850°C anneal) at 200 mW (top) and Heaviside (unprocessed) at 100 μ W (bottom). Bascom serves as the NV ⁰ basis function due to its high fluorescence and negligible NV ⁻ content. (Right) Construction of the NV ⁻ basis function. The NV ⁰ basis function is scaled to fit the NV ⁰ ZPL of Heaviside's PL spectrum, which is then subtracted to yield the NV ⁻ basis function. The original and basis-fitted Heaviside spectra are also shown.	101
B-4	PL spectra for Bascom (5×10^{17} e ⁻ /cm ² , 850°C anneal) at 200 mW for 405 nm and 532 nm excitation.	102
C-1	Wiring diagram for coherent control of the NV center. PB0 controls collection of photons; PB2 controls the MW field delivered to the diamond; and PB3 switches the laser to excite and polarize the NV center.	106
C-2	Diagram of the dipole magnet and (100) diamond geometry. (Left) Top view of the magnet and diamond. The diamond is mounted in the setup such that the corner is bisected by the dipole axis. (Right) Side view of the diamond and magnet. The ideal alignment for this setup and diamond orientation is to have the field axis aligned along the NV class shown.	108

C-3	Continuous-Wave Optically Detected Magnetic Resonance. (top) Pulse sequence to obtain CAW-ODMR data. (bottom) Measured CAW-ODMR spectrum of the diamond Noddack ($5 \times 10^{16} \text{ e}^-/\text{cm}^2$, 1250°C anneal). The signal m_1/m_0 shows the deviation from maximum fluorescence when the MW drives an NV orientation at or near resonance. This data was taken when the static field was aligned to one NV class (outermost resonance pair) and triply degenerate with the other three classes (innermost pair). The applied MW power is set low to observe the hyperfine splitting of each resonance due to interaction with the ^{14}N nucleus.	110
C-4	The effect of laser polarization on NV class excitation. At one angle (130° with the axes set by the third HWP in the setup), the green-colored pair is maximally excited as the electric field is perpendicular to the NV axis. Rotating the HWP 45° in either direction maximally excites the other NV pair. Selectively exciting one pair over another aids in magnetic field alignment.	111
C-5	CAW-ODMR spectrum of all four $ 0\rangle \leftrightarrow -1\rangle$ transitions for the diamond Hilbert ($5 \times 10^{15} \text{ e}^-/\text{cm}^2$, 1250°C anneal) for different half-wave plate angles. The magnetic field is mis-aligned here such that all four resonances are distinguishable. Inset: maximum deviation from the reference fluorescence of the left-most NV class as a function of the half-wave plate angle.	112
C-6	CAW-ODMR spectra of the (left) $ 0\rangle \leftrightarrow -1\rangle$ and (right) $ 0\rangle \leftrightarrow 1\rangle$ electronic transitions for the diamond Ramon y Cajal ($1.6 \times 10^{18} \text{ e}^-/\text{cm}^2$, 850°C anneal) The three Lorentzian peaks arise from the hyperfine interaction with the ^{14}N nucleus, which can only be resolved when the NV ensemble is not power-broadened from the MW and optical drive. The slight polarization of the peaks closest to the zero-field splitting of 2.87 GHz arises from partial polarization of the nuclear spin.	113

- C-7 Rabi nutation experiment. (top) Pulse sequence used to measure population oscillations under a resonantly applied MW field. (bottom) Fluorescence contrast m_1/m_0 as a function of MW pulse duration for the diamond Bohr ($5 \times 10^{17} \text{ e}^-/\text{cm}^2$, 1250°C anneal). The coherent population oscillations yield a sinusoidal fluorescence signal with a stretched exponential decay envelope. 116
- C-8 Optical pumping pulse length determination (top) Pulse sequence used to measure the re-pump time necessary to optically polarize the NV into the $|0\rangle$ state. (bottom) Example signal from a pump measurement for the diamond Lorentz ($5 \times 10^{18} \text{ e}^-/\text{cm}^2$, 1250°C anneal). After optical pumping, a π pulse flips the spin population and a repump laser pulse is applied. After a time τ , the fixed-length gate pulse is turned on to measure the fluorescence m_1 . The sequence is repeated without the π pulse to give the signal m_0 . After sweeping the start time τ , the time after which both signals achieve their steady state values is chosen as the minimum duration of the repump pulse 117

List of Tables

2.1	Diamonds processing conditions of irradiation dose and annealing temperature. For sanity, bookkeeping, and a little amusement, diamonds were named after scientists.	49
-----	--	----

Chapter 1

Magnetometry and the Nitrogen-Vacancy Center

1.1 Introduction

The measurement of increasingly precise magnetic fields has served to give civilizations the strategic edge with regards to military warfare, navigation/exploration, and scientific investigation. The earliest recorded use of a magnetometer was by the Chinese emperor Hoang-Ti (~ 2700 B.C.E.), when he navigated his army through fog-shrouded lowlands using a magnetic rock, called loadstone, to capture enemy forces [2]. This same loadstone served as the magnetization source to “feed” iron needles in compasses as 16th century explorers mapped the new world in the Age of Exploration. In the 19th and 20th centuries, advances in classical and quantum physics ushered in new generations of highly-sensitive magnetometers that continue to push the limits of human exploration. Modern applications today include mapping the magnetic field of the brain [3] and assisting archaeologists in magnetically mapping temples of ancient civilizations [4]. The push for higher sensitivity in magnetic field detection and imaging promises to unearth new applications in the life and material sciences in addition to increasing our understanding of mesoscopic physics.

Certain limits exist for today’s magnetometers, however. While atomic magnetometers currently possess the highest sensitivity in magnetometry [5], these systems typically measure only the magnitude of the magnetic field; i.e. they are scalar magnetometers. To measure

both field magnitude and direction, vector magnetometers (such as SQUIDS and fluxgates) rely on mechanical axes of the system, which can be limited by mechanical and electrical drifts. Recently, the nitrogen-vacancy (NV) center in diamond has emerged as a favorable candidate for high-sensitivity scalar and vector quantum metrology [6, 7]. In the last five years, ensembles of NV centers have mapped the μT -fields in μm -size meteorite grains [8] and noninvasively mapped the action potentials of single neurons [9]. In addition, NV ensembles in diamond are inherent vector magnetometers with the advantage of measurement axes tied to the unchanging crystal axes of diamond.

An active area of investigation is the improvement of the NV spin-state dependent fluorescence-based measurement of magnetic fields. This thesis presents a systematic study of the effects of diamond processing to understand the effects of irradiation and annealing on NV formation and the spin properties in commercially available bulk chemical vapor deposition (CVD) diamond for ensemble magnetometry. Nitrogen-vacancy-center charge state and spin decoherence times are measured for diamonds irradiated with 1 ME electrons at doses of $1 \times 10^{15} - 5 \times 10^{19} \text{ e}^-/\text{cm}^2$ and subsequently thermally annealed at temperatures of 850°C and 1250°C . The study provides an optimal range for diamond processing and shows the quenching of the NV center at high dosage from the creation of additional vacancy-related defects.

1.2 Nitrogen-Vacancy Center Physics

Among the hundreds of color centers in diamond [10] is the nitrogen-vacancy center, which is composed of a substitutional nitrogen atom adjacent to a vacancy in the diamond lattice. Figure 1-1 shows this defect along the $[111]$ crystallographic axis in diamond, where it exhibits trigonal symmetry about this axis. The NV center is primarily found in one of two charge states: the negatively charged NV^- state and the neutrally charged NV^0 state. The NV^- charge state is the focus of this thesis due to its favorable spin and optical properties for high-sensitivity magnetometry. The NV^0 charge state exhibits markedly different properties than the NV^- center and is not suited for magnetometry; as will be explained below, it can actually hinder the operation of an NV magnetometer. In this thesis, unless explicitly

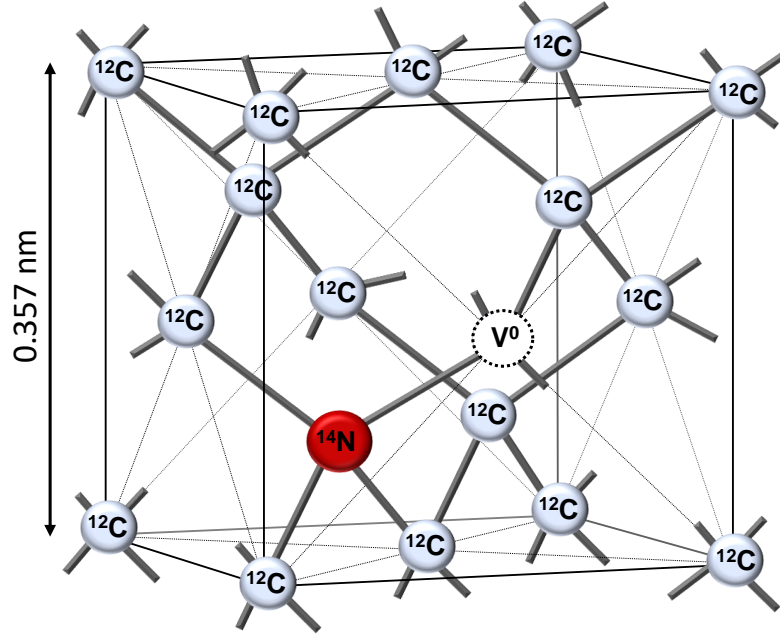


Figure 1-1: The nitrogen-vacancy center in diamond.

stated, the term NV center will refer to the negative charge state NV^- .

The first observation of the NV color center came in 1965 when du Preez [11] observed the absorption spectrum of a high-nitrogen content diamond subject to 0.78 ME electron irradiation and thermal annealing at temperatures exceeding 600°C . As will be discussed later in this thesis, irradiation from highly energetic particles creates vacancies in the diamond lattice, while thermal annealing causes the vacancies to diffuse throughout the diamond. The vacancies are trapped by the nitrogen to form the NV center. Systematically increasing the annealing temperature and measuring the absorption spectra after each anneal, after 600°C du Preez noticed the optical bands in the absorption spectra corresponding to the negative vacancy (ND1) and neutral vacancy (GR1) decreased as a new band, the “6400 Å” (640 nm) optical line increased. This of course is the well-known 637 nm optical transition of the NV^- center. These considerations led du Preez to speculate the band belonged to a substitutional nitrogen-vacancy pair in the diamond lattice.

In the 1970s the physical and electronic structure of the “640 nm” band was unraveled. Photoluminescence measurements taken by Clark and Norris [12], in addition to the uniaxial stress measurements of Davies and Hamer [13], established the trigonal symmetry of the

defect and elucidated its electronic structure. Electron paramagnetic resonance (EPR) measurements by Loubser and van Wyk led to the assignment of the negative charge state and a molecular orbital model to model the electronic structure. In this model, the dangling bonds of the carbon and nitrogen atoms surrounding the vacancy provide five of the six electrons attributed to NV^- , while the sixth is assumed to come from a nearby charge donor. The current explosion in the interest of the NV center, however, can be traced back to 1997, when Gruber et. al. used the evolving techniques of confocal microscopy to optically address and observe single NV centers in diamond [14]. It was quickly discovered afterward that the NV center possessed long coherence times and that its spin state could be readout with conventional optically-detected magnetic resonance techniques. Among the many applications the NV is suited for, these properties endow the NV center as a highly-sensitive magnetometer.

This section will briefly overview the energy level structure of the NV center, to include the neutrally-charged NV^0 . The spin polarization and spin-state dependent fluorescence emission, two crucial ingredients for practical use of the NV center, will then be explained. A more in-depth description of the NV centers can be found in [15].

1.2.1 Electronic Structure

Figure 1-2 shows a simplified diagram of the NV center’s electronic structure. We will only examine the room temperature energy structure in this thesis. A full group theoretical treatment of the NV center [16] reveals that a set of molecular orbitals form the basis of the NV energy structure. These are deep on the diamond band-gap and are filled with the six electrons of the NV center. Instead of thinking in terms of six electrons, however, it is simpler to think of the energy structure in terms of two missing electrons (“holes”) that are needed to fill the molecular orbitals. These two holes give rise to a spin-triplet ground state and excited state. Here we take the spin projection axis to be the NV axis. The electronic ground state is a 3A_2 spin triplet¹ [10] with a zero field splitting of $D_{gs} = 2.87$ GHz between the $|0\rangle$ ($m_s = 0$) and $|\pm 1\rangle$ ($m_s = \pm 1$) spin sublevels [13]. This splitting is caused by the

¹The labels A_1 , A_2 , and E describe the three irreducible representations of the C_{3v} symmetry point group of the NV center. Each of these has a certain symmetry and constrain the types of dipole-allowed transitions that can take place.

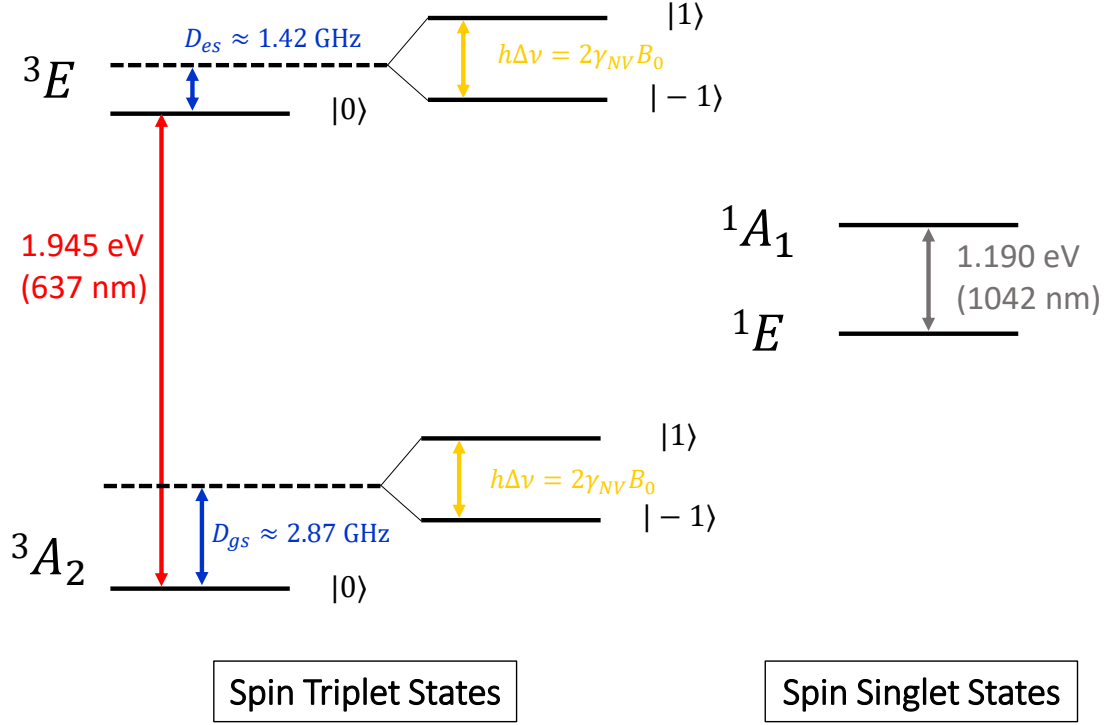


Figure 1-2: Electronic energy level structure of the NV^- center in diamond.

spin-spin interaction of the electrons. The excited state 3E is also a spin triplet state with a zero field splitting of $D_{es} = 1.42$ GHz [17]. The $|0\rangle$ states of the ground and excited spin triplet states are separated by a 1.945 eV (637 nm) zero-phonon line (ZPL). Application of an external magnetic field B causes a Zeeman shift between the $|\pm 1\rangle$ levels, leading to an energy splitting of $2\gamma_{\text{NV}}B_{\parallel}$. Here γ_{NV} is the NV gyromagnetic ratio (2.8 MHz/G [15]) and B_{\parallel} is the component of the magnetic field along the NV axis. The nitrogen nuclear spin causes an additional hyperfine splitting of each electronic spin level into two (for ${}^{15}\text{N}$, $I = 1/2$) or three (${}^{14}\text{N}$, $I = 1$) substates. Finally, in addition to the spin triplets are two intermediate singlet states 1A_1 and 1E separated by a 1.190 eV (1042 nm) ZPL [18].

1.2.2 Photoluminescence Spectra

Both the NV^0 and NV^- have resonant transitions at their respective zero-phonon lines. However, the optimal excitation wavelength of the NV^- center (to minimize population in

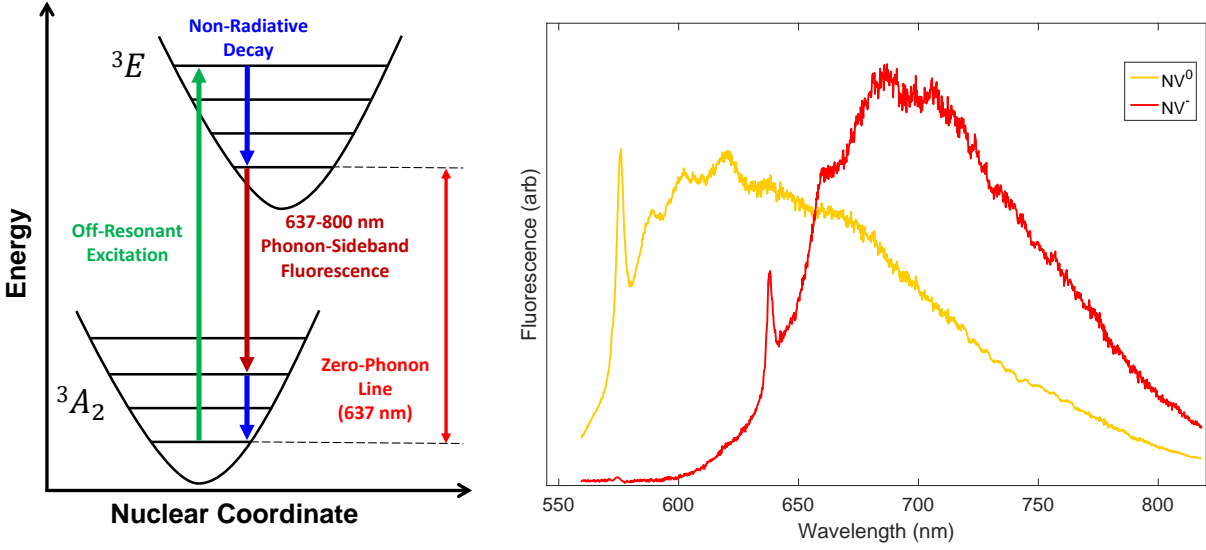


Figure 1-3: Photoluminescence of the NV center. (left) Diagram depicting the optical and vibrational transitions that occur under optical excitation. Non-radiative decay by vibrational states coupled to the main ${}^3A_2 \leftrightarrow {}^3E$ NV^- transition result in a broad emission pattern from 637 - 800 nm at room temperature. (right) Photoluminescence spectra of the NV^0 and NV^- charge states, normalized to have the same area.

NV^0 under optical illumination) is 510 - 540 nm [19]. The use of off-resonant higher energy light excites the NV into the continuum of vibrational states induced by the vibrational degrees of freedom of the electrons and nuclei. Figure 1-3 (left) shows the effect of this vibronic coupling. The vibrational states can approximately be regarded as states in a harmonic well, where the lowest state corresponds to zero phonons, the first state having coupling to one phonon, etc. Off-resonant light excites the NV into a higher-energy phonon state. Phonon relaxation quickly brings the NV spin back to one of the electronic states, where it can then spontaneously decay to the electronic ground state through a zero-phonon transition (575 nm for NV^0 , 637 nm for NV^-) or to a higher-energy phonon state, resulting in a range of longer wavelengths called the phonon-sideband (PSB). The PSB is the primary decay channel for the NV center; for the NV^- center the emission into the ZPL is only a few percent [20].

Figure 1-3 (right) depicts the photoluminescence (PL) spectrum of NV^0 and NV^- , which is the intensity of light emitted as a function of wavelength. The narrow peaks at 575 nm and 637 nm correspond to the zero-phonon lines, whereas the broad emission band at higher

wavelengths corresponds to the PSB. Note the overlap of the NV^0 PL spectrum with that of NV^- . We will see that this adds background fluorescence to NV^- state readout, which is a problem in magnetometry measurements.

1.2.3 The Neutrally-Charged NV Center

As mentioned above, the other common charge state of the NV center is the neutrally-charged NV^0 center. Initially observed in cathodoluminescence spectra in 1960 [21], this center was detected through optical absorption and emission measurements in 1979 by Davies [22]. Conclusive assignment of the observed 2.156 eV optical band to NV^0 occurred in 1996 after Mita [23] noticed the correlated changes in NV^- and NV^0 fluorescence under increased neutron irradiation. At first it was proposed that changes in the Fermi level from diamond impurities were responsible for the charge state of the NV center, but Collins [24] argued that this would not permit the co-existence of both charge states. Instead, the microscopic distribution of proximal charge donors plays the dominant role in influencing the NV's charge state.

Since it has one less electron than NV^- , the electronic energy-level structure of NV^0 differs from that of NV^- . Figure 1-4 shows the currently accepted energy level structure. Note that the NV^0 energy-level structure of NV^0 is less studied than NV^- . The proposed NV^0 states are a spin doublet ground and optically excited state, in addition to a spin-quartet metastable state [25]. Since the NV^0 does not exhibit the same spin-dependent fluorescence as NV^- under MW excitation, the overlapping PL of NV^0 adds background fluorescence that degrades the signal-to-noise of NV^- fluorescence measurements.

It is thus desirable for magnetometry purposes to eliminate the influence of NV^0 or to use it for readout. In general, elimination of NV^0 fluorescence is difficult as several phenomena contribute to charge conversion processes in addition to the native NV^0 population in the lattice. With regards to the diamond composition, if the vacancy concentration is comparable to the nitrogen concentration in the diamond lattice, NV^0 will preferentially form over NV^- . As explained above, this is due to influence the local environment of a nitrogen-vacancy has in determining the charge state. In particular, if the single substitutional nitrogen atoms are increasingly paired to vacancies, the amount available to donate an electron to an existing

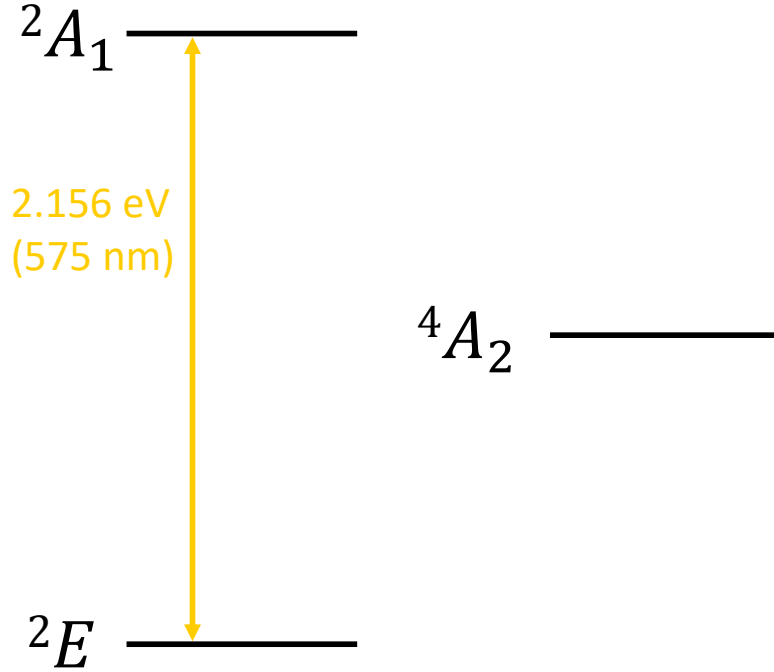


Figure 1-4: Currently proposed NV^0 energy level structure. The 575 nm ZPL transition is between a proposed spin doublet ground state and an optically excited spin doublet excited state. Experimental evidence also suggests the existence of a metastable spin quartet state.

NV^0 center to create NV^- decreases.

Even if an NV^- center exists in diamond after growth and processing, under optical illumination the NV^- center can be ionized to form the NV^0 center. Figure 1-5 shows the two-photon ionization and recombination charge state dynamics [19] between the NV^- and NV^0 . Starting in the NV^- center, under optical excitation (1) an electron in the NV^- is promoted to its excited state by one photon. (2) From there, electron is then excited to the conduction band of the host diamond by a second photon, and the resulting NV^0 center is left in either its excited state (which rapidly decays) or ground state. In the recombination process, (3) a single photon first excites an electron from the NV^0 ground state, and (4) a second photon captures an electron from the valence band, leaving the NV center in the ground state of NV^- . Under common operating conditions with a low intensity green laser, the steady-state occupation probability for the NV to be in the negative charge state is $\sim 70\%$ [26]. Note that at high enough photon energies NV^- can be directly ionized to NV^0 with a single photon, which increases the probability to be in NV^0 . At still higher energies

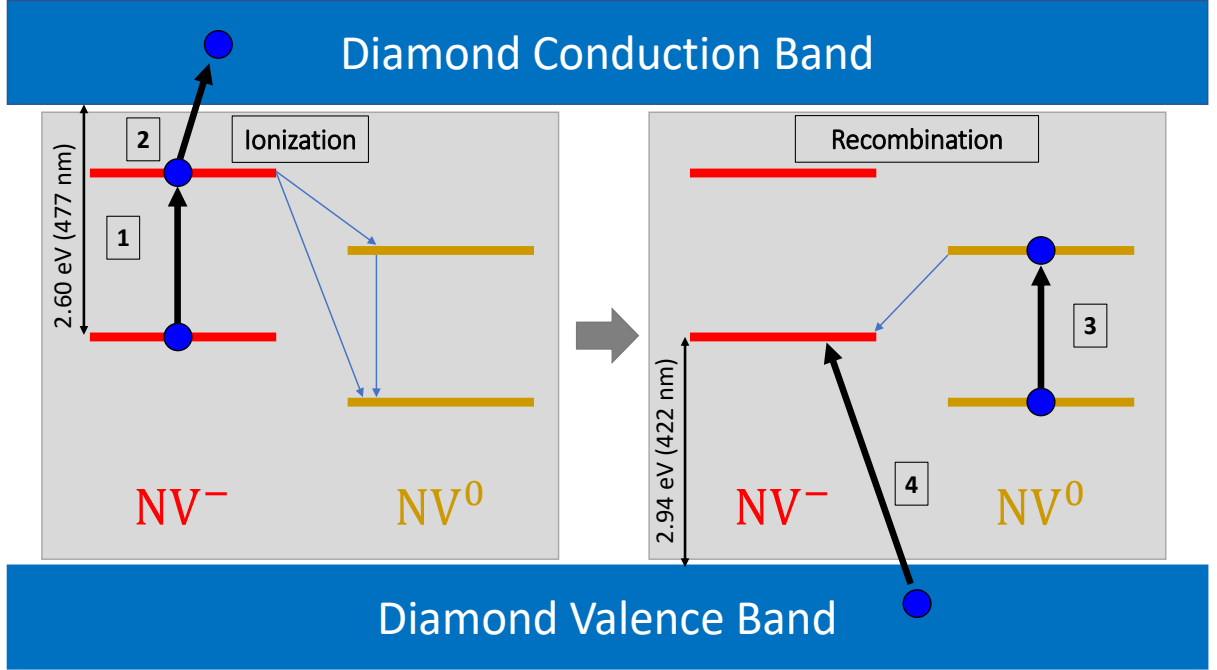


Figure 1-5: Two-photon charge state conversion between the negative and neutrally charged NV center. At wavelengths below 477 nm ionization from NV^- to NV^0 is predominantly a one-photon process, as with recombination from NV^0 to NV^- below 422 nm.

the recombination process can be accomplished with a single photon, thus increasing the NV^- occupation probability [27].

1.2.4 Spin-State Dependent Fluorescence and ODMR

We conclude this section by discussing two physical mechanisms that most applications of the NV^- center are critically dependent on. When the NV^- center is optically excited, there are two primary ways for the excited state to decay, depending on the initial electronic ground state. While the main decay path is to spontaneously decay through the zero-phonon transition at 637 nm or into the phonon-sideband between 640 - 800 nm, there exists a non-radiative decay pathway via the intersystem crossing (ISC) to the 1A_1 singlet state. The weak coupling between the 3E and 1A_1 states arises from spin-orbit coupling; this also weakly couples the 1E and 3A_2 manifolds. If the NV^- spin decays through the ISC, it quickly decays to 1E by emission of an infrared photon, which then decays to the ground state 3A_2 .

Two properties are of interest here: first, the optical cycling between the ground and

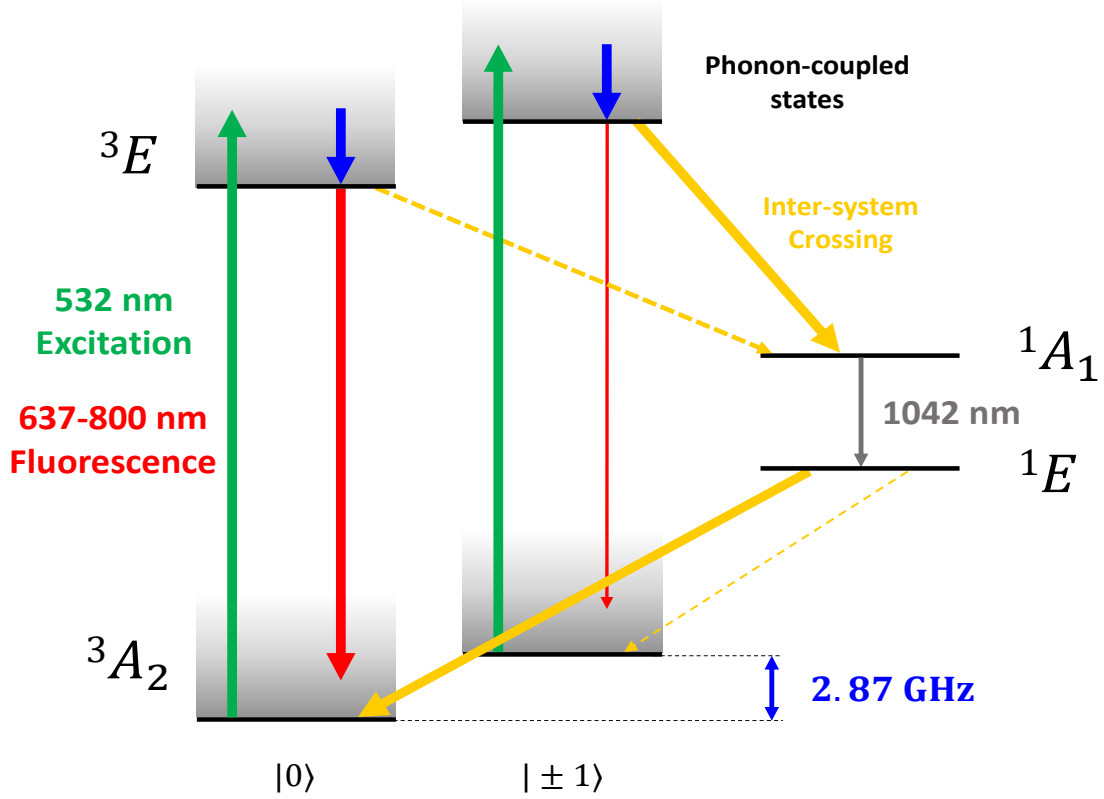


Figure 1-6: Spin-state dependent dynamics of the NV⁻ center. The $|\pm 1\rangle$ excited states exhibit a higher branching ratio to decay via the non-radiative ISC transition. After decay to the 1E state, the $|0\rangle$ ground state is preferentially populated, leading to spin polarization. The spin-dependent ISC and optical polarization lead to spin-state dependent fluorescence, where the emitted light intensity under optical excitation maps out the NV⁻ spin state.

excited states is largely spin conserving, while the ISC is mostly spin-dependent. The ISC decay occurs more frequently from the $|\pm 1\rangle$ excited state sublevels. The NV system cannot optically cycle while in the 1E singlet state (with an average lifetime of about 250 ns [28]), hence it is dark during this time period. Since the $|0\rangle$ state decays mainly through optical cycling (average excited state lifetime of 12 ns [29]), it is deemed a “bright state” and has a higher average fluorescence. The second property of interest stems from the preferentially decay from 1E to the 3A_2 $|0\rangle$ sublevel. Upon continuous optical excitation, the state is polarized into the non-Boltzmann steady state spin alignment along the $|0\rangle$ axis [15]. Both of these mechanisms (ground state spin polarization and spin-state-dependent fluorescence) are used to optically detect the NV ground spin state: if the NV center is optically excited,

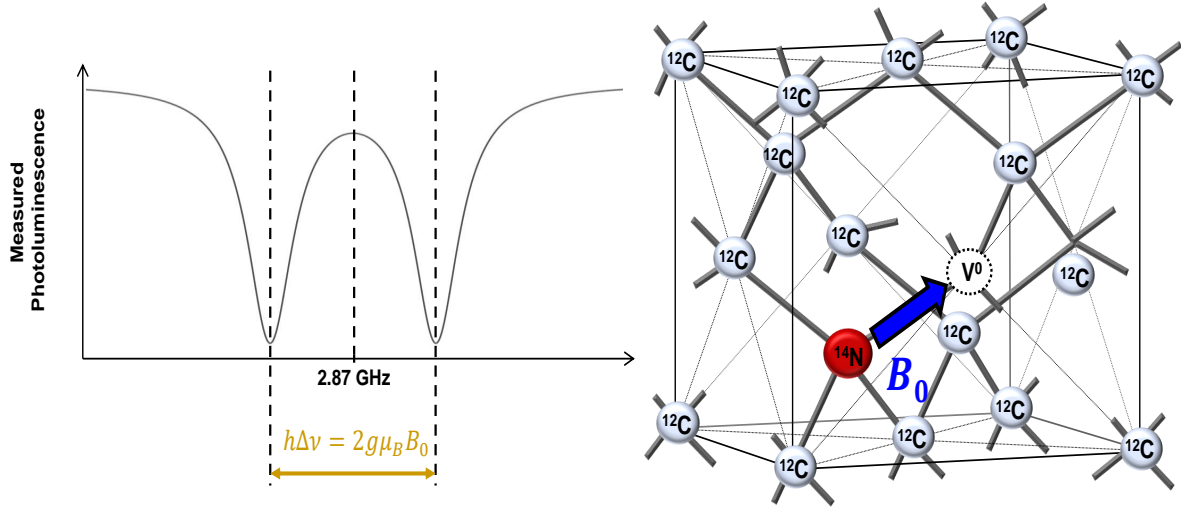


Figure 1-7: Basic detection of an applied magnetic field through a Zeeman splitting of ODMR spectra. (a) The NV fluorescence is monitored as MW excitation is swept; when the MW is on resonance with a transition between the different spin projections of the 3A_2 state, the fluorescence decreases. (b) An applied magnetic field splits the degeneracy between the $|\pm 1\rangle$ states, giving rise to two ODMR dips. The distance between the dips is proportional to the projection of the field along the NV axis.

higher fluorescence recorded indicates the spin state was initially zero. Under the same measurement time, lower fluorescence means the state was in $|\pm 1\rangle$. Figure 1-6 shows the different transitions involved in this spin-state dependent fluorescence.

The experimental procedure of optically detected magnetic resonance (ODMR) takes advantage of the spin-state-dependent fluorescence dependence to read out the transition frequencies between the different spin-sublevels of the NV ground state (see Appendix C for a more in-depth treatment). This can be achieved under continuous (CAW) laser excitation or by a pulsed technique [30]; here we will only discuss the CAW technique. The NV center is continuously excited (usually by green light), which causes the ground state-spin to be polarized to $|0\rangle$. This results in maximum fluorescence due to the lower branching ratio to the non-radiative ISC decay path, which is recorded. Simultaneously, the frequency of an applied MW field is swept through a range of frequencies. When the MW field is not on resonance between the $|0\rangle \leftrightarrow |\pm 1\rangle$ ground state transition, the fluorescence intensity is a maximum as the NV is polarized in the $|0\rangle$ state. If the MW is on an NV resonance, it drives the NV population which cycles between the $|0\rangle$ and $|\pm 1\rangle$ states. This causes a reduction in the fluorescence intensity due to the increased probability of these states to decay using the

non-radiative ISC. Thus, the recorded fluorescence signal exhibits dips at the NV resonance frequencies.

In the absence of a static magnetic field, the only transition detected in ODMR is the degenerate $|0\rangle \leftrightarrow |\pm 1\rangle$ electronic resonance at the $D = 2.87$ GHz zero-field splitting. If a static field is applied with a projection B_{\parallel} along the NV axis, then to zeroth order the $|\pm 1\rangle$ states are split by $2\gamma_{NV}B_{\parallel}$, where γ_{NV} is the NV gyromagnetic ratio (2.8 MHz/G). ODMR then records resonances at $E = D \pm \gamma_{NV}B_{\parallel}$. Figure 1-7 shows a simulated fluorescence signal from an ODMR measurement.

1.3 NV Magnetometry

The ODMR technique described above is the essence of the NV system as a magnetometer, namely the detection of Zeeman shifts through spin-state dependent fluorescence. A change in the magnetic field leads to a change in the ODMR spectrum. For a single NV center the field projection along the NV axis creates a pair of Zeeman-split energy levels; with an NV ensemble as many as eight resonances can be observed due to the four different crystallographic axes in diamond. This is the basis of vector magnetometry. The four different projections can be used to over-determine the three-component vector field, where the axes are stable to those of diamond.

In the magnetometry measurement schemes the central feature is the measurement of a population difference of the NV^{-} electronic spin between $|0\rangle$ and $|\pm 1\rangle$. Two signals are read out sequentially in order to calculate this population difference. After optical pumping to the $|0\rangle$ state, a NV fluorescence signal m_1 is acquired during/after a prescribed laser/MW excitation protocol. The NV center is then re-polarized, or repumped, by the laser and a different MW excitation is executed to record a fluorescence signal m_0 . The contrast α of the measurement is defined as $(m_0 - m_1)/(m_0 + m_1)$ and is a measure of the population difference between the signals m_0 and m_1 . The number of collected photons β in a single measurement is defined as $\beta = (m_0 + m_1)t_{gate}/2$, where t_{gate} is the fluorescence collection time. Note that the measured fluorescence signals m_0 and m_1 contain fluorescence from NV^0 due to the overlapping PL spectra of NV^0 and NV^{-} . However, since the NV^0 fluorescence

does not change under the same MW excitation that changes the NV^- fluorescence, the subtraction of the two signals in α still measures the NV^- population difference, albeit with a lower value due to the contribution of the NV^0 fluorescence in the denominator of α . This compensates for any improvement in β NV^0 may give.

1.3.1 Magnetic Sensitivity

The magnetic sensitivity in units of $\text{T}/\sqrt{\text{Hz}}$ is $\eta = \delta B \sqrt{T}$ [9], where δB is the minimum detectable magnetic field above the noise floor ($\text{SNR} = 1$) and the time T is the measurement time. For NV centers, the fundamental quantum limit to sensitivity is associated with spin projection noise [31]. However, as most NV magnetometry schemes read out magnetic fields through population differences by fluorescence detection, the photon-shot noise becomes the dominating limitation to the sensitivity of an NV magnetometer. In the photon-shot noise limited regime, the magnetic field sensitivity η takes the form [32]

$$\eta \propto \frac{1}{\alpha \sqrt{\beta T}}, \quad (1.1)$$

where T is the measurement time, α is the fluorescence contrast, the β is the average number of collected photons. Fundamental constants and other pre-factors that depend on the specific magnetometry protocol are neglected here for simplicity.

For most DC magnetometry schemes the optimal sensitivity is obtained when T is chosen to be on the order of the inhomogeneous spin dephasing time T_2^* [30], while for most AC schemes it is optimized when chosen to be on the order of the spin decoherence time T_2 [7]. While longer times in principle would give a better sensitivity, when T is longer than the dephasing/decoherence time of the NV ensemble the contrast of the sensitivity is degraded. Figure 1-8 shows simulated fluorescence data that is typically measured in DC and AC magnetometry experiments and what each of the variables corresponds to.

1.3.2 Optimizing Sensitivity

Equation 1.1 highlights the three most important variables to optimize for a given NV ensemble. Physically, a larger contrast α and fluorescence β give a higher signal-to-noise in a

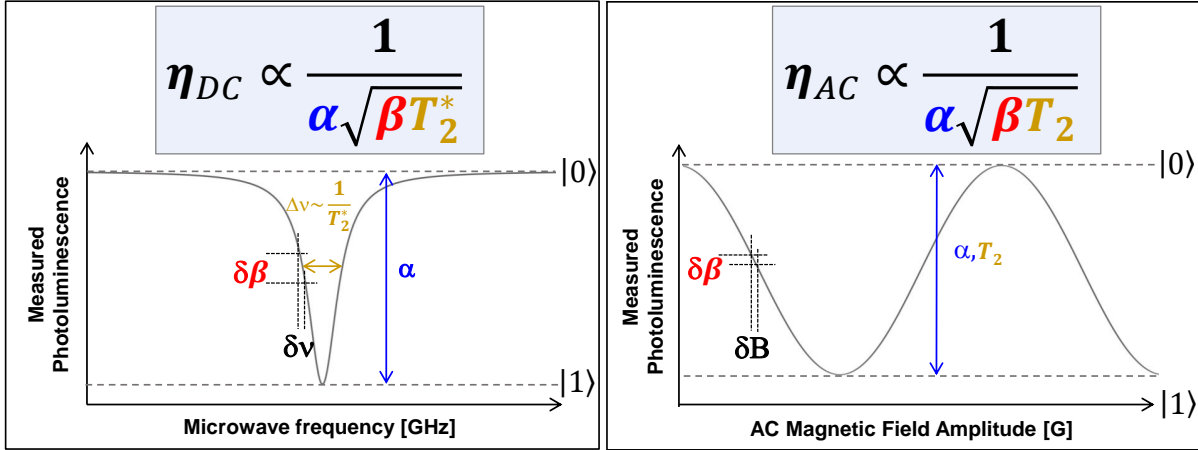


Figure 1-8: Modeled fluorescence data that is typically seen in magnetometry measurements. The contrast α in both curves corresponds to the deviation from the maximum fluorescence level that is caused by applied MW fields and the fluorescence β corresponds to the luminescence signal from the NV ensemble. For the DC (left) scenario T_2^* is a measure of the broadening of the lineshape, while in the AC (right) scenario T_2 characterizes the decay envelope.

magnetometry measurement and can be improved by increasing the NV density in a diamond. Similarly, a longer coherence time T_2 or T_2^* enables a longer signal acquisition time before the contrast is degraded by the surrounding environment, and can be improved by having a high-purity diamond free of paramagnetic defects besides the NV center. Optimizing the three parameters is not a straightforward task as they are not independent. For example, in CAW-ODMR, while one can increase the microwave drive power to the NV to increase the contrast α , the power broadening increases the linewidth of the resonance. Since the linewidth is inversely proportional to T_2^* [30], this compromises sensitivity. Similarly, in the continuous excitation scheme one can decrease the laser power broadening to narrow the linewidth at the cost of decreasing the number of photons collected. The same interdependence arises in diamond processing: while one can improve nitrogen to NV conversion by irradiation of energetic particles to increase β , creation of NV^0 and other defects from crystal damage can accompany the irradiation, thus decreasing the coherence time T_2^*/T_2 and contrast α .

We can now state the goal of this thesis: given the NV center's potential for high-sensitivity magnetometry, we wish to optimize the sensitivity in order to detect smaller fields with high precision. While different experimental protocols can be applied to achieve

this, in this thesis we focus on the host diamond itself. That is, we look to the influence of the growth and processing of the diamond lattice and the effects it has on the sensitivity of an NV ensemble. We will characterize a set of diamonds with varied processing conditions with a set of measurements to measure the contrast α , collected photons β , and the coherence times T_2 . We then look at the combined effect of these parameters in the sensitivity formula to determine the processing conditions yielding the optimal sensitivity.

This thesis is organized as follows: in Chapter 2 we will review the different diamond processing techniques and introduce the diamonds used for this study. Chapter 3 and Chapter 4 will describe the set of experiments used to characterize α, β , and T for each diamond. Finally, all the experimental results will be collectively analyzed in Chapter 5 to determine the optimal processing parameters for the specific diamonds used.

Chapter 2

Diamond Processing

2.1 Overview

The previous chapter introduced the NV center as a unique and powerful candidate for scalar/vector magnetometry and magnetic field imaging. To detect sub-picoTesla magnetic fields and to image sub-millimeter magnetic regions, the NV magnetometer must be tailored to optimize the magnetic field sensitivity η . This sensitivity optimization can be realized, for example, by employing dynamical decoupling pulse sequences to isolate the NV center from the environment [33], optimizing the geometry of the diamond to enhance fluorescence collection [34], or by post-diamond growth processing to enhance the NV concentration and purity of the surrounding environment [35]. In this thesis, we focus on the latter approach and examine the effects of diamond processing on NV magnetometry properties. Specifically, we examine the effects of varying electron irradiation doses and different anneal temperatures on a set of initially identical diamonds to find a processing regime suited to ensemble magnetometry.

Diamond processing in this context refers to modifying the diamond properties during and after the growth process to produce desired effects. Commercially, these techniques have been historically developed in the gemology industry where diamonds (among other stones) are irradiated with high energy particles to change their color [36]. For NV diamond magnetometry, the desired effect is to increase the nitrogen to NV conversion efficiency while also keeping the environment free of other defects that can decohere the NV ensemble.

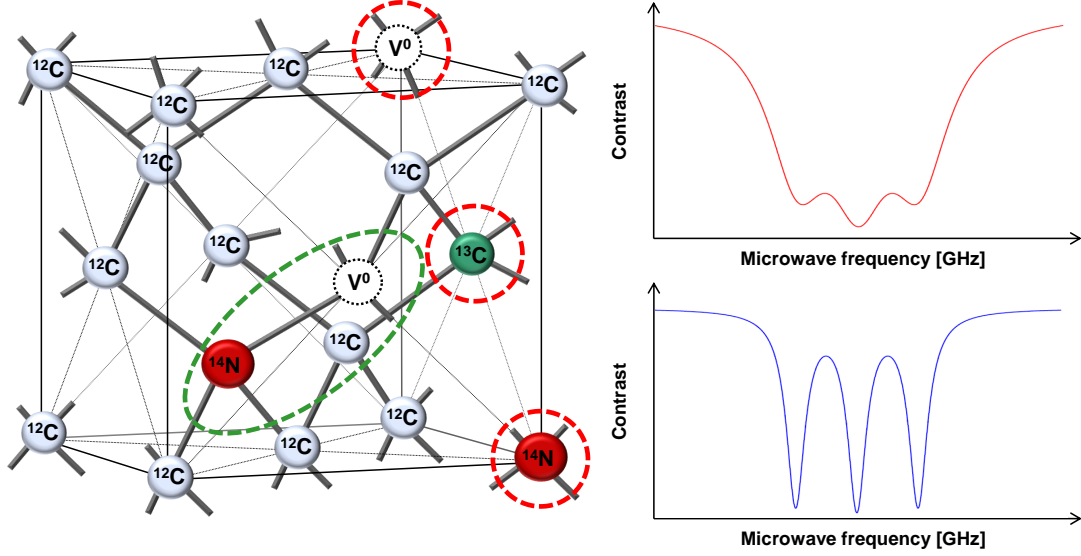


Figure 2-1: The effects of diamond processing on NV ODMR lineshapes. (Left) A diagram of the diamond lattice showing a nitrogen-vacancy center (circled in green) along with other defects (circled in red) that interact with the NV center and broaden its resonance profile, such as single vacancies, substitutional nitrogen atoms, or ¹³C atoms. (Right) Simulated ODMR curves for (top) a naturally abundant 98.9% ¹²C diamond and (bottom) a isotopically ¹²C pure diamond, where the effects of broadening from ¹³C are eliminated.

Figure 2-1 shows the simulated effects of one example of diamond processing. A diamond with defects such as isolated vacancies, isolated single substitutional nitrogen, and ¹³C interact with the NV center to broaden the measured ODMR lineshape [37]. Growing isotopically pure ¹²C diamond [38] narrows the lineshape by eliminating dipolar coupling with ¹³C, and thus increases the coherence time.

In this chapter we discuss the role of diamond processing in creating an NV ensemble in the diamond lattice. First, two main methods of synthetic diamond growth are discussed. Then, we focus on the incorporation of individual nitrogen and vacancies in the lattice, along with how to couple them to form an NV center. Finally, we introduce the diamonds used in this thesis, along with the processing methods used.

2.2 Diamond Processing

There are several factors to consider in processing a diamond for NV magnetometry: how to grow the diamond, controlling the amount of nitrogen and vacancies incorporated into the diamond lattice, and how to form the NV defect centers while minimizing the presence of other unwanted defects. Each has a significant effect on the resulting properties and concentration of NV centers in the diamond (both charge states) and the surrounding environment. This section will go over each of these factors and discuss why we chose specific diamond processing recipes for our study.

2.2.1 Synthetic Diamond Generation

While it is possible to perform NV magnetometry with natural diamonds, the reproducibility and control of defects that synthetic diamond affords makes it the preferred diamond type. Since graphite is the thermodynamically stable form of solid carbon at room temperature and pressure, synthetic diamond manufacturing methods must provide the favorable thermodynamic environment or chemical kinetic conditions that promote diamond growth. The three main manufacturing methods to create synthetic diamond are high pressure, high temperature synthesis (HPHT); chemical vapor deposition (CVD); and detonation techniques to create nanodiamonds. The choice of diamond type for NV Quantum Information Processing depends on the desired application. As nanodiamonds with NV centers fall outside the scope of this thesis, their synthesis and properties will not be discussed here.

HPHT synthesis takes the thermodynamic approach and provides the temperatures and pressures necessary for stable diamond formation. This method, which mimics the conditions by which natural diamonds are formed in the Earth’s mantle, was first demonstrated by Bundy et al. in 1955 at General Electric [39]. Seed crystals (for single crystal diamond growth, the seed is usually a seed diamond) are placed alongside a high-purity graphitic carbon source and metal catalyst in an anvil press, at pressure around 5 GPa with temperatures exceeding 1400°C. The metal catalyst (usually a solvent of transition metals like nickel, cobalt, and/or iron) dissolves the graphitic carbon and transports it to the seed crystal in addition to lowering the temperature needed for diamond formation [40]. A temperature

gradient is applied to precipitate carbon onto the seed crystal, which then grows into the desired diamond.

CVD, in contrast to HPHT synthesis, creates chemically kinetic conditions that favor the growth of diamond over graphite. This allows lower temperatures and pressures to be used during growth. A substrate (again, usually a diamond for single crystal growth) is placed in a reactor along with gas containing carbon and hydrogen. After the gas is heated into a plasma the ensuing carbon radicals deposit onto the substrate, which in this metastable environment can be in the form of graphite (sp^2 -hybridized) or diamond (sp^3 -hybridized). Early methods in the 1960's used filaments to heat and dissociate the gas, but (to avoid introducing impurities into the diamond) microwaves are primarily used today [41]. The hydrogen radicals etch off carbon that hybridizes in the sp^2 form, allowing diamond to grow layer-by-layer instead to form plates a few millimeters in size [42].

A consideration in both of these methods is the isotopic content of the carbon used to form the diamond lattice. Naturally occurring carbon is composed 1.1% of the isotope ^{13}C , which has a nuclear spin $I = 1/2$. The dipolar coupling between this spin and the NV electronic spin is a source of decoherence that limits the coherence times T_2 and T_2^* of the NV center. If the isotopic content is controlled (e.g. using isotopically pure ^{12}C methane gas in CVD synthesis), the abundance of this isotope decreases and the coherence time is extended [38, 43]. At the time of this thesis, only naturally abundant diamonds (1.1% ^{13}C) were available for our study.

Although HPHT synthesis enables mass-production of diamond that can be used for numerous industrial applications, for NV magnetometry diamonds created by CVD are preferred for the following reasons. First, as discussed below, a high concentration of paramagnetic substitutional nitrogen lowers the coherence time of the NV center [44]. HPHT synthesis typically produces diamonds with 100–200 ppm of nitrogen (which, since nitrogen absorbs mostly blue and green light, gives the diamond a yellow color), while CVD produces a range usually between 1 ppb to a few or several ppm, where the effects of other impurities like ^{13}C can become the dominant source of decoherence. Second, CVD allows more precise control over the defects introduced into the diamond by means of the gases used. This allows higher-purity diamonds to be produced and altered to fit a particular technological

application.

2.2.2 Nitrogen Incorporation

In addition to the way the host diamond is grown, the nitrogen content is a crucial factor in creating NV centers in the diamond lattice. In both HPHT and CVD diamonds, nitrogen is a major impurity incorporated during growth. In addition to deliberate addition of nitrogen (usually N_2) during diamond growth, the residual air in the growth chamber, the carbon gas sources (usually methane), and the metal catalysts (nickel, iron, and cobalt are commonly used) are just a few sources that, if left unchecked, can cause the creation of unwanted nitrogen defects in the lattice. In both HPHT [45] and CVD [46, 47] diamonds single substitutional nitrogen N_S (also called the P1 center) is the main form of the nitrogen defect. If the nitrogen is not controlled, HPHT growth may give rise to hundreds of ppm, which becomes the dominant limiting factor of the coherence time of the NV center [7, 44, 48]. Controlled nitrogen incorporation can be achieved by the use of nitrogen-getters like aluminium or boron [49] and injecting a controlled amount of nitrogen gas into the growth chamber. For CVD diamond, the amount of nitrogen-containing gas can be varied to get a desired nitrogen concentration, but with great care nitrogen concentrations lower than 100 ppb can be obtained [50].

Another method to incorporate nitrogen into the lattice is through nitrogen ion implantation, usually with the ions N^+ or N_2^+ . The advantages of this method are that it allows a greater control over the nitrogen dosage and introduces the extra vacancies needed in the diamond to form NV centers (after subsequent annealing, as explained below). The position and depth can also be controlled with great precision, making this an advantageous approach for single NV experiments or experiments with NV layers. For nitrogen implantation the use of ^{15}N can allow implanted nitrogen to be distinguished from existing nitrogen in the diamond. The disadvantages, however, make this method less appealing for ensemble magnetometry: the optical and spin coherence properties of NV centers formed with these nitrogen ions is usually worse compared to as-grown NV centers. Two relevant reasons are the higher preference to be in the NV^0 charge state [51, 52] and the shorter coherence times due to radiation damage caused by the nitrogen to the diamond lattice [38, 53]. For this

reason, we used the as-grown nitrogen in our CVD diamonds to make NV centers and did not pursue ion implantation.

2.2.3 Vacancy Production

Regardless of how the nitrogen is added to the diamond, to form nitrogen-vacancy centers the corresponding vacancies need to be present in the lattice. For NV centers it is believed [24] that two nitrogen atoms are required to form a NV center: one to pair with a vacancy and another to donate an electron to make the NV center negatively charged. This sets the ideal nitrogen to NV conversion efficiency to 50%; were this to be exceeded the native NV⁰ concentration would increase as the available substitutional nitrogen N_S charge donors would decrease. Although for CVD diamonds NV centers are present after growth, the nitrogen to NV conversion efficiency is usually less than 0.5% [54]. Thus, to create more vacancies and enhance the NV concentration, the diamond is usually irradiated with high-energy particles to displace carbon atoms from their lattice sites. The caveat to this method is that additional defects may be introduced into the diamond, giving rise to additional paramagnetic defects [38, 47, 55, 56] that can lower the coherence time of the NV center.

To minimize unwanted damage to the diamond lattice while still increasing the nitrogen vacancy concentration, the type and energy of irradiating particles can be controlled. As discussed above nitrogen ions are an option to create vacancies, but other ions and heavy particles can be used such as protons and neutrons [36]. Gamma rays are also an option [57]. For NV magnetometry, however, these high energy and momentum particles are undesirable due to the large amounts of damage they create. Irradiation of this type can produce knock-on atoms [58], which occurs when the carbon atom is displaced from the lattice site with enough energy to itself displace further carbon atoms. Additionally, these heavier particles can create localized lattice damage that cannot be annealed out, as described in the following section [59], as well as paramagnetic vacancy chains [38]. Electrons on the other hand are light enough to avoid this type of damage and are more suited to creating evenly distributed monovacancies [58]. This is the preferred irradiation particle to create NV ensembles optimized for NV magnetometry.

The energy of the irradiation electrons determines the depth of penetration. Experimen-

tally vacancy creation has been observed for incident electrons with energies greater than 180 keV [60], which gives the electron enough energy to collide with the carbon atoms and transfer about 35 eV of activation energy. This value closely matches theoretical predictions of [57] where monovacancy production is calculated to occur with electron energies of at least 165 keV. To avoid excess damage to the diamond lattice, it is desirable to keep the electron energy low enough to prevent the creation of vacancy chains (but high enough to penetrate through the diamond).

2.2.4 Thermal Annealing

The final step in NV creation is the diffusion of vacancies to the nitrogen atoms embedded in the lattice, which is accomplished by high temperature annealing of the diamond. In addition to alleviating the crystal strain caused by the irradiation, vacancies begin to diffuse in the lattice at 600°C [61] and get trapped by the nitrogen atoms. Annealing at even higher temperatures causes certain defects to ‘anneal’ out, but can also cause the creation of more stable defects [38, 55].

2.3 Diamonds used in this Thesis

Section 2.2 showed that there are numerous ways to grow and to process a diamond, which results in variable properties NV centers. For our purposes we want to choose processing recipes that best tailor the diamond for NV ensemble magnetometry. For the type of diamond to use, CVD is likely preferred over HPHT due to the lower nitrogen content, higher control of defect incorporation and isotopic composition, and easier ability to control the geometry of the sample (e.g. create a layer with nitrogen defects atop a purer diamond substrate). For this study we chose commercially available CVD diamonds with an initial nitrogen concentration of 0.15 ppm [62] and a natural abundance of ^{13}C (1.1%). Although a higher concentration of nitrogen and a high purity ^{12}C diamond would be better suited to NV ensemble magnetometry, at the time of this study these were the commercially available CVD diamonds, in addition to HPHT diamonds at a few hundred ppm of nitrogen. However, the commercial availability gave us the means to acquire a large set of diamonds for a

systematic study of diamond processing, with the intent of studying the effects of irradiation and annealing and extracting results that can be applied to diamonds suited for magnetometry when they become more available. Electron irradiation at a commercial company (Prism Gem) using 1 ME electrons is used to produce vacancies in the diamonds.

The diamonds in the study are commercially available standard grade diamond available from Element Six. The size of the diamonds are thin square wafers of side-length 2.6 mm and thickness of 0.3 mm with un-polished sides and (100) polished surfaces. The nitrogen-14 concentration listed by Element Six is 0.15 ppm ($\approx 2.64 \times 10^{18} \text{ cm}^{-3}$). The natural isotopic abundance of carbon is 98.9% ^{12}C and 1.1% ^{13}C . Prism Gem in New York irradiated and annealed the diamonds. To ensure the radiation damage was uniform throughout the diamond, the 1 ME electron beam used was 1 cm in diameter. A given electron irradiation dose in electrons per cm^2 depended on the duration of the irradiation treatment. The samples were placed on water cooled plates not exceeding 66°C , and Prism Gem predicted the diamond sample temperature was under 120°C during irradiation. The samples are flipped halfway throughout the irradiation. The annealing recipes all involved first heating the diamonds to 850°C in a reduced nitrogen atmosphere of 1.0 atm. A thermocouple kept track of the temperature as the diamonds annealed for an hour. Those diamonds slated to receive a 1250°C anneal were then moved to another furnace in a 100 torr (0.13 atm) hydrogen atmosphere for an hour. The temperature in this chamber was recorded by a pyrometer pilot chip. Figure 2-2 shows the effects of annealing on diamond color for three of our samples that had the same irradiation dose.

All twenty-eight diamonds we characterized are compiled in Table 2.1. With the exception of three diamonds (two of them being control diamonds that received no post-growth processing), all were subjected to an initial anneal at 850°C for one hour. After a given dose of irradiation the diamonds were either not annealed, annealed at 850°C for one hour, or annealed 850°C for one hour followed by an anneal at 1250°C for one hour. The range of electron doses was chosen such that the range of vacancy concentration before annealing be less than, comparable to, and greater than the nitrogen concentration in the diamond.

Sample	Pre-anneal ($^{\circ}\text{C}$, 1 hr)	Irradiation (1 ME e^{-}/cm^2)	Post-anneal ($^{\circ}\text{C}$, 1 hr)
Meitner	none	none	none
Heaviside	none	none	none
Hyde	850	none	850
Ayrton	850	1×10^{15}	850
Curie	850	5×10^{15}	850
Leavitt	850	1×10^{16}	850
Robbins	850	1×10^{16}	850
Einstein	850	5×10^{16}	850
Blodgett	850	1×10^{17}	850
Wegener	850	5×10^{17}	850
Bascom	850	5×10^{17}	850
Ramon y Cajal	850	1.6×10^{18}	850
Evans	850	5×10^{18}	850
Ladd-Franklin	none	5×10^{18}	850
Thomson	850	1.6×10^{19}	850
Cannon	850	5×10^{19}	850
Diesel	850	1×10^{15}	1250
Hilbert	850	5×10^{15}	1250
Rutherford	850	1×10^{16}	1250
Blau	850	1×10^{16}	1250
Noddack	850	5×10^{16}	1250
Cori	850	1×10^{17}	1250
Bohr	850	5×10^{17}	1250
Mendeleev	850	5×10^{17}	1250
Stevens	850	1.6×10^{18}	1250
Lorentz	850	5×10^{18}	1250
Anderson	850	1.6×10^{19}	1250
Planck	850	5×10^{19}	1250

Table 2.1: Diamonds processing conditions of irradiation dose and annealing temperature. For sanity, bookkeeping, and a little amusement, diamonds were named after scientists.

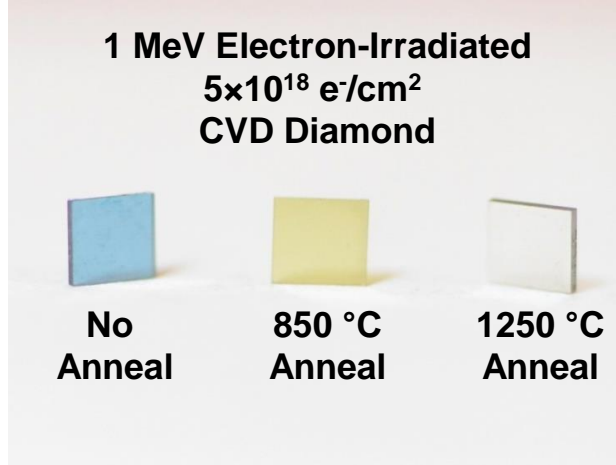


Figure 2-2: Three Element Six standard grade diamonds used in this thesis with the same electron dose subjected to varying annealing temperatures. The change in color is due to the annealing out of different defects at higher temperatures.

2.4 Conclusion

In this chapter and the previous one we have set the stage for the experiments performed in this thesis. Chapter 1 discussed the sensitivity equation, a key metric in NV magnetometry, in terms of its main variables and how each can be optimized. In this chapter we then looked at how diamond processing techniques could be used to create and tailor a NV ensemble in diamond for the purpose of high-sensitivity magnetometry.

The remainder of this thesis is dedicated to two sets of measurements designed to test each diamond for properties relevant to magnetometry. Chapter 3 will describe photoluminescence spectroscopy measurements used to examine the charge state fluorescence ratio of NV^- to NV^0 along with the total fluorescence of the NV ensemble. Chapter 4 details the coherence-time measurements that extract the spin decoherence time T_2 for each diamond. Finally, in Chapter 5 the results will be analyzed to obtain an optimal parameter space for diamond processing with commercially available CVD diamonds.

Chapter 3

Charge State Fluorescence Characterization

3.1 Overview

As outlined in the previous two chapters, the goal of this thesis is to understand the effects of irradiation and annealing on NV^- formation and the spin properties in diamond for ensemble magnetometry. To accomplish this goal we fix the type and energy of the irradiation particle (1 ME electrons) and initial nitrogen concentration (0.15 ppm) and systematically vary the irradiation dose and annealing temperature. We determine which combination optimizes the sample set for magnetometry. To quantify magnetometry performance, we look at the sensitivity equation ($\eta \sim 1/\alpha\sqrt{\beta T}$), which depends on the fluorescence contrast α , photons collected β per measurement, and interrogation time T [7, 30, 32] (which is bounded by the NV coherence time T_2). In this chapter we start the characterization of the 28 diamonds used in this study by evaluating the contrast α and the photons collected β by photoluminescence spectroscopy measurements. The other variable in the ever-present sensitivity equation, T , will be addressed in the next chapter.

After discussing the role of the contrast α and collected photons β in magnetometry measurements, this chapter will describe the acquisition of photoluminescence (PL) spectra and subsequent analysis by fitting to a linear combination of NV^0 and NV^- spectra. Two relevant quantities are extracted from the PL spectra: the total NV fluorescence (which

measures the collected photons β) and the charge state fluorescence ratio (which affects α). The behavior of these two quantities with irradiation dose and laser excitation power will be shown.

3.2 Charge State Dynamics and Magnetometry

In Chapter 1 we defined the contrast α in terms of the two signals acquired in a magnetometry measurement, from which the NV^- population difference (and thus the magnetic field) is calculated. For the two fluorescence rate signals m_0 and m_1 , the contrast is $\alpha = (m_0 - m_1)/(m_0 + m_1)$. The number of photons collected in a measurement was similarly defined in terms of m_0 and m_1 : $\beta = (m_0 + m_1)/2t_{\text{gate}}$, where t_{gate} is the fluorescence collection time. To optimize α and β for the magnetic sensitivity, a high conversion efficiency of a fixed amount of single substitutional nitrogen N_S to NV^- centers is required. As mentioned in Chapter 2, to form an NV^- center, typically two nitrogen atoms in the diamond lattice are required, one to capture the vacancy and another nitrogen (or charge donor) to donate an electron to give the NV a negative charge [63]. As the initial N_S to NV^- conversion efficiency in as-grown synthetic diamond is low [54], irradiation of high energy particles or ions is used to create more vacancies that, upon subsequent annealing, increase the NV^- concentration. This process increases the number of collected photons in the signals m_0 and m_1 and thus improves β .

An unwanted consequence of this processing procedure, however, is the increased presence of the neutrally-charged nitrogen-vacancy center NV^0 [47], which does not possess the desired optical and spin properties needed for magnetometry. If a vacancy captured by a nitrogen atom is not located close to an N_S atom, it will not receive the needed electron to become NV^- . If the concentration of created vacancies from irradiation approaches the concentration of nitrogen, NV^0 will be the dominant NV charge state in the diamond lattice as there will be fewer N_S to donate electrons [23]. Figure 3-1 shows the PL spectrum for Diesel ($1 \times 10^{15} \text{ e}^-/\text{cm}^2$, 1250°C anneal) excited with 10 mW of laser power. The PL spectrum shows the zero-phonon-lines (ZPL) of both the NV^0 (575 nm) and NV^- (637 nm) charge states, as well as their respective phonon-sidebands. The Raman line at 572 nm, which arises

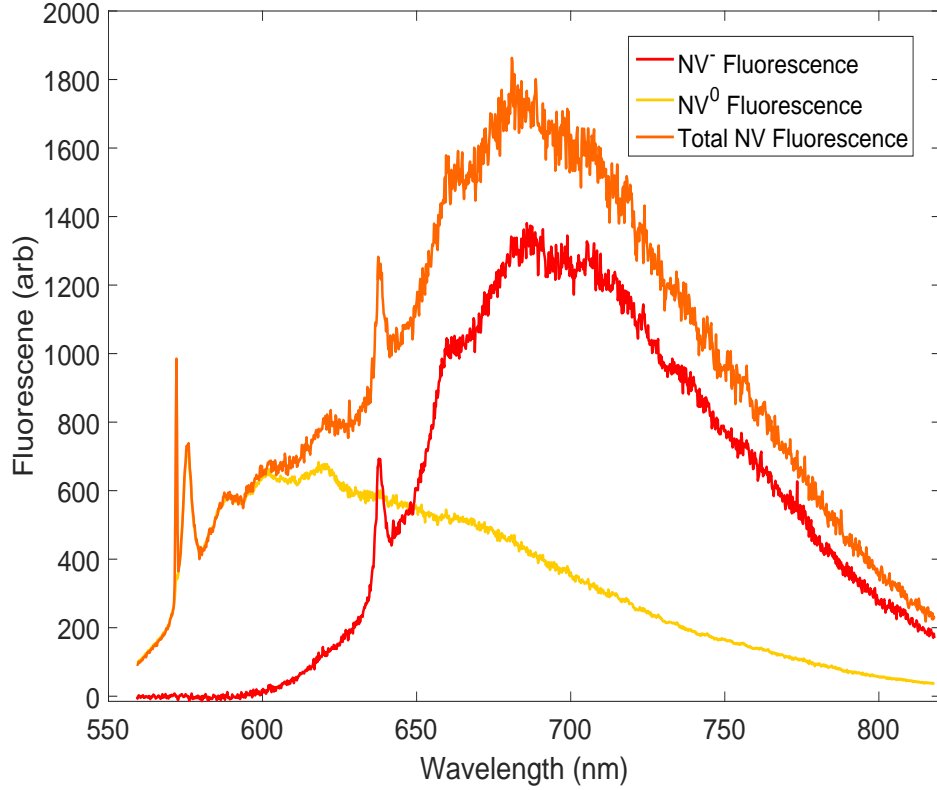


Figure 3-1: Example photoluminescence spectra for Diesel ($1 \times 10^{15} \text{ e}^-/\text{cm}^2$, 1250°C anneal) at 10 mW of laser excitation. The PL signatures from the NV^0 and NV^- charge states are also shown to highlight the contribution of each charge state, as well as the overlap of the two spectra.

from inelastic light scattering of the laser photons with the diamond lattice, is also shown. The overlap of the NV^0 PL spectrum adds background fluorescence to NV^- state readout. As NV^0 does not respond to the MW excitation that creates a population difference in NV^- , the overall photons collected β increases, but the contrast α decreases.

It is thus desirable to determine irradiation dose required for a given initial concentration of nitrogen that maximizes the N_S to NV^- conversion efficiency while minimizing the degrading effects of NV^0 , both native NV^0 and that produced in readout. Even if the conversion efficiency is high (low native NV^0 concentration) post-processing, there are other physical mechanisms that lead to the presence of NV^0 in the lattice while under optical excitation. Recall from Chapter 1 that the ionization of NV^- into NV^0 under optical excitation is a two-photon process, as is the recombination process of NV^0 to NV^- . Under the common

operating conditions of low-intensity green laser excitation, the dynamics of these competing processes give rise to the NV center on average residing in the neutrally-charged state 30% of the time [19, 26]. In addition, experiments have shown that increasing the intensity of optical excitation further photo-ionizes the NV center to spend a larger fraction of time in the neutral charge state [51, 64], since it is a two-photon process as explained in Chapter 1.

Given these considerations, we characterize the charge state fluorescence of our diamonds as a function of excitation power to provide a measure of the collected photons β and contrast α . For the collected photons we monitor the integrated fluorescence intensity of each charge state as a function of irradiation dose and optical excitation power (the photons collected β also depends on the gate time of fluorescence collection, but this will not be addressed in this thesis). We provide a simple model for explain the fluorescence behavior with irradiation to investigate the conversion of irradiation dose to NV centers. Similarly, for contrast we measure the ratio of the fluorescence of each charge state as a function of irradiation dose and optical excitation power.

3.3 Measurement Procedure

To measure the PL spectra of each diamond, off-resonant 532 nm excitation is focused with an objective to a spot size of $3.1\ \mu\text{m}$ in diameter and depth of focus (Rayleigh Range) of $z_R = 32\ \mu\text{m}$. A full description of the experimental setup is in Appendix A. The same objective collects the resulting fluorescence, which propagates to a $10\text{-}\mu\text{m}$ multimode fiber that acts as a pinhole. This fiber directs the light to a spectrometer with a CCD camera in the readout plane. All frames taken by the spectrometer/CCD for a single measurement are averaged together, followed by normalization by the exposure time of the measurement. To analyze the fluorescence from each charge state for each diamond at different laser powers, we fit each measured PL spectrum to a linear combination of NV^0 and NV^- spectra [65], as described in Appendix B. The ratio of the coefficients forms the charge state fluorescence ratio, while the integral of the coefficient-weighted basis spectra gives the fluorescence of each charge state.

Frequently in the literature the fluorescence of NV^- centers is commonly used to estimate

their concentration in a given diamond, where the integrated ZPL fluorescence from an ensemble PL spectra is normalized to the integrated ZPL of a single NV center/ensemble of known concentration [35, 53, 66]. The proper conversion of fluorescence to concentration is not as trivial as it first appears, however. First, the fluorescence must be taken in the low laser intensity regime, where the fluorescence is proportional to the concentration of the emitters. At higher excitation, charge state conversion [19, 64] and saturation effects introduce a more complex relation between the fluorescence and concentration. Second, because the NV center is dynamically switching between different charge states under optical excitation, the ensemble fluorescence measured is a time-averaged value [19]. This means the charge state fluorescence ratio is not equal to the charge state concentration ratio. A full rate-equation analysis of the different levels of NV^0 and NV^- is required for an accurate comparison; however, the full electronic structure (and associated transition rates) of NV^0 is still the subject of active investigation. For these reasons we report the charge state fluorescence only. This is also the most important parameter because in practice this ratio determines the contrast α and collected photons β in a magnetometry measurement.

We now systematically show the results of charge state fluorescence measurements, both as a function of irradiation dose and optical excitation power.

3.4 Charge State Fluorescence Measurements

3.4.1 Total Fluorescence vs. Irradiation Dose

We first characterize the collected photons β for each diamond by calculating the total NV fluorescence. The total NV fluorescence is obtained by adding the fluorescence from each charge state, determined from the linear combination of the NV basis functions. Figure 3-2 shows the total NV fluorescence vs. irradiation dose D over four orders of magnitude of laser power. For clarity the data from two annealing temperatures are plotted separately. For both annealing temperatures and all laser excitation powers, we observe three regions of different behavior: at low electron irradiation doses ($D \lesssim 1 \times 10^{18} \text{ e}^-/\text{cm}^2$), the fluorescence steadily increases; at intermediate doses ($1 \times 10^{18} \text{ e}^-/\text{cm}^2 \lesssim D \lesssim 1 \times 10^{19} \text{ e}^-/\text{cm}^2$) the

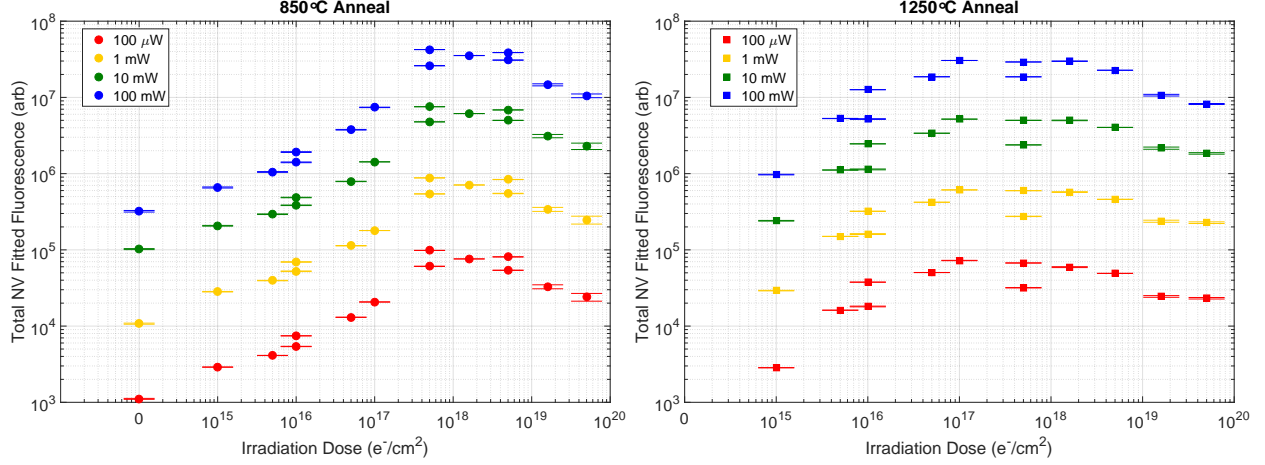


Figure 3-2: Total NV fluorescence vs. irradiation dose over four orders of magnitude for diamonds that underwent (left) 850°C annealing treatment (right) 1250°C annealing treatment.

fluorescence saturates, and at the highest doses ($D \gtrsim 1 \times 10^{19} \text{ e}^-/\text{cm}^2$), the fluorescence begins to decrease. The first two dose regions are consistent with the discussion of vacancy production in the lattice in Section 3.2. Higher irradiation doses introduce more vacancies into the lattice, which after annealing lead to the formation of more NV centers (NV^- and NV^0). As the vacancy concentration surpasses that of nitrogen in the diamond, the fluorescence saturates as the production of NV ceases. The behavior at the highest doses where the fluorescence begins to decrease is not expected from considering nitrogen and vacancy concentrations alone. One possible cause could be the creation of vacancy-related defects that quench the concentration of NV centers [55].

To compare the affects of annealing temperature, we look at both temperatures simultaneously. Figure 3-3 displays the total fluorescence of all diamonds as a function of irradiation dose for low (100 μW) and high (10 mW) laser excitation. In terms of the behavior discussed above, the fluorescence of 1250°C annealed diamonds saturate at a lower dose ($\sim 1 \times 10^{17} \text{ e}^-/\text{cm}^2$) than that of the 850°C annealed diamonds ($\sim 5 \times 10^{17} \text{ e}^-/\text{cm}^2$). This means the efficiency of NV formation for a given dose is higher for 1250°C anneal diamonds. This can be understood in terms of vacancy diffusion: in a diamond subjected to a hotter annealing temperature, the vacancies diffuse farther in that lattice for a given amount of time, giving them a higher probability to be trapped by a nitrogen atom. Note, however, that at all powers shown the highest fluorescence occurs at 850°C, the decrease of fluorescence at the

highest doses seems to be independent of the annealing temperature, however, since it occurs at about the same dose ($\sim 1 \times 10^{19} \text{ e}^-/\text{cm}^2$) for both temperatures.

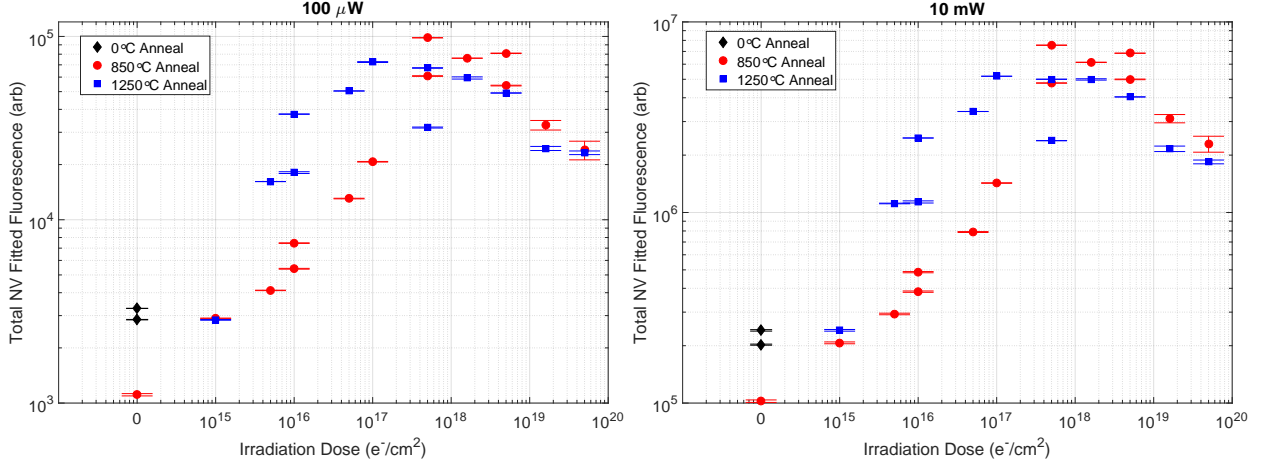
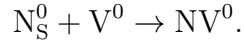


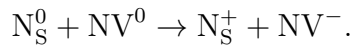
Figure 3-3: Total NV fluorescence vs. irradiation dose for all diamonds at (left) $100 \mu\text{W}$ of laser excitation before the objective and (right) 10 mW .

3.4.2 Fluorescence Model

To further investigate the effect of annealing temperature on the conversion efficiency of irradiation electrons to NV centers, we fit the above fluorescence data to a simple model. We ignore the influence of other charge traps in the diamond, such as lattice dislocations, and focus on the vacancy concentration created by a given irradiation dose. Electron irradiation creates vacancies V^0 in the diamond which, when trapped by a single substitutional nitrogen N_S^0 , form NV^0 [63]:



Interaction with a nearby N_S^0 induces charge transfer to form NV^- :



We assume three dose ranges in this model: at low irradiation dose, the additional NV centers (both charge states) formed are negligible compared to the initial NV concentration present after diamond synthesis. At intermediate doses, when the vacancy concentration created is

comparable to the nitrogen concentration, the growth in NV concentration is approximately linear. At higher doses, when the vacancies created far exceed the nitrogen content in the diamond, the NV concentration saturates. We ignore the fluorescence at doses higher than $(5 \times 10^{18} \text{ e}^-/\text{cm}^2)$, as it falls outside the scope of this model and is not needed to investigate irradiation to NV conversion. We also assume that the concentration of NV centers is linearly proportional to the fluorescence, which is valid at laser excitation below saturation.

The functional form of the model is

$$f_{NV}(D) = A \left([\text{NV}_i] + [\text{N}_T] \left(1 - \exp \left(-B \frac{D}{(1.76 \times 10^{17} \text{ cm}^{-3}/\text{ppm})[\text{N}_T]} \right) \right) \right), \quad (3.1)$$

where $f_{NV}(D)$ is the total NV fluorescence as a function of irradiation dose D , $[\text{NV}_i]$ is the initial concentration of NV centers in ppm pre-irradiation, $[\text{N}_T]$ is the total nitrogen concentration in ppm in the diamond pre-irradiation, A is a scaling factor to convert from concentration to fluorescence (ppm^{-1}), and B is a parameter relating the conversion of irradiation electrons to NV centers ($\text{V}^0/\text{e}^-/\text{cm}$). To fit the model we fix the initial nitrogen concentration at 0.15 ppm, which is consistent with the typical nitrogen concentrations found in commercially available CVD diamond from Element Six [62]. Figure 3-4 shows an example of the model applied to diamonds incident with 70 mW optical excitation. The two highest doses, also shown in the figure, were not included in the fitting.

Figure 3-5 depicts the fit parameters as a function of excitation power. The initial NV concentration is consistently in the range of 1-10 ppb, corresponding to an N to NV conversion efficiency between 0.6 - 6%. The parameter A increases and shows the beginning of saturation at high excitation powers, which is expected since the assumption that the NV concentration is proportional to the fluorescence is not valid past saturation (calculated to be 5 mW in this experimental setup, see Appendix B). The irradiation to vacancy conversion factor B is roughly constant until powers past 4 mW for both annealing temperatures, at which they both begin to decline. Since this parameter describes the conversion of dose to vacancy concentration, it should not depend on laser power. The decline is probably due the breakdown of the assumption that the fluorescence is proportional to concentration at high powers.

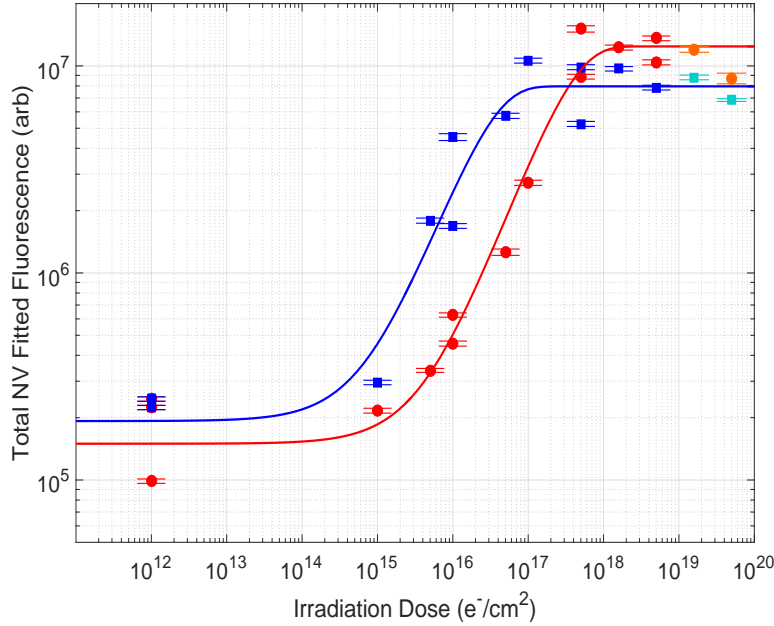


Figure 3-4: Sample model fitting for fluorescence measurements taken at 70 mW excitation power. Red corresponds to 850°C annealing and blue to 1250°C. Note that the two unprocessed diamonds are included in both data sets. The diamonds at doses exceeding $5 \times 10^{18} \text{ e}^-/\text{cm}^2$ are also shown, distinguished from the main data set as these were not used for the fitting.

To analyze the conversion efficiency of irradiation electron dose to NV production, we average the B values for powers less than 6 mW. For 850°C we have $B_{850} = 0.096 \pm 0.028 \text{ V}^0/\text{e}^-/\text{cm}$ and for 1250°C we have $B_{1250} = 1.347 \pm 0.601 \text{ V}^0/\text{e}^-/\text{cm}$. That is about 0.1 vacancies are formed per 1 ME electron per centimeter at 850°C, while about 1.3 vacancies are created per electron at 1250°. As mentioned above, one explanation for the higher B value is the greater diffusion vacancies experience at higher temperatures.

3.4.3 Total Fluorescence vs. Optical Power

The total fluorescence of each NV charge state is plotted against optical excitation power for 850°C annealing in Figure 3-6 and for 1250°C annealing in figure Figure 3-7¹ Both charge

¹Note that Bascom ($5 \times 10^{17} \text{ e}^-/\text{cm}^2$, 850°C anneal), whose PL spectra serves as the NV⁰ basis function, shows a decrease in fluorescence with higher power; this is a systematic error that can be fixed with a refinement of the basis functions. For the entire thesis, data for Bascom at high laser power deviates from expected trends due to this systematic error.

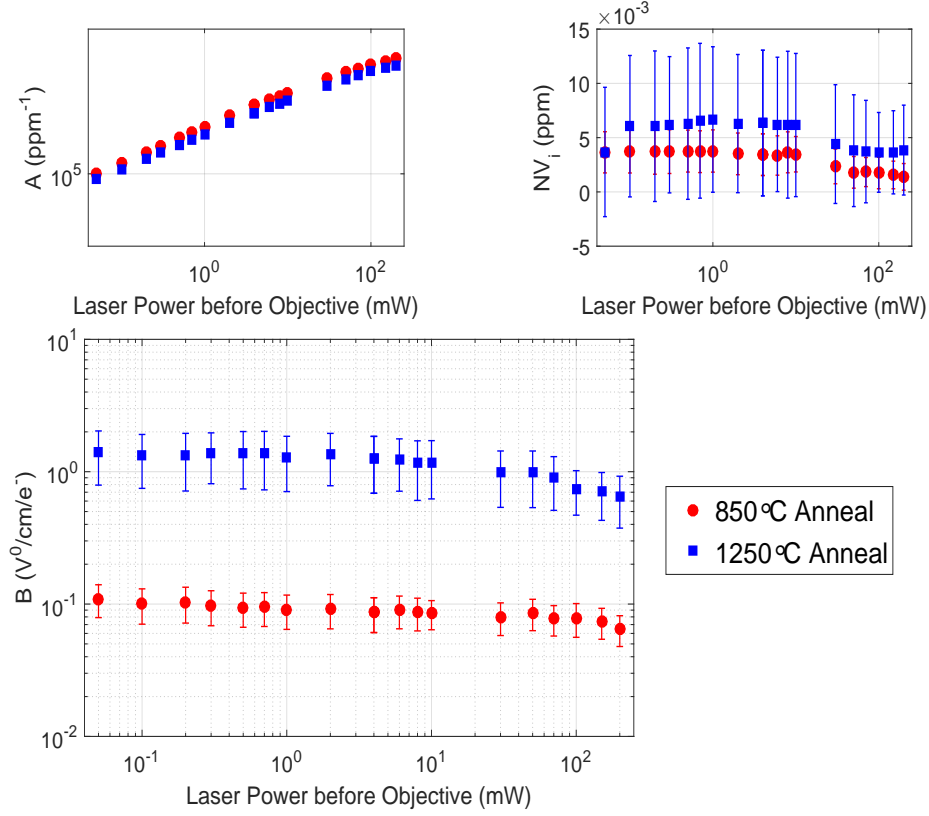


Figure 3-5: Fitting parameters for the fluorescence model as a function of laser power. The initial nitrogen concentration N_T is fixed at 0.15 ppm. For all plots, the error bars are extracted from the 68% confidence intervals obtained from the fitting; those associated with A are encompassed within the points.

states show the beginning of saturation in fluorescence as the optical power is increased. To determine what the saturation power is, we fit a simple model[19] the fluorescence f of each charge state to the form

$$f(P) = A \frac{P}{P + P_{sat}}, \quad (3.2)$$

where P is the laser power measured before the objective, P_{sat} is the saturation power, and A is a fitting parameter.

Figure 3-8 shows two examples of this fit. For the diamond Bohr ($5 \times 10^{17} \text{ e}^-/\text{cm}^2$, 1250°C anneal) the NV^0 saturation power is extracted to be $P_{sat,0} = 160 \text{ mW}$ and for NV^- is $P_{sat,-} = 9.2 \text{ mW}$. Similarly, for the diamond Lorentz ($5 \times 10^{18} \text{ e}^-/\text{cm}^2$, 1250°C anneal) $P_{sat,0} = 158 \text{ mW}$ and $P_{sat,-} = 55 \text{ mW}$. A significant number of diamonds do not

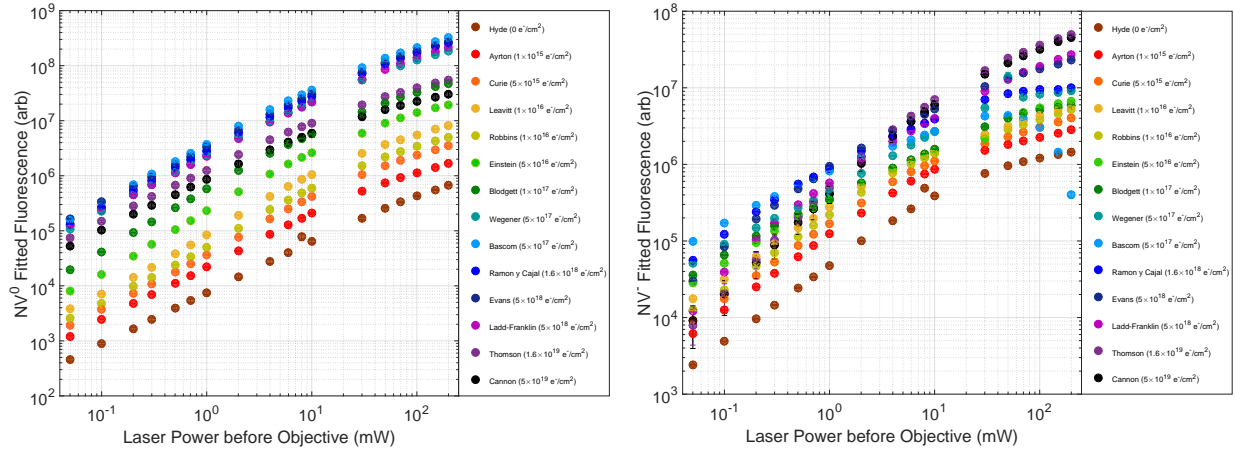


Figure 3-6: NV fluorescence vs. optical excitation power of all diamonds annealed at 850°C for the (left) neutral charge state and (right) negative charge state.

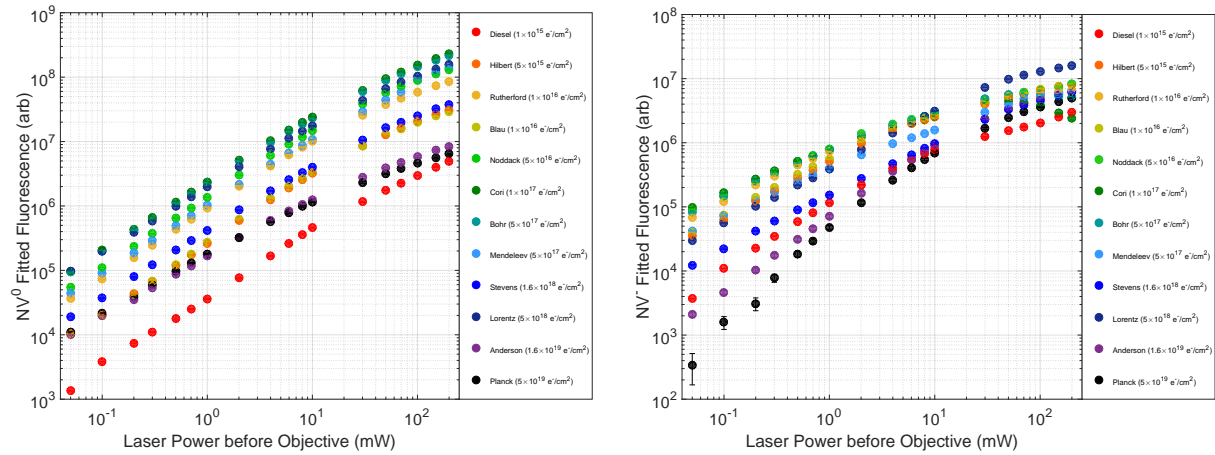


Figure 3-7: NV fluorescence vs. optical excitation power of all diamonds annealed at 1250°C for the (left) neutral charge state and (right) negative charge state.

fit the saturation model above, like Bohr. For diamonds where the saturation model was successful, the saturation powers of NV^- were all higher than the calculated 5 mW for this experimental setup. This suggests that saturation may not be the only mechanism occurring at high excitation power. Further analysis into the charge state dynamics, and perhaps fluorescence measurements on a smaller imaged fluorescence region (see Appendix B), is needed to explain this discrepancy.

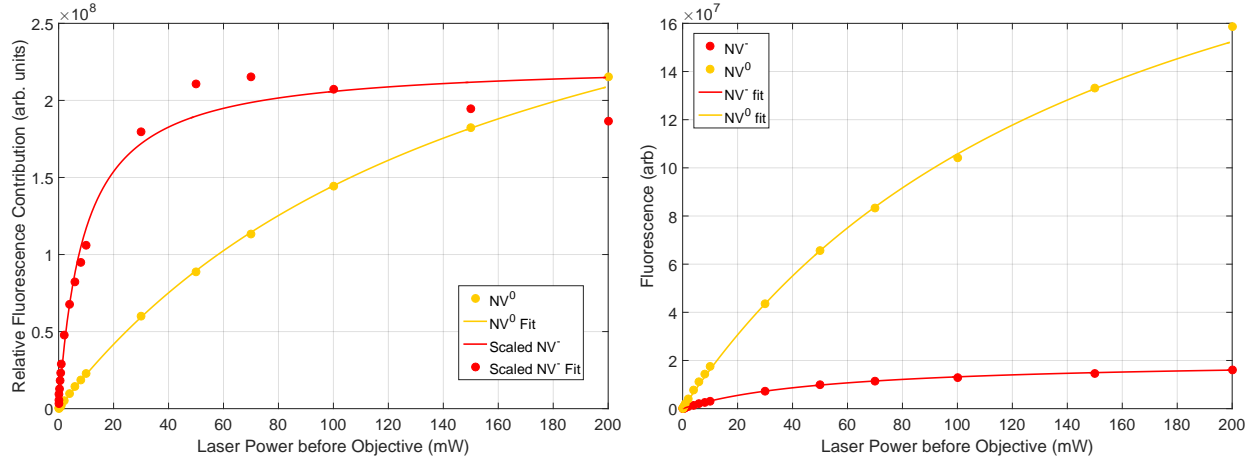


Figure 3-8: Saturation model fitting for (left) Bohr (5×10^{17} e⁻/cm², 1250°C anneal) and (right) Lorentz (5×10^{18} e⁻/cm², 1250°C anneal). The NV^- curve for Bohr is scaled for comparison with NV^0 .

3.4.4 Charge State Fluorescence Ratio vs. Irradiation Dose

We now analyze the contrast α by looking at the charge state fluorescence ratio of NV^- to NV^0 . This is obtained from the ratio of the fitting coefficients of NV^- to NV^0 . Figure 3-9 shows the charge state fluorescence ratio versus irradiation dose D over four orders of magnitude of laser power. For clarity the data from two annealing temperatures are plotted separately. For all laser powers, the ratio decreases for doses up to 1×10^{18} e⁻/cm². For doses past 1×10^{18} e⁻/cm², excitation power dependence arises. At low laser power the ratio either continues to decrease or levels off; for higher laser power the ratio increases. At low doses the drop in ratio can be attributed to the increase in NV^0 production as more vacancies pair off with N_S , which decreases the number of electron donors to form NV^- . The behavior at high dose is not expected: similar to the quenching of fluorescence at these

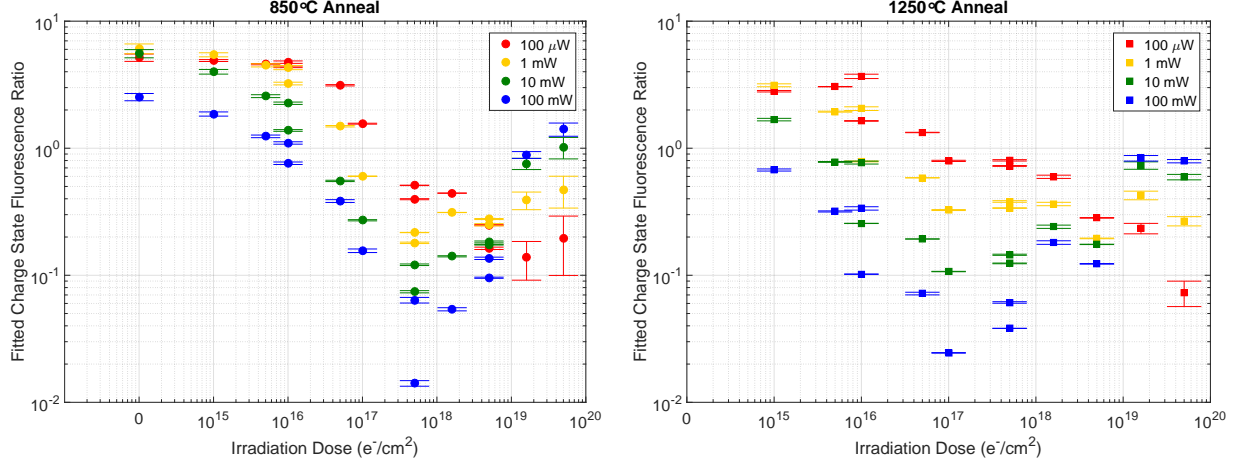


Figure 3-9: Charge state fluorescence ratio NV^-/NV^0 vs. irradiation dose over four orders of magnitude for diamonds that underwent (left) 850°C annealing treatment (right) 1250°C annealing treatment.

same doses seen in Section 3.4.1, something is causing the charge state ratio to increase. As mentioned earlier, the production of a vacancy-related defect could be the cause, if it were to influence the charge switching dynamics between NV^- and NV^0 . This influence would increase at higher laser power, as seen in the next section.

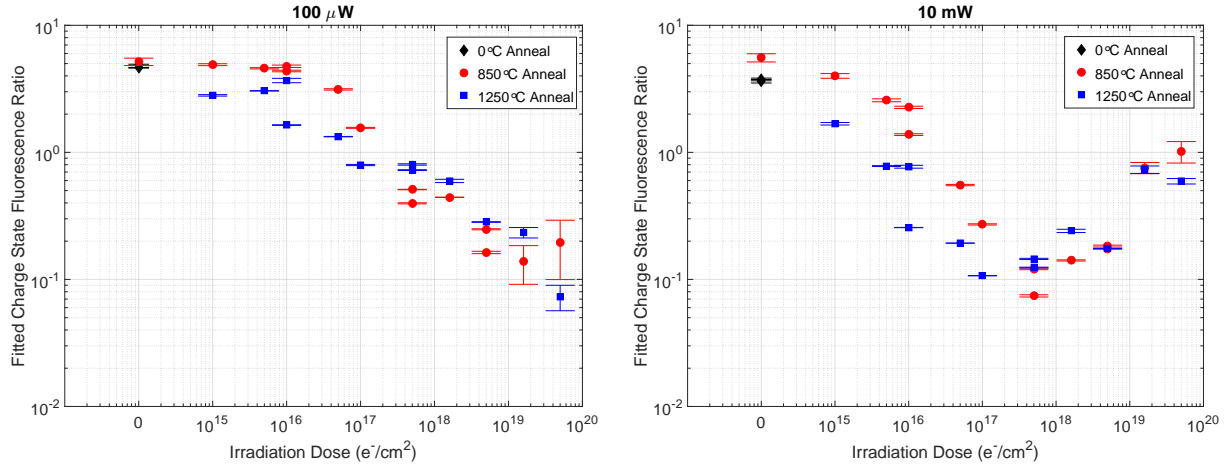


Figure 3-10: Charge state fluorescence ratio NV^-/NV^0 vs. irradiation dose for all diamonds at (left) 100 μ W of laser excitation before the objective and (right) 10 mW.

To see the effects arising from the different annealing temperatures, we look at both temperatures simultaneously. Figure 3-10 shows the charge state fluorescence ratio as a function of electron irradiation dose for all 28 diamonds at low (100 μ W) and high (10 mW)

excitation power. For doses below $5 \times 10^{17} \text{ e}^-/\text{cm}^2$, diamonds annealed at 850°C generally had a higher ratio than those annealed at 1250°C . This decrease can be attributed to a decrease in charge donors needed to create NV^- . This agrees with the vacancy diffusion discussion above, where it was hypothesized that the vacancies created during irradiation diffuse farther away from their initial location, which increases their probability to be trapped by a nitrogen atom. This led to a higher total NV fluorescence at lower doses. For the charge state fluorescence ratio, the creation of more NV centers at lower doses means NV^0 is also being created, which means the ratio should be lower. Another explanation could be the creation of stable defects at this annealing temperature that are stable charge traps, robbing electrons needed for NV^- to form.

3.4.5 Charge State Fluorescence Ratio vs. Optical Power

We finish our characterization of the charge state fluorescence by looking at the charge state fluorescence ratio as a function of excitation power. The charge state fluorescence ratio is plotted as a function of laser power for both annealing temperatures in Figure 3-11. For doses below $1 \times 10^{16} \text{ e}^-/\text{cm}^2$ for 850°C , $5 \times 10^{15} \text{ e}^-/\text{cm}^2$ for 1250°C , and for the two unprocessed diamonds (not shown) the ratio slightly increases at first but then falls off with higher excitation power. For doses up to 1×10^{18} the ratio decreases monotonically for all excitation powers. This is consistent with the literature, where increase laser intensity ionizes NV^- to NV^0 [19, 51, 64]. At doses above $1 \times 10^{18} \text{ e}^-/\text{cm}^2$, however, the magnitude of the ratio begins to increase at the higher laser power (but still decreases as laser power increases), and then for both anneal temperatures the two diamonds with doses above $1 \times 10^{19} \text{ e}^-/\text{cm}^2$ the result is notable: the charge state fluorescence ratio increases with the laser excitation. Like the increase in ratio with laser power seen in the last section, this is contrary to what we expect. Figure 3-12 shows the PL spectra of Cannon ($5 \times 10^{19} \text{ e}^-/\text{cm}^2$, 850°C anneal) at all laser powers used. As the excitation power increases the ZPL of NV^- is increasingly distinguishable from the NV^0 phonon sideband.

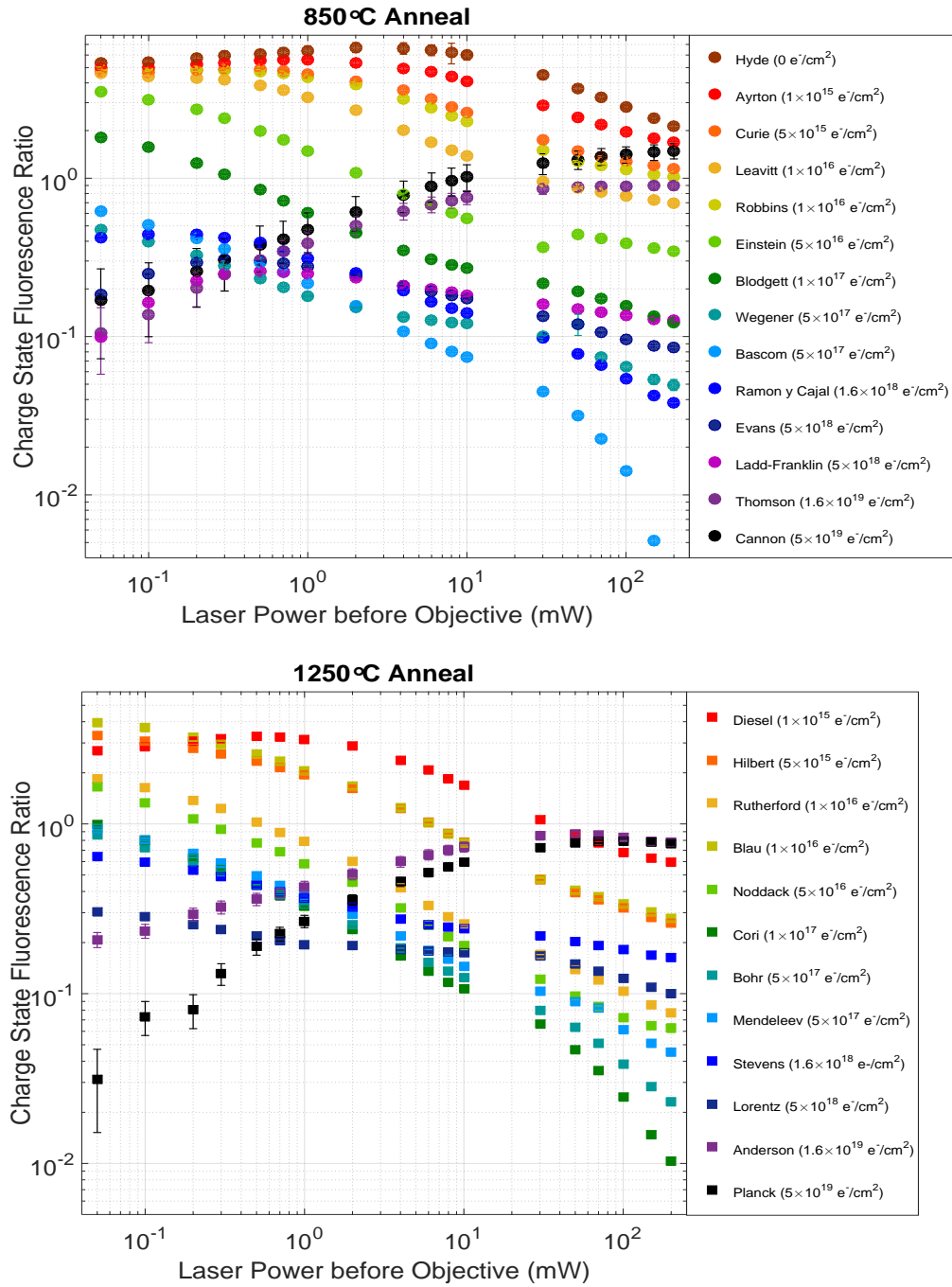


Figure 3-11: Charge state fluorescence ratio NV^-/NV^0 vs. optical excitation power as measured before the dichroic mirror in the setup. (top) 850°C annealing treatment (bottom) 1250°C annealing treatment.

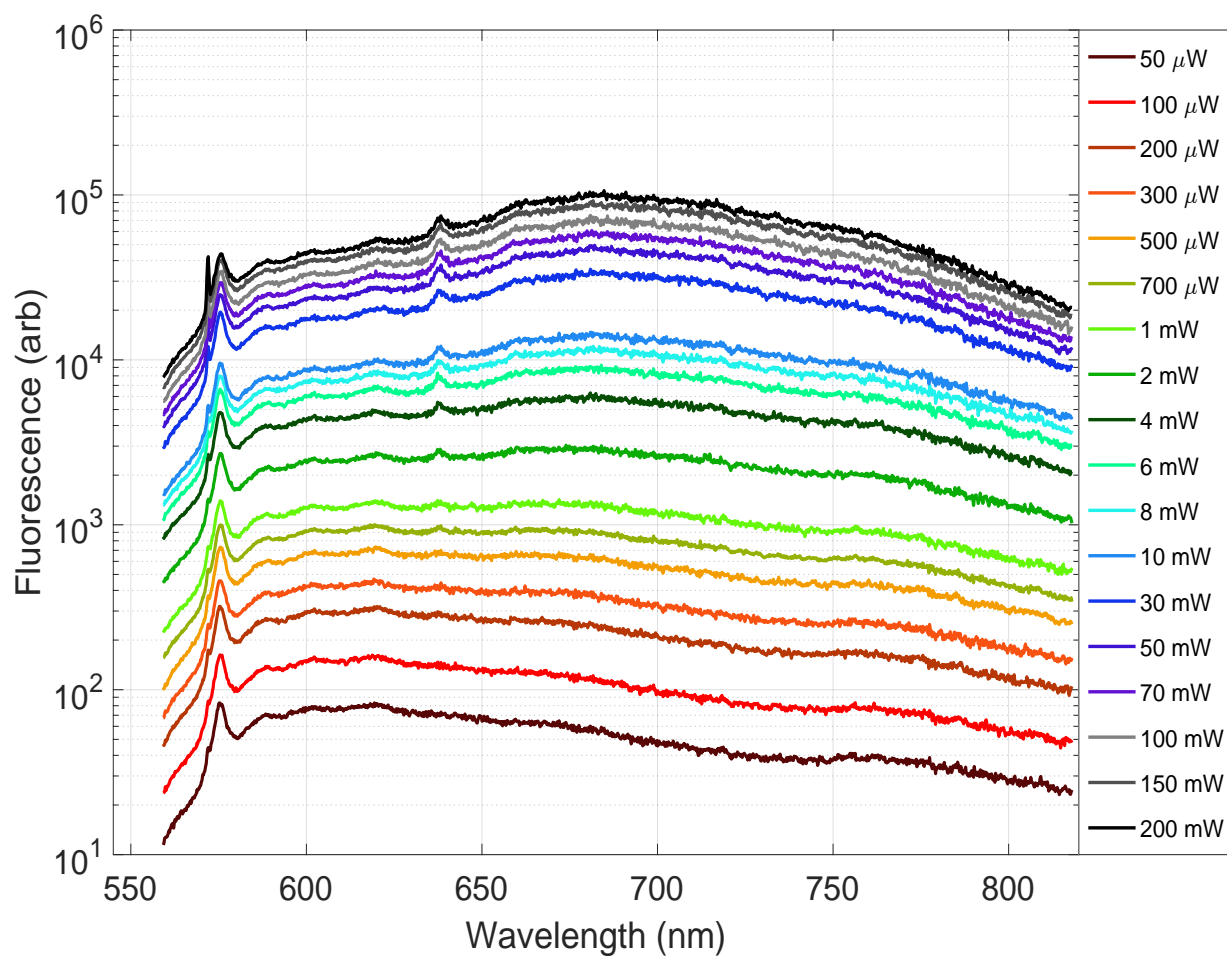


Figure 3-12: Photoluminescence spectra of the diamond Cannon ($5 \times 10^{19} \text{ e}^-/\text{cm}^2$, 850°C anneal) at all laser powers. Contrary to diamonds irradiated at a lower dose, the NV⁻ contribution to the PL spectra increases as a function of laser power.

3.5 Conclusion

In this chapter, we have described the role that fluorescence from NV^0 and NV^- play in NV magnetometry. Photoluminescence spectra of each diamond were measured for laser intensities spanning over four orders of magnitude and fit to a linear combination of individual charge state spectra. From this fitting we calculated the total NV fluorescence and charge state fluorescence ratio. For irradiation doses below $1 \times 10^{18} \text{ e}^-/\text{cm}^2$ the behavior of each quantity agreed with a simple picture of adding more vacancies to a fixed concentration of nitrogen. The total fluorescence from both charge states increases with dose as more NV centers are created until saturating as the vacancy concentration is believed to exceed that of nitrogen. Similarly, the charge state fluorescence ratio decreases with dose as the available substitutional nitrogen electron donors are used to form more NV^0 centers. For different annealing temperatures, a simple model of fluorescence vs. dose revealed a factor of ~ 10 increase in irradiation electron to NV conversion efficiency for 1250°C annealed diamonds over 850°C , which is attributed to the higher diffusion rate of vacancies during higher temperatures. This allows more vacancies to be trapped by nitrogen atoms for a given dose; it also explains the lower charge state fluorescence ratio for 1250°C at low dose.

At higher irradiation doses the data behave contrary to what is expected from our simple model. The total fluorescence is quenched with the addition of more vacancies, and the charge state fluorescence ratio increases. Even more striking are the diamonds at $1.6 \times 10^{19} \text{ e}^-/\text{cm}^2$ and $5 \times 10^{19} \text{ e}^-/\text{cm}^2$, which show a monotonic increase in charge state fluorescence ratio under increased laser excitation, contrary to the expected ionizing role provided high laser intensities. It is proposed that these trends can be attributed to effects lying outside the picture of only nitrogen and monovacancies existing in the lattice, as the NV fluorescence would not decrease past its saturated value, nor would the charge state fluorescence ratio increase with the addition of more vacancies (NV^- would ideally not exist at all in the lattice in the absence of optical illumination). High irradiation doses are known to give rise to vacancy chains and other vacancy-related defects [38, 55]. These defects could act as charge donors to increase the NV^- fluorescence under illumination. In addition, the defects could include nitrogen atoms to form defect complexes, which would decrease the

total concentration of NV centers and thus the total fluorescence. Further characterization of defects present in the highly-irradiated diamonds is required.

This data serves as the basis to characterize the collected photons β and fluorescence contrast α for each diamond. However, before we can analyze the relative magnetic sensitivity of each diamond, the coherence time scales must also be measured.

Chapter 4

Coherence Time Characterization

4.1 Overview

To characterize an ensemble of color centers for magnetometry, knowledge of the coherence times is required. By analogy with nuclear magnetic resonance spectroscopy, ensembles are characterized by two decay times, namely T_1 and T_2 [67]. The relaxation time T_1 describes population decay to the ground state, while the dephasing time describes the randomizing of phase between two eigenstates. The dephasing time is separated into two categories: the inhomogeneous spin-dephasing time T_2^* characterizes the influence of inhomogeneities in the environment, such as temporal fluctuations in the local magnetic field and variations in the local spin environment of each NV center. The homogeneous spin-dephasing time T_2 , or spin-decoherence time, characterizes the intrinsic spin environment apart from the influence of external inhomogeneities (such as applied MW and static fields). Static dephasing influences are “focused” out in measuring the T_2 time, as explained below. Different magnetometry protocols depend on different coherence time scales.

In this chapter, we characterize the coherence times of NV ensembles by measuring the three time scales T_2^* , T_2 , and T_1 . The role coherence time plays in the sensitivity equation and the different AC and DC magnetometry regimes will be discussed. The emphasis in this thesis will be on T_2 measurements; preliminary T_2^* and T_1 measurements will also be shown. For T_2 an empirical model of the dependence of irradiation dose will be presented.

4.2 Coherence Time and Magnetometry

As discussed in Chapter 2, magnetic sensitivity ($\eta \approx 1/\alpha\sqrt{\beta T}$) depends on the fluorescence contrast α , total fluorescence β , and NV interrogation time T . High-sensitivity magnetometry benefits from long coherences, which approach the sampling time of the measurement. The NV ensemble, however, can only maintain phase coherence for a finite time before the surrounding noise bath of the environment causes ensemble decoherence. Past these time-scales the contrast α of the NV fluorescence degrades, yielding a net loss in sensitivity. Optimizing these time scales is thus critical to an NV magnetometer.

The first time scale, which is relevant for DC magnetometry, is the inhomogeneous spin-dephasing time T_2^* . The two most common schemes to measure low frequency magnetic fields, CAW-ODMR and Ramsey, both depend on this time scale: for CAW-ODMR the linewidth of the measured resonances scales as $\sim 1/T_2^*$, while for Ramsey-based methods, the NV ensemble can only maintain phase coherence during the free precession time at time scales equal to or less than T_2^* . The magnetic field sensitivity in both of the above schemes are thus optimized when the measurement time T is of similar duration as the inhomogeneous spin-dephasing time T_2^* [7, 30]. The physical mechanism for spin-dephasing is a result of spatial and temporal field inhomogeneities experienced by each NV center. For high-purity (low nitrogen concentration, less than 10 ppm [48]) diamond with a natural abundance of ^{13}C (1.1%), the dominant source of dephasing arises from the hyperfine dipolar coupling of the NV electronic spin with the ^{13}C nuclear spin. Dipolar interactions with electron spins from nitrogen impurities (including other NV centers) also contribute to dephasing.

In AC magnetometry schemes, the relevant time scale shifts from T_2^* to T_2 . Tailored pulse sequences can be used to refocus static/low frequency dephasing influences in the environment, which extends the ability to maintain phase coherence to the longer spin-decoherence time T_2 . For NV ensembles, T_2 can exceed T_2^* by a factor of 100 [68]. Similar to the DC sensing scheme, an AC measurement time of $T \sim T_2$ yields the optimal sensitivity. Like T_2^* , contributors to decoherence are dipolar coupling to the ^{13}C nuclei and other paramagnetic impurities, such as the electron spins from single substitutional nitrogen.

Finally, the third time scale to consider is the spin-lattice relaxation time T_1 . This time

scale characterizes the time for the NV ensemble to decay to the thermal equilibrium state. This is the result of interactions with lattice phonons that cause spin-flips. Ultimately T_2 is limited to $2T_1$, but it is beyond the scope of this thesis to pursue methods of improving T_1 in our diamonds.

The remainder of this chapter will discuss the various pulse sequences used to measure the three coherence-times discussed above, with an emphasis on the spin-decoherence time T_2 . Each section first details the measurement procedure and then the experimentally-acquired results. The experimental measurements taken before each coherence time measurement (magnetic bias field alignment to an NV axis, determination of the resonances, etc.) is found in Appendix C.

4.3 Spin-Dephasing Time T_2^* Measurements

4.3.1 Measurement Procedure

The method to measure T_2^* is based on the Ramsey pulse sequence (see Figure 4-1 (top)), where after optical pumping to the $|0\rangle$ electronic ground state, $|0\rangle$, a microwave (MW) $\pi/2$ pulse (calibrated by a Rabi measurement, see Appendix C) projects the NV spin into a superposition of $|0\rangle$ and $|-1\rangle$ (where a static field B_0 is applied to split the $|\pm 1\rangle$ states). The NV spin ensemble precesses about the static field during a free precession time τ . A second MW $\pi/2$ pulse projects the spin back into the $\{|0\rangle, |-1\rangle\}$ basis (or manifold) where the single-photon counter (SPCM) measures the fluorescence m_1 with a gate pulse. The sequence is repeated again, except a MW $3\pi/2$ pulse is applied at the end instead of a MW $\pi/2$ pulse and fluorescence m_0 is recorded. The two signals are subtracted and normalized to form the signal $s = (m_1 - m_0)/(m_1 + m_0)$ to cancel out common-mode noise.

The envelope of the signal s is modeled as a stretched exponential with stretching parameter p :

$$s(\tau) = \exp[(-\tau/T_2^*)^p] \sum_{i=1}^3 \cos(2\pi f_i \tau - \phi_i), \quad (4.1)$$

where τ is the free precession time, f_i are the detunings from the three NV hyperfine resonances that were determined by a Fast-Fourier Transform of the Ramsey fringes, ϕ_i are

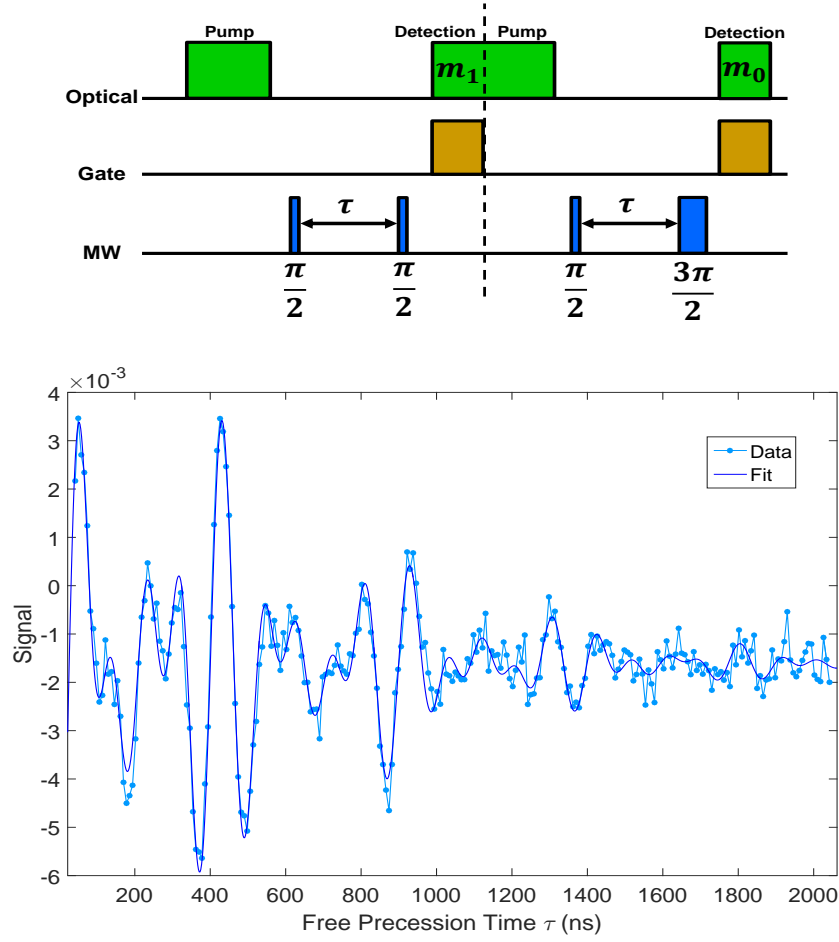


Figure 4-1: (top) Ramsey pulse sequence used to measure spin-dephasing time T_2^* . (bottom) Example Ramsey curve from the diamond Rutherford (1×10^{16} e $^-$ /cm 2 , 1250°C anneal), where the calculated spin-dephasing time is $T_2^* = 719 \pm 41.6$ ns.

phase shifts, and p is the stretched exponential factor. Figure 4-1 (bottom) shows a sample measured signal. The detuning of the MW field from the three hyperfine resonances creates the beating modulation of the signal. To observe enough Ramsey fringes before dephasing diminishes the signal, the MW drive was detuned by 8 MHz from the central NV hyperfine resonance, with the shortest detuning (6 MHz) having a period of about 167 ns.

4.3.2 Results and Limitations

Coherence measurements were carried out on the matrix of irradiated diamond in Table 2.1. Figure 4-2 shows the measured T_2^* values. Note that Mendeleev ($5 \times 10^{17} \text{ e}^-/\text{cm}^2$, 1250°C anneal) and Cannon ($5 \times 10^{19} \text{ e}^-/\text{cm}^2$, 850°C anneal) were excluded due to insufficient signal-to-noise. Error bars are extracted from the 68% confidence intervals obtained from the dephasing curve fitting. These values lower bounds to the intrinsic T_2^* of the diamond, which for dilute nitrogen concentrations is limited mainly by the dipolar interactions of ^{13}C to be about $1 \mu\text{s}$ [1]. Preliminary measurements did not address magnetic field inhomogeneity and temperature fluctuations, which may limit the effective spin-dephasing times reported. Further investigation is needed to determine if the T_2^* values are limited by either irradiation and annealing effects or systematic effects.

Other methods exist to measure T_2^* . (1) Pulsed-ODMR operates similar to CAW-ODMR (see Appendix C) by measuring the fluorescence of the NV ensemble at or near resonance, but the laser is switched off during pulsed MW excitation. By reducing the MW power and adjusting the MW π pulse, the natural linewidth $\Delta\nu$ can be extracted from the fluorescence lineshape. Avoiding laser power broadening, the spin-dephasing time is then $T_2^* = 1/(\pi\Delta\nu)$ [30]. Pulsed-ODMR (like Ramsey) has the advantage of eliminating laser power broadening, which allows the laser excitation to be set high to increase the fluorescence signal. This method can also be utilized through CAW-ODMR. (2) Another method to measure T_2^* takes advantage of the full spin-1 nature of the NV center and observe quantum beating between bright and dark superposition states of $|\pm 1\rangle$ magnetic sublevels [69]. The advantage of this method is to eliminate the role of temperature and strain-dependent zero-field frequency [70] by measuring a beat frequency defined only in terms of the external magnetic field and fundamental constants. Realizing this for NV ensembles is more challenging, however,

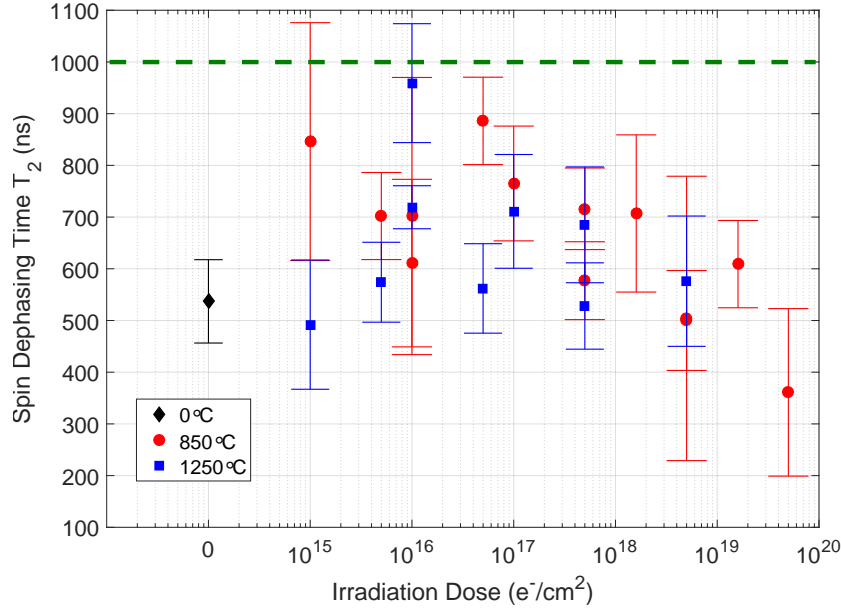


Figure 4-2: Spin-dephasing times T_2^* as a function of dose measured with the Ramsey pulse sequence. Due to environmental factors that were not explicitly controlled, these values are to be seen as a lower bound of the intrinsic T_2^* of the diamond, not limited by external environmental factors. the dotted line indicate the expected ^{13}C -limited $T_2^* = 1 \mu\text{s}$ [1].

because only one NV axis can be addressed at a time and both $|1\rangle \leftrightarrow |0\rangle$ and $|-1\rangle \leftrightarrow |0\rangle$ resonances need to be driven at the same time.

4.4 Spin-Decoherence Time T_2 Measurements

4.4.1 Measurement Procedure

The Spin-echo (also known as Hahn Echo) sequence (see Figure 4-3 (top)), which is used to measure T_2 , builds on the Ramsey pulse sequence by inserting an additional MW π pulse between the $\pi/2$ pulses. As in the Ramsey sequence, after optical pumping to the $|0\rangle$ electronic spin state the NV spin ensemble is prepared into a superposition of the $|0\rangle$ and $|-1\rangle$ states with a $\pi/2$ pulse. The spin ensemble then acquires phase from the environment during a free precession time of length $\tau/2$. An additional MW π pulse is applied and switches the sign of the phase accumulation for the second free precession time. For static magnetic fields, this means that any phase accumulated before the MW π pulse is “echoed”

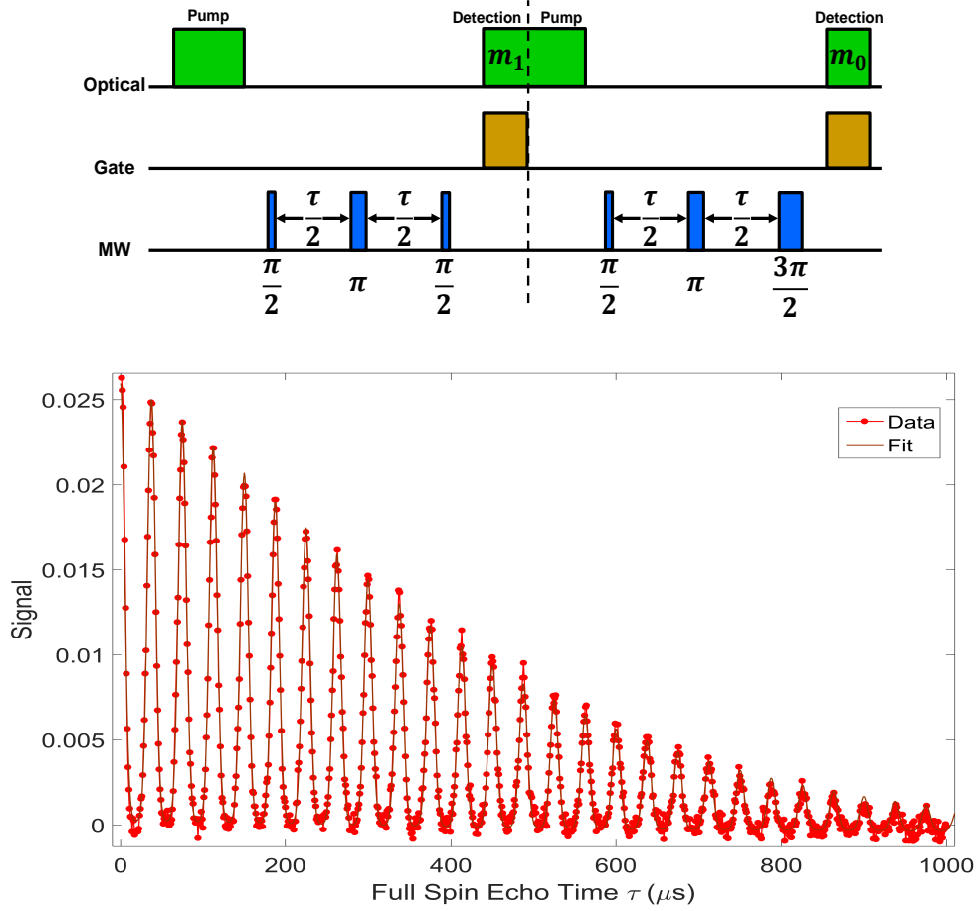


Figure 4-3: (top) Pulse sequence used to measure the spin-decoherence time T_2 . (bottom) Example signal from the diamond Noddack ($5 \times 10^{16} \text{ e}^-/\text{cm}^2$, 1250°C anneal), where the calculated spin-decoherence time is $T_2 = 450 \pm 2.59 \mu\text{s}$. The collapses and revivals in the signal are due to the Larmor precession of ^{13}C nuclei in the surrounding environment.

out after. Phase accumulation from local magnetic field fluctuations is also cancelled out ('refocused') assuming they do not vary appreciably on the time scale of the free precession. Precessing again for a time $\tau/2$, a second MW $\pi/2$ pulse rotates the spin ensemble back into the $\{|0\rangle, |-1\rangle\}$ basis and a gate pulse from the SPCM records fluorescence m_1 . As in Ramsey measurements, the readout pulses alternates between $\pi/2$ and $3\pi/2$ and output signals from m_0 and m_1 are subtracted to remove common-mode noise.

Figure 4-3 (bottom) shows a sample spin-echo signal. The collapses and revivals in the echo signal owe to the natural abundance (1.1%) of ^{13}C nuclei in the lattice environment. Free to rotate in its lattice site, ^{13}C experiences Larmor precession due to the static magnetic

field B_0 . This causes a periodic fluctuation in the interaction between the nuclei and the NV spin, thus leading to an oscillating phase accumulation during the echo cycle [1, 71]. If the free precession time $\tau/2$ coincides with an integer multiple of the Larmor period T_L , then the net phase accumulation from the ^{13}C interaction is cancelled out, leading to a revival in the fluorescence signal. Other precession time intervals lead to modulation of the echo signal, alternating between collapses and revivals. Eventually, weak dipole-dipole interactions between pairs of ^{13}C nuclei and between ^{13}C nuclei and spins of paramagnetic impurities induce flip-flops in the interaction between the NV spin and ^{13}C nuclei, leading to decoherence [72]. To ensure that all ^{13}C nuclei precess at the same frequency, special care is taken to ensure zero misalignment of the static magnetic field with the NV symmetry axis. A transverse static field induces anisotropic-hyperfine coupling between the NV spin and the ^{13}C nuclei [73], causing a position-dependent precession frequency and thus the disappearance of the collapses and revivals, and a reduction in the decoherence time T_2 .

The envelope of the signal is modelled as a stretched exponential $e^{-(\tau/T_2)^p}$ with stretching parameter p . For a single NV $p = 3$ [74], but for ensembles p usually varies between 0.5 and 3 [73]. The curve fits for our diamonds yielded $0.5 < p < 2$. The collapses and revivals in the fluorescence signal due to the ^{13}C nuclei is theoretically a fourth-power sinusoid [75] for a single NV spin, but we used a linear combination of Lorentzian and Gaussian shapes for each revival to modulate the stretched exponential. From this fit we extract T_2 :

$$s(\tau) = A_0 + A_1 \exp[(-\tau/T_2)^p] \sum_{n=1}^N \left(Bg_n e^{-(\tau - nt_r)^2/(2G_g^2)} + \frac{Bl_n}{(\tau - nt_r)^2 + \left(\frac{G_l}{2}\right)^2} \right), \quad (4.2)$$

where $A_0, A_1, Bg_n, Bl_n, G_g, G_l$ are fit parameters, t_r is the revival time of first revival, and n ranges from 1 to the number of revivals N in the signal.

4.4.2 Results

Figure 4-4 gives the measured T_2 values for all the diamonds. The error bars are extracted from the 68% confidence intervals obtained from the decoherence curve fitting. For irradiation doses up to $1 \times 10^{18} \text{ e}^-/\text{cm}^2$, T_2 ranges from over 380 - 460 μs ; after this dose the values begin to decline. It is interesting to note that this dose is also where the fluorescence and

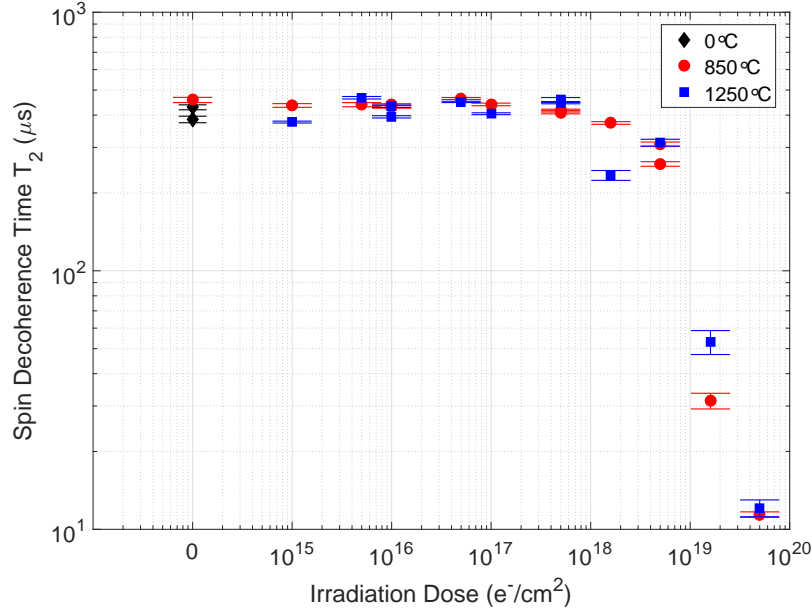


Figure 4-4: Spin-decoherence times T_2 for all diamonds as a function of irradiation dose.

charge state fluorescence ratio also begin to change behavior as seen in chapter Chapter 3; past this dose, the total NV fluorescence begins to decline and the charge state fluorescence ratio begins to increase relative to lower doses at high laser excitation. The nitrogen content (~ 0.15 ppm) and ^{13}C content of the diamonds is the same, which is expected to be the reason for the uniformity of T_2 at low doses. Past $1 \times 10^{18} \text{ e}^-/\text{cm}^2$, however, T_2 is no longer limited by the substitutional nitrogen or ^{13}C concentration in the diamond. Further investigation is needed to elucidate the nature of this new limiting mechanism. One possible cause could be the creation of paramagnetic vacancy-related defects at these high doses [47, 55], which couple to the NV center to induce decoherence at a faster rate than ^{14}N and ^{13}C . Electron paramagnetic resonance (EPR) spectroscopy is a technique to identify paramagnetic defects; measuring EPR spectra for the high dose diamonds and comparing to the literature would indicate what defects are formed.

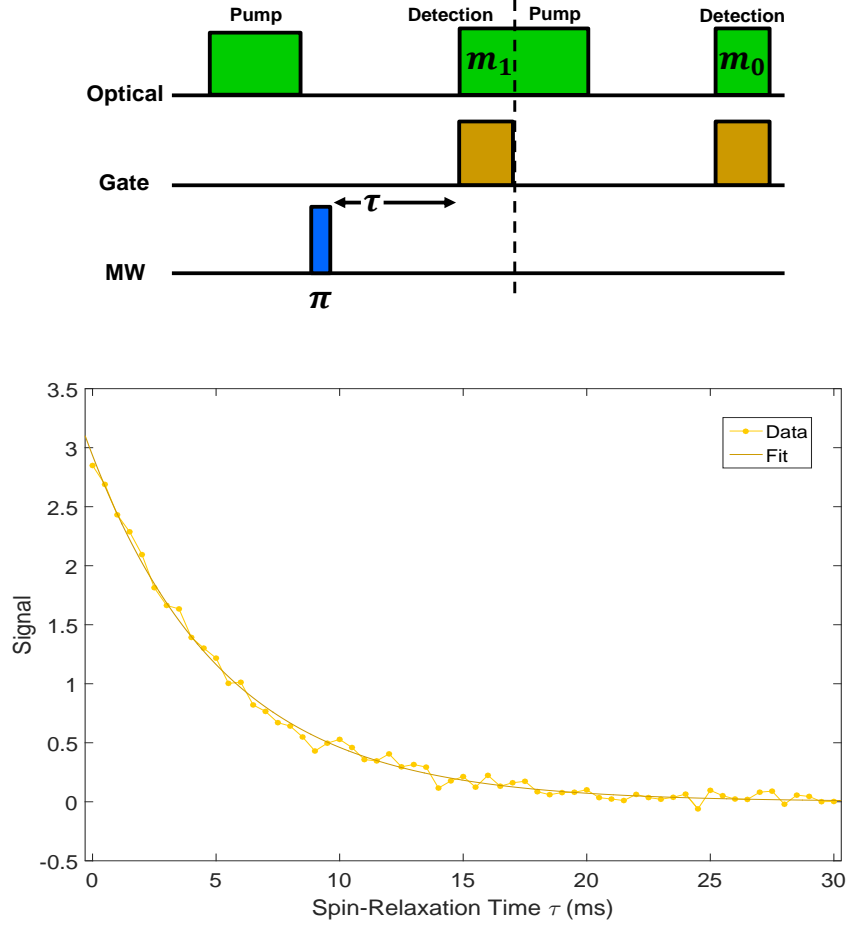


Figure 4-5: (top) Pulse sequence used to measure the spin-relaxation time T_1 . (bottom) Example signal from a spin-relaxation pulse sequence, where the calculated spin-relaxation time is $T_1 = 5.4 \pm 0.0751$ ms.

4.5 Spin-Lattice Relaxation Time T_1 Measurements

4.5.1 Measurement Procedure

To measure T_1 time scales, the pulse sequence depicted in Figure 4-5 is employed. After being pumped to the $|0\rangle$ state, a resonant MW π pulse flips the spin to the $|-1\rangle$ state and is allowed to relax toward the thermal equilibrium mixed state over a variable time τ , yielding the fluorescence trace m_1 . The NV ensemble is then pumped back to $|0\rangle$ and allowed to relax again to thermal equilibrium with no MW pulse, giving the fluorescence trace m_0 .

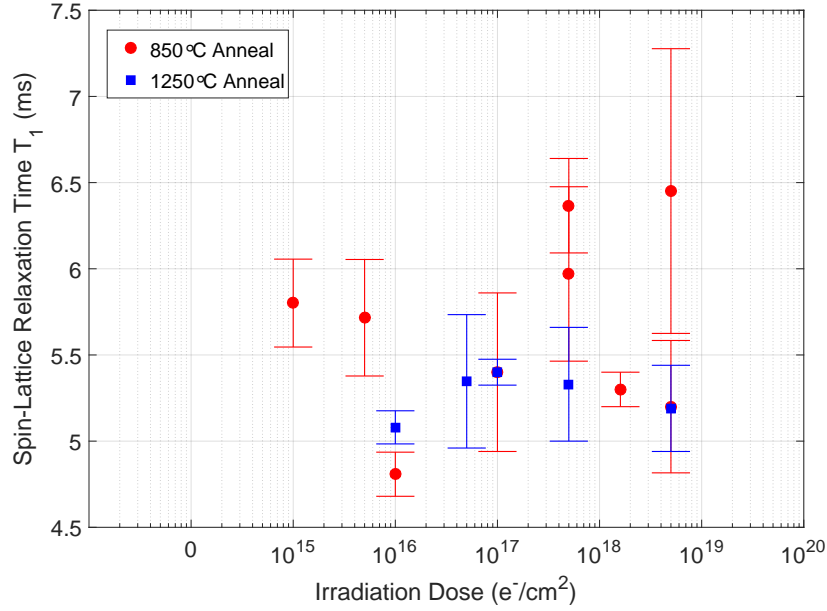


Figure 4-6: Spin-lattice relaxation times T_1 as a function of dose. All diamonds that had T_1 measurements under high laser excitation and experienced partial re-polarization during relaxation are omitted.

4.5.2 Results and Limitations

To form the signal and calculate spin-lattice relaxation, we form the population difference $m_0 - m_1$. This follows a simple exponential profile with decay time T_1 . Similar to the spin-echo and Ramsey measurements, the subtraction of the signals eliminates common-mode noise from laser fluctuations during the measurement and the common fluorescence from the NV orientations not addressed by the MW π pulse. Figure 4-6 shows the values of T_1 as a function of irradiation dose. The error bars are extracted from the 68% confidence intervals obtained from the spin-relaxation curve fitting. The spread in error bars are the result of a spread of differing measurement times; smaller error bars correspond to more averages of a T_1 measurement (the error bars themselves arise from the confidence interval exponential fitting parameter b in the signal $s = ae^{-b\tau}$). No clear trend can be seen in these measurements, which suggest that T_1 is not strongly affected by irradiation and annealing.

4.6 Conclusion

In this chapter, we have described the role that various decoherence time scales play in NV magnetometry. For characterizing the diamonds for AC magnetometry, the spin-decoherence time T_2 was measured with a spin-echo pulse sequence. For diamonds in this study, irradiation doses greater than $1 \times 10^{18} \text{ e}^-/\text{cm}^2$ limit coherence beyond the limit imposed by substitutional nitrogen and ^{13}C alone. Similarly, for DC magnetometry, we measured the spin-dephasing time T_2^* using a Ramsey pulse sequence. The measured T_2^* times fall below the $1 \mu\text{s}$ limit imposed by ^{13}C , either due to systematic effects in the experiment and/or to effects imposed by irradiation and annealing. Further measurement of T_1 and T_2^* will be the focus of future work.

Chapter 5

Analysis and Outlook

5.1 Overview

Using the fluorescence and coherence measurements discussed in previous chapters of this thesis, we now determine the optimum diamond processing regime for commercially available CVD diamonds suited for NV ensemble magnetometry. A simple model is introduced to calculate the magnetic sensitivity figure of merit of each diamond. A discussion of the results is followed by proposed follow-on experiments to achieve a deeper understanding of the data.

5.2 Sensitivity Figure of Merit

5.2.1 Modelling the Sensitivity

So far in this thesis we have only discussed the behavior of the fluorescence and coherence time separately as a function of optical excitation power and irradiation dose. The original question of this study, however, deals with their combined effect on magnetic sensitivity of an NV ensemble magnetometer. Recall that the magnetic sensitivity equation $\eta \sim 1/\alpha\sqrt{\beta T}$ depends on the fluorescence contrast α , photons collected during measurement β , and the measurement time T (optimized when set on the order of T_2^* for DC and T_2 for AC magnetometry). For our commercially available bulk CVD, high purity (150 ppb [N_S]), electron irradiated diamonds, we now analyze our collected data to see which irradiation and anneal-

ing regime optimizes the diamond for ensemble NV magnetometry.

We will focus only on the main variables of the sensitivity equation $\eta \sim 1/\alpha\sqrt{\beta T}$ and ignore fundamental constants and factors of order unity that arise from the specific magnetometry scheme implemented. Recall that a given NV ensemble emits a photoluminescence (PL) spectrum under excitation with contributions from both the NV^0 and NV^- charge states. In Chapter 3 we modelled these contributions as arising from a linear combination of the individual charge state PL spectra, f_{NV^0} and f_{NV^-} , where f is defined as the total integrated intensity of the individual PL spectra. In this chapter we take these values to be fluorescence rates in photons/second. The total fluorescence f_{NV} is then taken to be a linear combination of the two rates: $f_{NV} = c_0 f_{NV^0} + c_- f_{NV^-}$, where c_0 and c_- are the fitting coefficients from the linear combination. In Chapter 1 the contrast α was defined in terms of two measured signals in a standard NV measurement, m_0 and m_1 . The normalized difference between these two signals provides a measure of the population difference of the NV center being addressed. For a single NV^- center, when the ground state spin is in $|\pm 1\rangle$, the maximum population difference is 30 % [7]. Assuming this occurs under the conditions where signal m_1 is taken, we write the fluorescence as $m_0 = f_{NV_{single}^-}$, $m_1 = (1 - 0.3)f_{NV_{single}^-}$ ¹.

In an ensemble measurement, however, the presence of NV^0 serves to decrease the contrast by adding background fluorescence. Furthermore, as explained in Appendix C, typically in NV ensemble magnetometry only one NV orientation in the crystal lattice is addressed by microwave (MW) control pulses, while the other three classes provide additional background fluorescence. For laser polarization normally incident on a diamond with (100) face geometry, only two NV classes can be preferentially excited at a time, while the other two are minimally excited. For this geometry it has been measured that the intensity ratio of maximum to minimum fluorescence is 2:1 [76]. Therefore, out of the total fluorescence of all four NV^- classes, 2/3 arises from the three NV classes (one preferentially excited and two minimally excited) not addressed and 1/3 arises from the NV class (preferentially excited) that is being addressed. When the latter NV^- class is in the $|\pm 1\rangle$ state, the fluorescence from the NV^- ensemble is $m_1 = c_0 f_{NV^0} + c_- \left(\frac{2}{3} f_{NV^-} + (1 - 0.3)\frac{1}{3} f_{NV^-}\right) = c_0 f_{NV^0} + 0.9c_- f_{NV^-}$, where we

¹Note that 30% is the typical maximum contrast that can be achieved; if laser broadening exists the contrast will decrease. In a pulsed experiment, however, this is not an issue as long as the pulses are well calibrated and no contrast is lost to decoherence.

have included the NV^0 fluorescence that is the same for m_1 and m_0 . Putting this all together, the measurement contrast $\alpha = (m_0 - m_1)/(m_0 + m_1)$ is

$$\alpha = \frac{0.1c_-f_{NV^-}}{2c_0f_{NV^0} + 1.9c_-f_{NV^-}}. \quad (5.1)$$

The photons collected β is modeled as $\frac{m_0+m_1}{2}t_{gate}$, where t_{gate} is the fluorescence collection time. In terms of the fluorescence rates calculate above, this yields

$$\beta = (c_0f_{NV^0} + 0.95f_{NV^-})t_{gate}. \quad (5.2)$$

The measurement time T is the length of the free-precession time in the measurement, which we take here to be T_2 , and the dead-time of a measurement used to re-pump the NV ensemble to the $|0\rangle$ state. The sensitivity formula $\eta \sim 1/\alpha\sqrt{\beta T}$ assumes that $T_2 \gg t_{pump}$; if the coherence time and pump time are comparable then the sensitivity needs to be modified to $\eta \sim \sqrt{T_2 + t_{pump}}/\alpha\sqrt{\beta T_2}$. To assist in comparing relative sensitivities between the diamonds, we use the inverse sensitivity as our figure of merit:

$$FOM = \frac{\alpha\sqrt{\beta T_2}}{\sqrt{T_2 + t_{pump}}}. \quad (5.3)$$

In terms of the figure of merit, a high sensitivity (low value of η) corresponds to a high FOM. Thus, we now seek to determine which processing conditions gives the highest values of FOM .

To calculate FOM for each diamond, we use the values of the fitting coefficients c_0, c_1 and the measured spin-decoherence time T_2 for each diamond for all laser powers used. One more thing is needed, however. In practice, due to the PL spectra overlap of NV^- with NV^0 , a long-pass optical filter is used in measuring m_0 and m_1 to improve the contrast α . While this does prevent some NV^- fluorescence from being measured, the much larger decrease in NV^0 fluorescence compensates for this. The cut-off wavelength λ_0 of this filter, however, depends on the relative contributions of each charge state. The individual charge state total fluorescence f_{NV^0} and f_{NV^-} are normalized to have an area of unity. In calculating the FOM , we varied the cut-off wavelength λ_0 for all wavelength measured (1340 with our

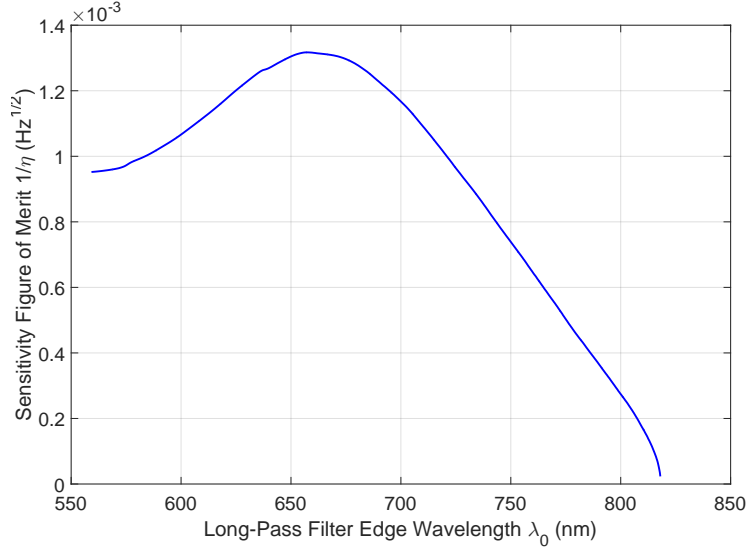


Figure 5-1: Sensitivity figure of merit FOM as a function of long-pass filter wavelength λ_0 for Rutherford ($1 \times 10^{16} \text{ e}^-/\text{cm}^2$, 1250°C anneal) at 70 mW of excitation.

CCD), which varied the value of the total fluorescence $f_{NV^0,-}$ from 0 to 1. Figure 5-1 shows an example of the variation of FOM as a function of the cut-off filter. As expected, an optimum value is reached as the reduction in NV^0 increases the contrast α . At higher cut-off wavelengths, the reduction in the collected photons β from both charge states counteracts the increase in contrast and reduces the FOM . Out of the 1340 values of FOM calculated, one for each long-pass filter, we report only the maximum values in the rest of this chapter.

5.2.2 Sensitivity vs. Irradiation Dose

Figure 5-3 plots the sensitivity FOM for each diamond at four excitation powers for both annealing temperatures. At low irradiation doses the sensitivity FOM increases until about ($\sim 1 \times 10^{18} \text{ e}^-/\text{cm}^2$). This agrees with the increasing NV fluorescence seen at these doses. The drop in FOM past this dose agrees with the drop in fluorescence seen in Figure 3-2 and the drop in T_2 seen in Figure 4-4. With regards to the optical power, the FOM monotonically increases (ignoring the systematic error for Bascom at ($5 \times 10^{17} \text{ e}^-/\text{cm}^2$, 850°C anneal)) due to the increased fluorescence higher excitation brings. The relative change in sensitivity, however, decreases as the power increases, which agrees with the start of saturation seen in Figure 3-6 and Figure 3-7, as well with the decrease in contrast due to a lower charge state

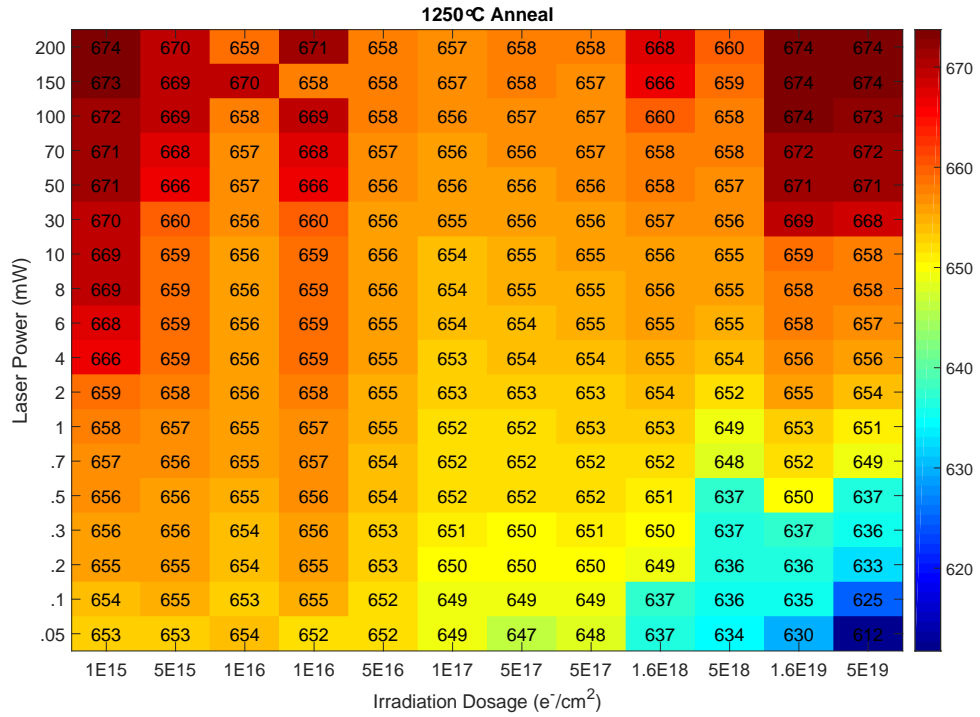
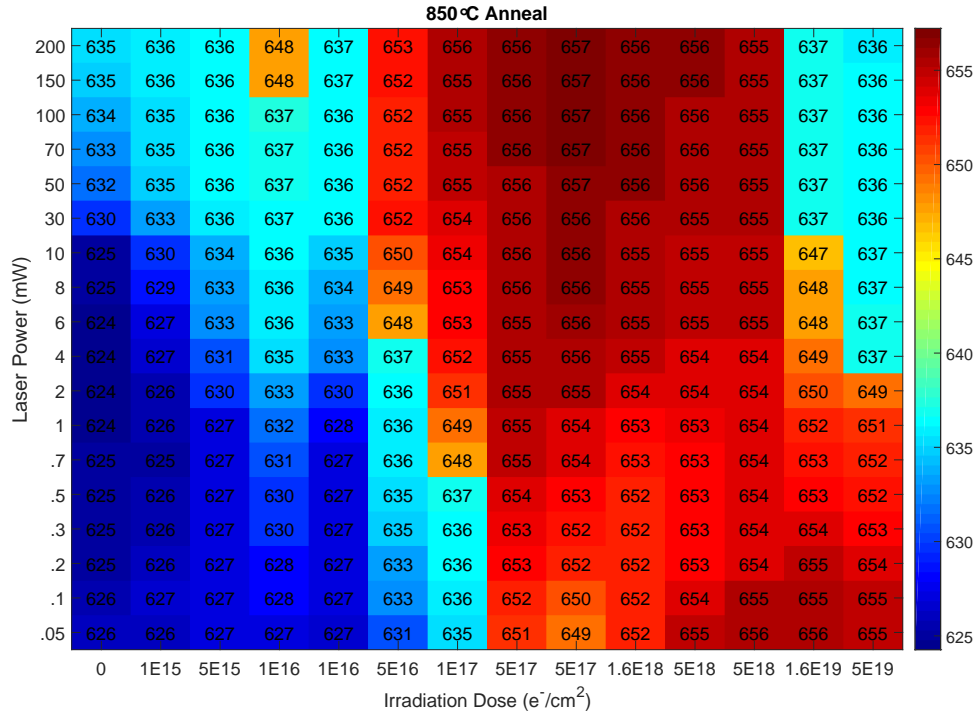


Figure 5-2: Optimum long-pass filter wavelength λ_0 as a function of laser power and irradiation dose for diamonds annealed at (top) 850°C and (bottom) 1250°C.

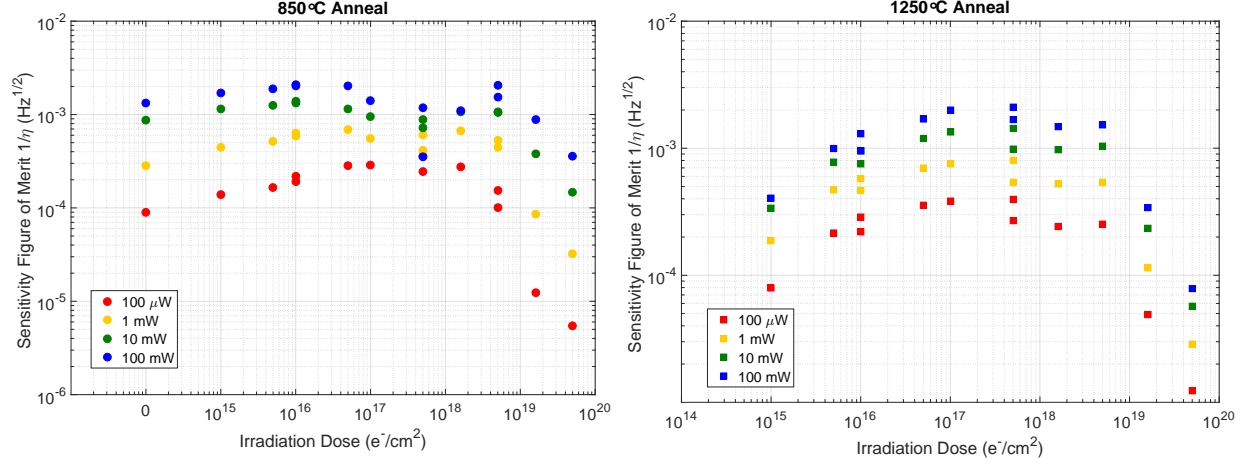


Figure 5-3: Relative sensitivity vs. irradiation dose over four orders of magnitude of excitation power for diamonds that underwent (a) 850°C annealing treatment (b) 1250°C annealing treatment.

fluorescence ratio, as was seen in Figure 3-9 (ignoring the highest two doses).

With regards to annealing temperature, Figure 5-4 shows the sensitivity *FOM* for both anneal temperatures at a low (100 μ W) and high (150 mW) laser excitation. At low laser power, the 1250° annealed diamonds achieve the optimum *FOM* in the dose range ($1 \times 10^{16} \text{ e}^-/\text{cm}^2 \lesssim D \lesssim 1 \times 10^{18} \text{ e}^-/\text{cm}^2$), which is consistent with the total fluorescence plotted in Figure 3-3 where in this dose range 1250°C diamonds have a higher total fluorescence than 850°C annealed diamonds. At higher laser powers, diamonds annealed at 850°C show higher *FOM*, in agreement with the lower charge state fluorescence ratio for 1250°C annealed diamonds seen in Figure 3-10.

5.3 Outlook

The data presented in the previous section reveal that for the majority of laser powers used, diamonds annealed at 1250°C and irradiated with a dose around $5 \times 10^{17} \text{ e}^-/\text{cm}^2$ would give an NV ensemble magnetometer the highest sensitivity. At all laser powers, the dose range ($5 \times 10^{16} \text{ e}^-/\text{cm}^2 \lesssim D \lesssim 5 \times 10^{18} \text{ e}^-/\text{cm}^2$) yields the optimum sensitivity compared to other doses at 1250°C. At higher laser powers, diamonds annealed at 850°C with a dose around $1 \times 10^{16} \text{ e}^-/\text{cm}^2$ optimize the sensitivity. The highest sensitivity *FOM* obtained

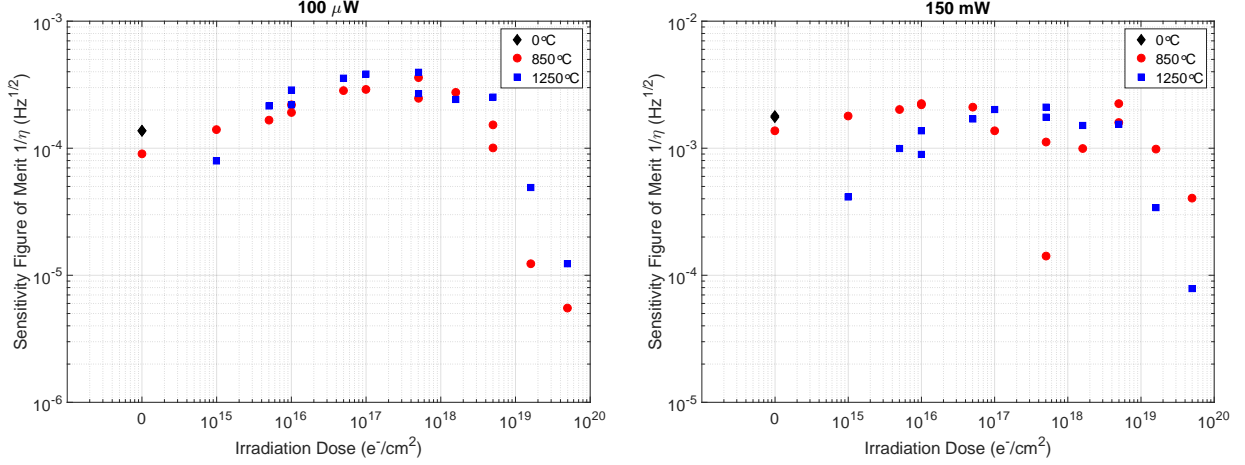


Figure 5-4: Relative sensitivity vs. irradiation dose at all anneal temperatures for (left) 100 μW and (right) 150 mW of laser excitation.

is at 200 mW for 850°C annealing temperature and a irradiation dose of $1 \times 10^{16} \text{ e}^-/\text{cm}^2$. Although $5 \times 10^{18} \text{ e}^-/\text{cm}^2$ gives a slightly higher sensitivity, the increase in the magnitude of the charge state ratio seen in Figure 3-11, as well as the lower value of T_2 relative to the low dose diamonds seen in Figure 4-4, make it suspect to the unknown effect that the highly irradiated diamonds have. At lower powers this dose not yield highest FOM . The dose range ($1 \times 10^{16} \text{ e}^-/\text{cm}^2 \lesssim D \lesssim 1 \times 10^{17} \text{ e}^-/\text{cm}^2$), however, consistently gives the optimum sensitivity FOM regardless of laser power.

This answers the question this thesis originally set out to answer. However, as seen in the data, at high doses ($\gtrsim 1 \times 10^{19} \text{ e}^-/\text{cm}^2$) unobserved deviations are seen from expected behavior in terms of a simple model of monovacancies and substitutional nitrogen atoms in the diamond lattice. At these higher doses the radiation damage to the lattice creates additional defects that are speculated to degrade the spin decoherence time T_2 of the diamond and significantly affect the charge-state dynamics of the NV center, shown by the increase in charge state fluorescence ratio under increased excitation power. If the results of this study are to be generalized to a wider range of diamonds, to include differing nitrogen concentrations, it is important that the behavior seen at high dose is fully understood.

The behavior of the charge state properties and coherence times under high dosages is most likely due to the presence of increased vacancy-related defects [38, 55], such as vacancy chains. Since a majority of these defects are paramagnetic, they can be identified by electron

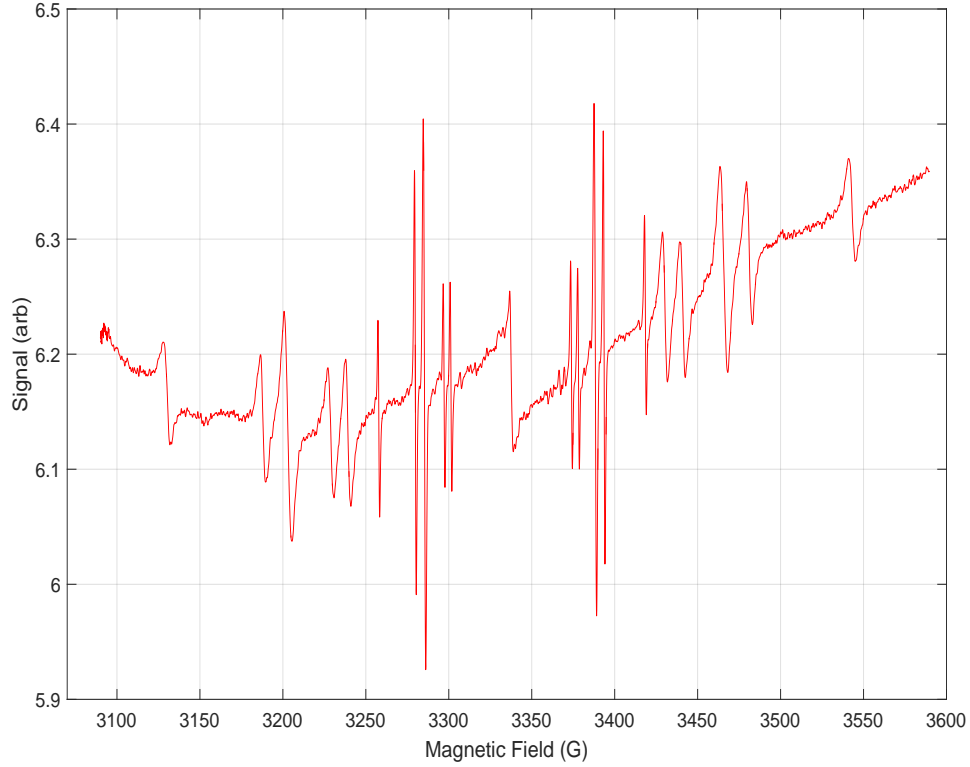


Figure 5-5: Example EPR spectrum for Ladd-Franklin ($5 \times 10^{18} \text{ e}^-/\text{cm}^2$, 850°C anneal). While the signal ideally should have a flat baseline, the MW power causes a response from holding tube that needs to be subtracted.

paramagnetic resonance spectroscopy. Briefly, under a fixed microwave frequency (around 10 GHz for typical X-band EPR) an applied static magnetic field is swept through a range of amplitudes, altering the Zeeman energy splittings of unpaired spins in paramagnetic defects. When the magnitude of the field causes the splitting to match the applied MW frequency, a transition between spin states occurs and the absorption of the MW is recorded. To enhance the signal-to-noise, phase sensitive detection is used where the magnetic field is modulated as it is swept. This results in the measurement of the first derivative of the actual MW absorption signal. Figure 5-5 shows an example raw EPR spectra for a diamond irradiated with a dose of $5 \times 10^{18} \text{ e}^-/\text{cm}^2$. The uneven baseline is the EPR signal from the Roxolite tube used to hold the diamond in the MW cavity. Comparison with Figure 2 in [38] indicates that some of the defects created at this high dose are vacancy chains. A systematic study of EPR spectra for the diamonds in this thesis could identify paramagnetic defects created

at high electron irradiation doses, which could assist in understanding the behavior of the charge state fluorescence and coherence times at these high doses.

Appendix A

Experimental Setup and Calculations

This appendix describes the experimental setup used for this thesis and provides technical details relevant to the acquisition/analysis procedures discussed in earlier chapters. In addition, the laser intensity for a given measured laser power, the approximate region of the confocal spot that is imaged by the collection fiber, and the approximate laser power needed to reach NV^- saturation is calculated.

A.1 Experimental Setup

A.1.1 Overview of the Setup

A home-built fluorescence microscope served as the basis for both photoluminescence (PL) spectroscopy and coherence time measurements of the diamond samples. The apparatus is shown in Figure A-1.

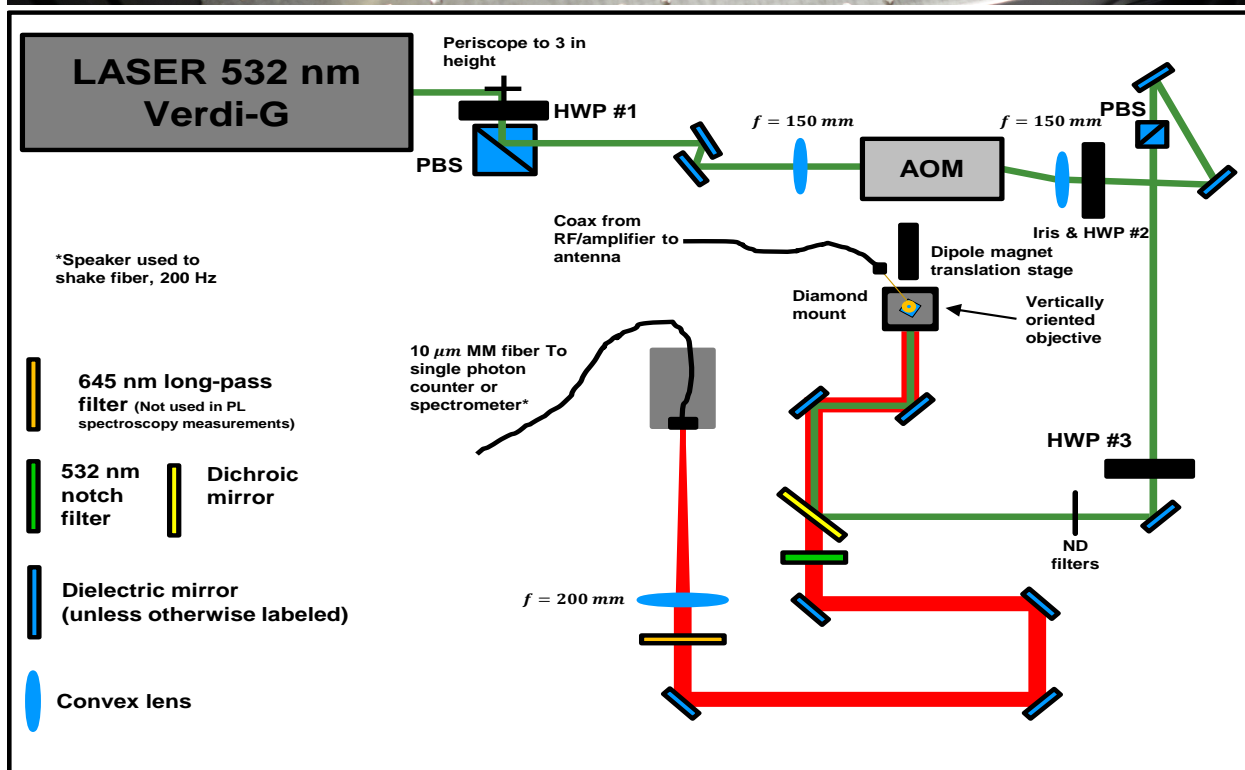
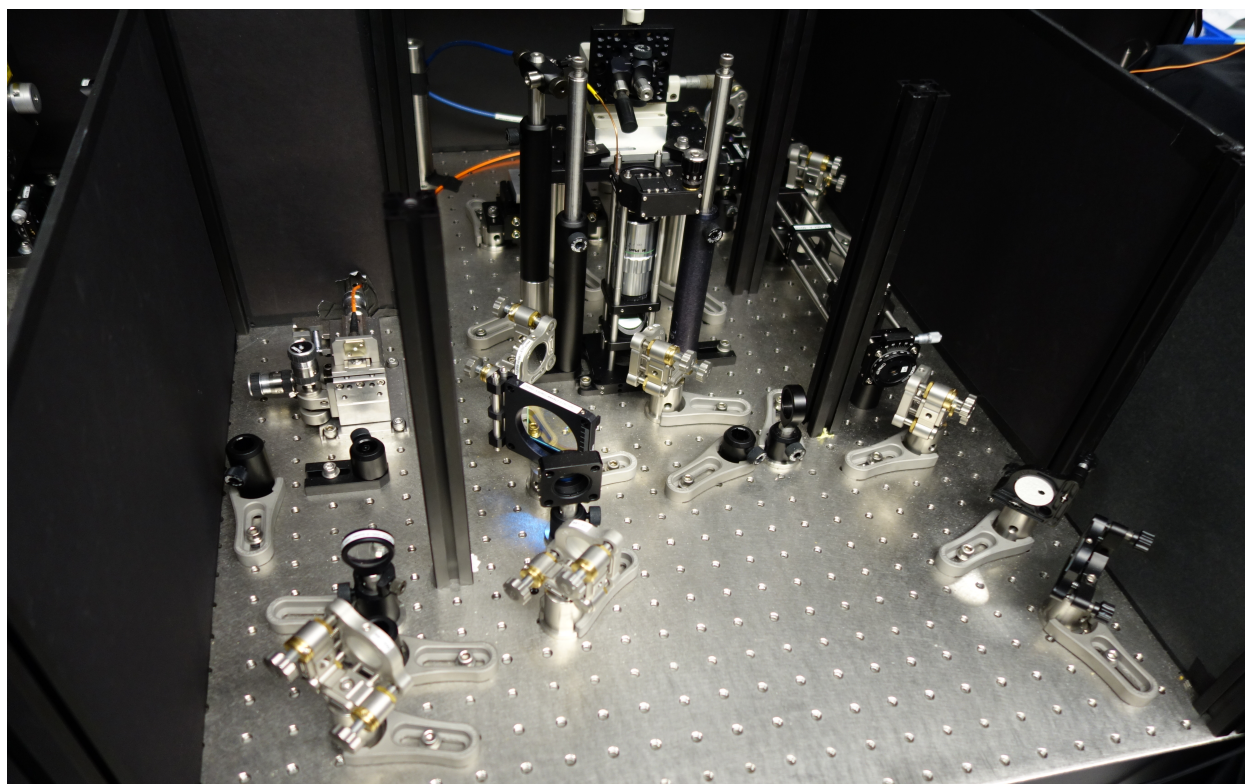


Figure A-1: Diamond characterization experimental setup (top) photograph and (bottom) schematic.

The two main sections of this setup are the optical excitation path and the NV fluorescence collection path. The optical excitation path begins with a 5 W 532 nm laser (Coherent Verdi G5). To maximize the proportion of NVs in the negative charge state the optimal excitation wavelength is in the range 510 - 540 nm [19], even though the NV^- zero-phonon line resonance is at 637 nm. To control the intensity of light from the laser box into the setup the green laser light first traverses a half-wave plate (HWP) and a polarizing beam splitter (PBS). Amplitude-controlled light is deflected by an acousto-optic modulator (AOM; Crystal Tech/Gooch & Housego 3200-147, driver model 1200-200). The first-order diffracted beam passes through a second HWP and PBS, which is used to control the power into a microscope objective. The beam then passes through a third HWP that establishes reference polarization axes of the light into the objective. The beam reflects off a dichroic mirror (Semrock LPD02-532RU, edge wavelength 537.2 nm) to a microscope objective (Mitutoyo, 20x, $\text{NA} = 0.42$, infinity-corrected) and is focused to a spot size $3.01\ \mu\text{m}$ in diameter (calculated below). The diamond is located on a z -translation stage directly over the objective shown in Figure A-2 (left). A loop antenna connected to an amplifier (Mini-Circuits ZHL-16W-43+) and vector signal generator (Keysight N5182B) provides microwaves for coherent control of the NV ensemble. A 1" pedestal spacer serves as the diamond mount; glass coverslip slides glued onto the spacer hold the diamond in a consistent location while under pressure from the loop antenna as shown in Figure A-2 (right). For coherence measurements, the diamond mount is aligned such that the confocal spot is at the top of the diamond near the antenna to provide a uniform MW field, while for PL measurements the mount is adjusted such that the confocal spot is at the bottom of the diamond closest to the objective to avoid laser or NV fluorescence absorption. To provide a static bias magnetic field, a permanent magnet is attached to a translation stage behind the diamond mount.

Light emitted from the NV ensemble in the diamond is collected by the objective and is transmitted through the dichroic mirror to a $0.10\ \mu\text{m}$ core multi-mode fiber (Thorlabs, M64L02). This coupling element is attached to a steel translation stage and serves as a pinhole to isolate the NV fluorescence emitted from the confocal volume of the objective in the diamond. This fiber is connected to one of two other fibers, a spectrometer for photoluminescence measurements or a single photon counter for coherence-time measurements.

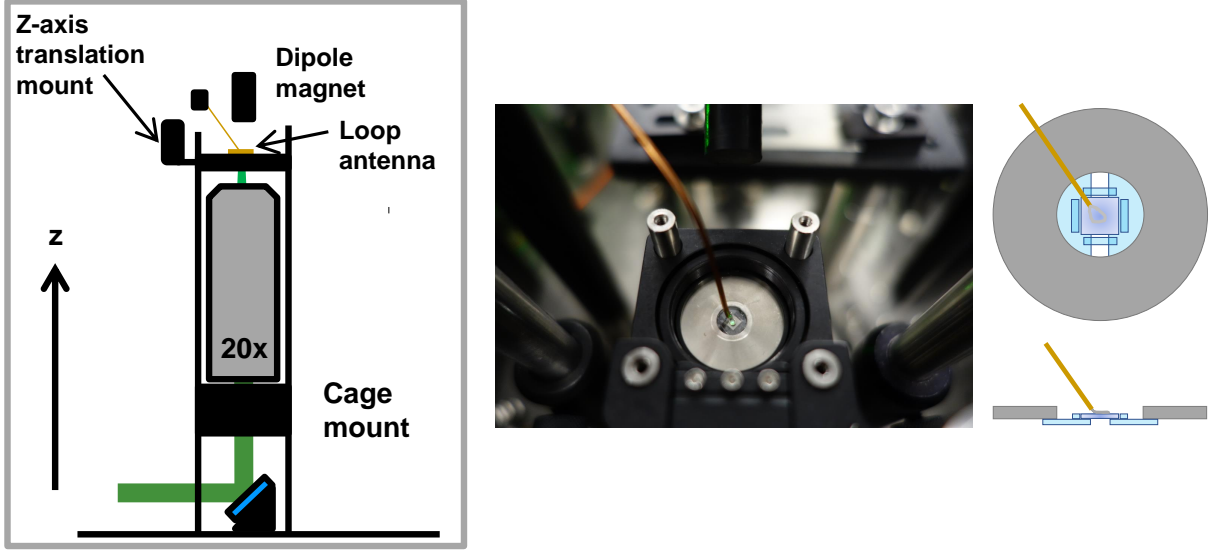


Figure A-2: Diamond mount. (left) Vertical view of the objective-diamond assembly. Laser light reflects up to the objective in a cage mount where it focuses onto the diamond mount translation stage, which is adjustable to ensure that the confocal volume is at the top of the diamond near the MW loop for coherence measurements or near the bottom of the diamond for PL spectroscopy measurements. (right) Left: photograph of the diamond mount. The loop antenna is pressed against the face of the diamond and centered about the confocal spot to maximize MW uniformity. Right: diamond mount schematic with top and side views.

A.2 Fluorescence Calculations

In this section we calculate the relevant experimental parameters for the setup defined above. We will model the intensity of the green laser beam focused by the objective as a Gaussian profile:

$$I(r, z) = \frac{2P}{\pi w(z)^2} \exp\left(-\frac{2r^2}{w(z)^2}\right), \quad (\text{A.1})$$

where P is the laser power, $w(z) = w_0 \sqrt{1 + (z/z_R)^2}$ is the $1/e^2$ beam radius (defined as the distance where the intensity drops to 13.5% of its maximum value), $z_R = \pi n_d w_0^2 / \lambda$ is the Rayleigh range (adjusted for the diamond index of refraction n_d), r is the radial distance in the plane transverse to the beam, and z is the axial distance with the origin defined at the center of the confocal volume [77]. The beam waist diameter at the origin is $2w_0$. The peak intensity I_0 is defined to be $I_0 = \frac{2P}{\pi w_0^2}$.

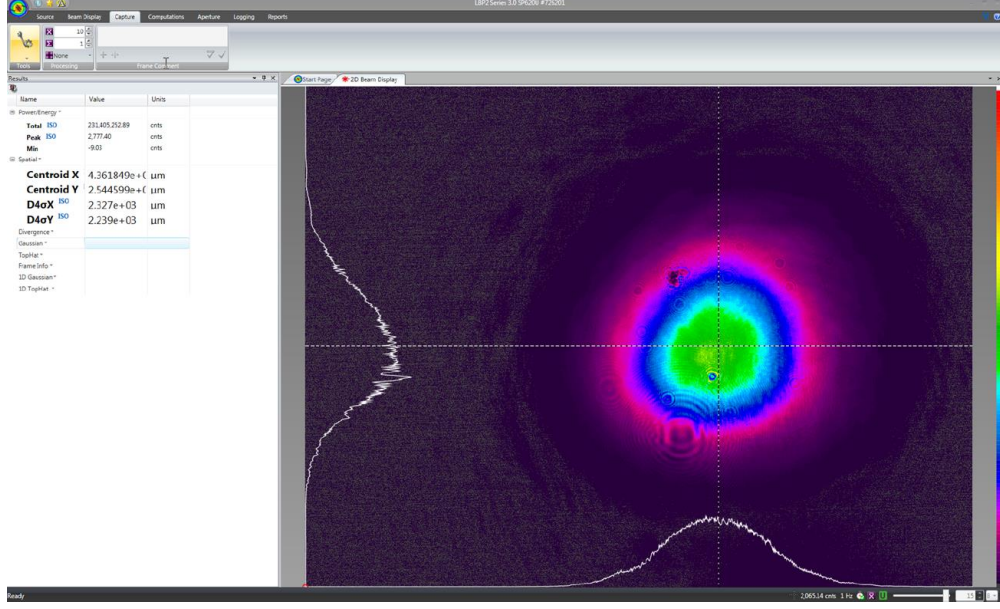


Figure A-3: Profile of the laser beam right before being reflected off the dichroic. The $D4\sigma X$ and $D4\sigma Y$ give measures of the beam widths in the X and Y directions.

A.2.1 Power Density

To calculate the intensity of the light in the confocal volume of the diamond, we first measure the spot size of the green laser beam before the dichroic with a beam profiler (Newport LBP2-HR-VIS). Figure A-3 shows the values of $D4\sigma X$ and $D4\sigma Y$ of the beam, which for a Gaussian beam give the width in terms of the $1/e^2$ distance¹. The Verdi G5 laser manual specifies a Gaussian beam diameter of $2.25 \text{ mm} \pm 10\%$, which is in agreement with the X-width of 2.33 mm and Y width of 2.24 mm. Possible reasons for the different X and Y lengths are the diffraction of the beam from the AOM and imperfect optics.

From the Mitutoyo objective manual, for an incident Gaussian beam of $(1/e^2)$ width D_{laser} , the focused beam waist is $D_{spot} = \frac{4\lambda f_{obj}}{\pi D_{laser}}$. For an input radius of 2.25 mm, laser wavelength $\lambda = 532 \text{ nm}$, and objective focal length $f_{obj} = 10 \text{ mm}$, the beam waist is 3.01 μm . This yields a Rayleigh range $z_R = 32 \text{ μm}$ for a confocal volume of about 450 μm^3 . Incident laser power was measured prior to the dichroic mirror. Accounting for 83% transmission

¹ $D4\sigma X$ is defined as four times the second x -moment M_x of the transverse intensity distribution of the light beam. The second moment in the x direction is $M_x = 2\sqrt{\frac{\int \int x I(x,y,z) dx dy}{\int \int I(x,y,z) dx dy}} = 2\sqrt{\frac{\int \int r^2 \cos^2 \theta I(r,z) r dr d\theta}{\int \int I(r,z) r dr d\theta}} = w(z)/2$. Since w is the $1/e^2$ radius and $D4\sigma X = 4M_x = 2w$, for a Gaussian beam both $D4\sigma X$ and the $1/e^2$ diameter are the same.

of the dichroic and 17% front surface reflection at normal incidence to the diamond², the intensity of the laser at the middle of the confocal spot in the diamond is

$$I = \frac{(0.83)^2 P}{\pi(D_{spot})^2/8} = P \cdot 0.1936 \mu\text{m}^{-2}, \quad (\text{A.2})$$

where the measured laser power prior to the dichroic mirror P is in mW.

A.2.2 Saturation Power

The saturation intensity of the NV^- center is approximately 100 kW/cm² [78]. Thus, for a confocal spot size diameter of 3.01 μm and 69% power loss, this corresponds to a measured laser power of 5 mW before the dichroic in this experiment.

A.2.3 Imaging Region Calculations

In Chapter 3 saturation of the NV fluorescence is considered. To see saturation effects in confocal microscopy, it is important that the region imaged by the pinhole is restricted to the central region of the confocal spot, where saturation is noticeable (i.e. to avoid measuring the increasing fluorescence in the wings of the NV fluorescence profile which do not saturate as fast). The collected fluorescence from the objective used the full numerical aperture. With a back aperture of 8.4 mm, the collection region of fluorescence by the objective is $D_{collection} = \frac{4\lambda f_{obj}}{\pi D_{backaperture}}$, which for a wavelength range of 560 - 818 nm is 0.85 to 1.24 μm .

²For light at normal incidence to a diamond-air interface, the reflection is $\left(\frac{n_d - n_{air}}{n_d + n_{air}}\right)^2 = 0.17$ from the Fresnel equations, where $n_{air} = 1.000$ is the index of refraction for air and $n_d = 2.419$ is the index of refraction for diamond.

Appendix B

NV Fluorescence Methods and Calculations

Chapter 3 showed the results of fluorescence measurements taken on the diamonds as the irradiation dose and optical excitation power were varied. To extract the charge state fluorescence ratio and the total fluorescence from each charge state, the fluorescence fraction of a photoluminescence (PL) spectrum from each charge state must be calculated. This appendix details the charge-state fluorescence data acquisition process and the accompanying analysis to calculate the charge state fluorescence ratio and total fluorescence from a linear combination of NV^0 and NV^- PL spectra.

B.1 Charge State Data Acquisition

B.1.1 Measurement Procedure

All PL spectroscopy measurements are performed with a spectrometer (Princeton Instruments, IsoPlane SCT 320) and an attached CCD camera (Princeton Instruments, PIXIS 100), shown in Figure B-1a. As explained in Appendix C, the half-wave plate before the dichroic in the experimental setup is adjusted so that the 532 nm excitation equally excites all four NV orientation classes. Princeton Instruments Intelical USB-powered sources provide wavelength and intensity calibrations to the recorded spectra. The intensity calibra-

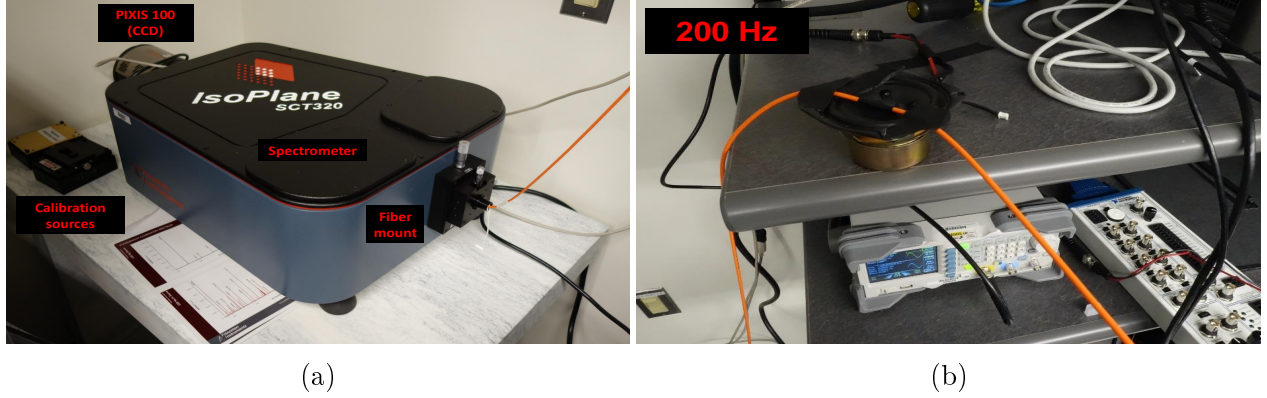


Figure B-1: Experimental apparatus for PL spectroscopy (a) Spectrometer. A fiber is mounted to the entrance slit where the acquired NV fluorescence is diffracted and processed by the CCD camera. The position of the fiber can be adjusted in two dimensions. A micrometer allows fine adjustment of the spectrometer input slit. (b) Fiber shaker to eliminate modal noise in the acquired PL spectra.

tion removes instrumental artifacts in the PL spectra that arise from the differing spectral responses from various optical elements in the spectrometer (mirrors, diffraction grating, CCD camera, etc.). Figure B-2 (top) shows a sample PL spectrum with and without this calibration. Only the rows of the CCD illuminated by the fiber are used in calibrating the spectra. To obtain maximal signal-to-noise, the exposure time of each frame is set so that the peak intensity on the CCD is about 55,000 counts; this ensures that the CCD operates in the linear regime but that the pixel wells are still nearly full. The diffraction grating is set to 300 gratings/mm with a center wavelength of 690 nm, which records spectra in the range of 560 - 818 nm. Finally, to avoid signal to noise degradation by modal noise in the multi-mode fiber [79], the fiber is taped to a speaker-head driven by a 200 Hz sinusoidal voltage (15 Volts peak-to-peak). Figure B-2 (bottom) shows a sample PL spectrum with and without the fiber shaker, revealing the enhancement in spectral resolution of the NV⁻ zero-phonon line amidst the NV⁰ phonon sideband.

After data acquisition, the resulting files are exported to .csv files to be read by MATLAB code. All frames taken for a single measurement are averaged together, followed by normalization by the exposure time of the measurement. To analyze the charge state properties of the PL spectra for each diamond, we employ a linear combination of NV⁰ and NV⁻ spectra [65] as described in the next section.

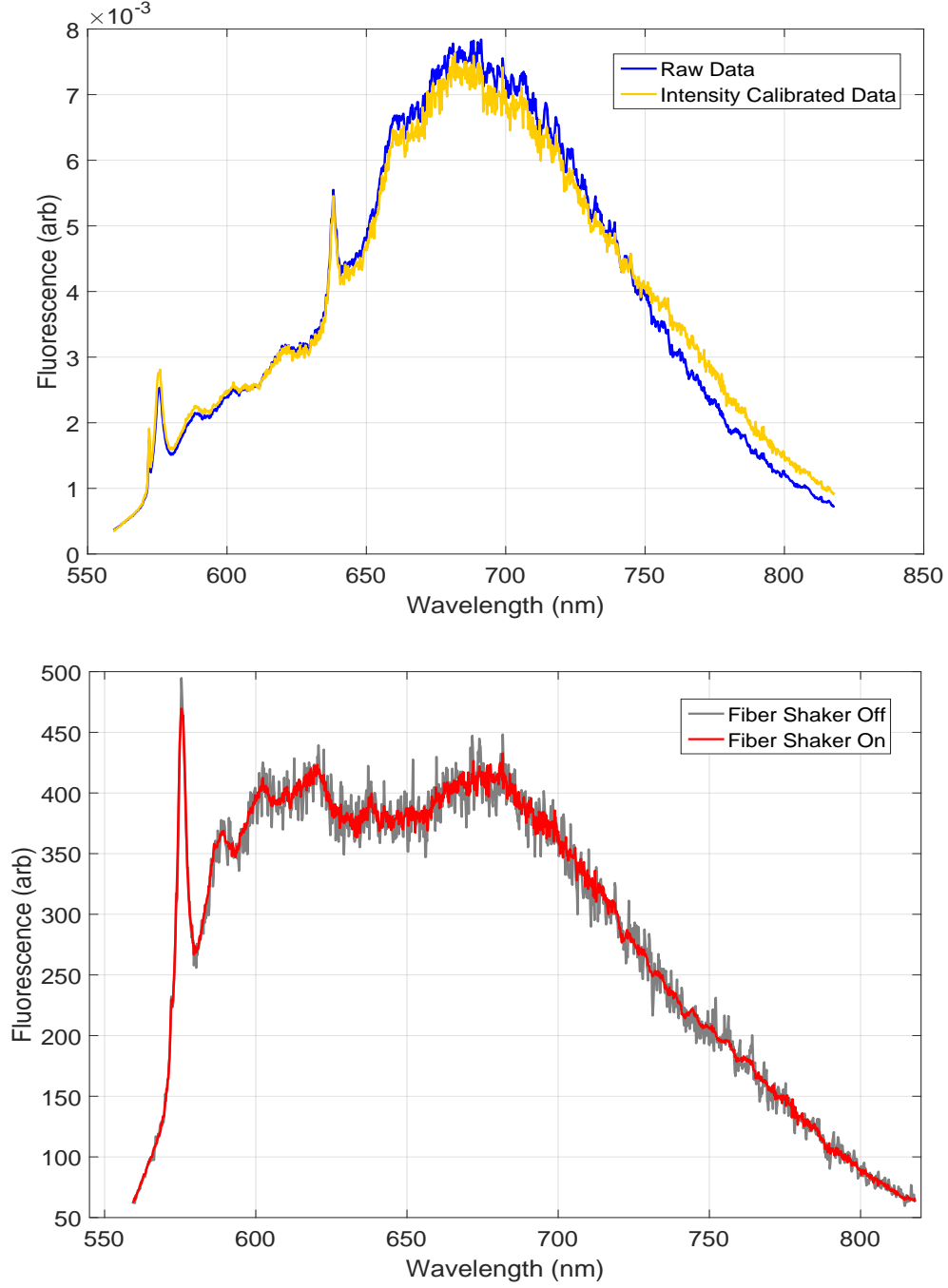


Figure B-2: Spectrum modification to correct for experimental artifacts. (top) Normalized photoluminescence spectra of the diamond Hilbert ($5 \times 10^{15} \text{ e}^-/\text{cm}^2$, 1250°C anneal) at 1 mW optical excitation with and without the intensity calibration turned on. (bottom) Photoluminescence spectra of the diamond Anderson ($1.6 \times 10^{19} \text{ e}^-/\text{cm}^2$, 1250°C anneal) at $300 \mu\text{W}$ optical excitation with the fiber shaker turned off and on. Notice how the NV⁻ zero-phonon line is resolvable with the fiber shaker on.

B.1.2 Linear Combination of NV Spectra

The other method employed to analyze the charge state ratio was fitting each acquired PL spectra to a linear combination of NV^- and NV^0 ‘basis’ spectrum. That is, for a normalized NV^- basis function $I_-(\lambda)$ and normalized NV^0 basis function $I_0(\lambda)$, each acquired PL spectrum I is fit to a linear combination of the basis functions

$$I(\lambda) = c_- I_-(\lambda) + c_0 I_0(\lambda), \quad (\text{B.1})$$

where c_- and c_0 are the weights of each basis function whose ratio yields the desired charge state ratio.

Constructing the Basis Functions

To acquire the NV^0 basis function, we first measured the PL spectrum of Bascom ($5 \times 10^{17} \text{ e}^-/\text{cm}^2$, 850°C anneal) at 200 mW excitation power (the highest power we can obtain before exceeding the damage threshold of the AOM in our setup). This PL spectrum, while not completely devoid of a NV^- PL fingerprint, is the highest fluorescing diamond in our diamond set and has little if any trace of a NV^- ZPL, so to a good approximation can serve as our NV^0 basis function. To obtain the NV^- basis function, we measured the PL spectrum of Heaviside (unprocessed) at 100 μW . The low power ensures that this specific PL spectrum is predominantly composed of NV^- fluorescence. However, since this spectrum does have a NV^0 PL signature, we scale the NV^0 basis function and subtract it off Heaviside’s spectrum to give the NV^- basis function, shown in Figure B-3. Both basis functions are then divided by their integrated area.

To check the validity of using the Bascom PL spectrum as the NV^0 basis function, we temporarily mounted a 405 nm laser pointer and aligned it to excite the Bascom diamond through the objective; the measured spectrum is plotted with the Bascom spectrum used for the NV^0 basis function (excited at the usual 532 nm) in Figure B-4. At wavelengths below 490 nm the NV^- center can be directly ionized to NV^0 with a single photon (as opposed to the two-photon process outlined in Chapter 1, which results in a lower steady state probability to be in the negative NV charge state [19, 27]. To within a small error the

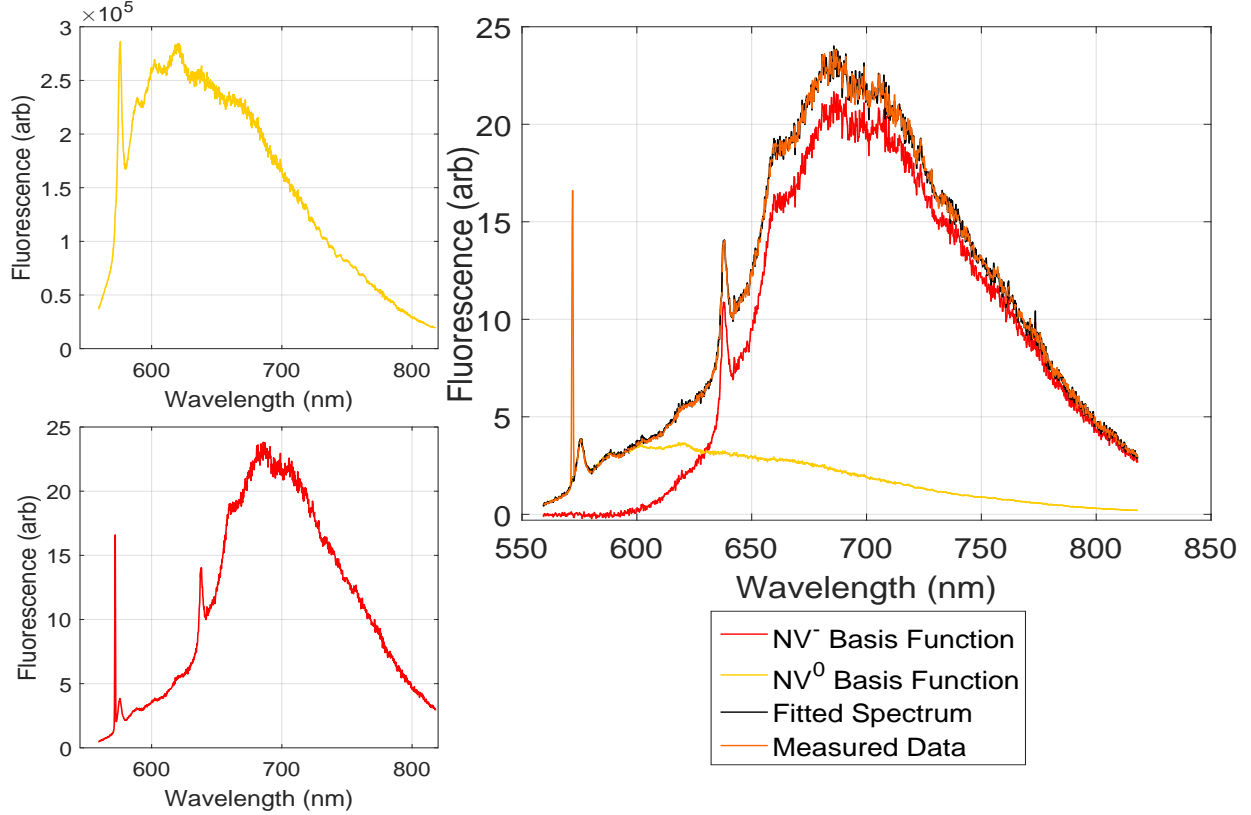


Figure B-3: (Left) PL spectra for Bascom ($5 \times 10^{17} \text{ e}^-/\text{cm}^2$, 850°C anneal) at 200 mW (top) and Heaviside (unprocessed) at $100 \mu\text{W}$ (bottom). Bascom serves as the NV^0 basis function due to its high fluorescence and negligible NV^- content. (Right) Construction of the NV^- basis function. The NV^0 basis function is scaled to fit the NV^0 ZPL of Heaviside's PL spectrum, which is then subtracted to yield the NV^- basis function. The original and basis-fitted Heaviside spectra are also shown.

two functions have a similar spectral profile.

Calculating the Coefficients

To obtain the coefficients c_- and c_0 , we use the method of least-squares regression [80]. To fit the measured PL spectrum $I(\lambda)$ to the form $I(\lambda) = c_- I_-(\lambda) + c_0 I_0(\lambda)$ we minimize the sum of the squares of the residuals $\sum_i (I(\lambda_i) - c_- I_-(\lambda_i) - c_0 I_0(\lambda_i))^2$, where λ_i are the discrete wavelengths the spectrum is measured at. This yields the following relations for the

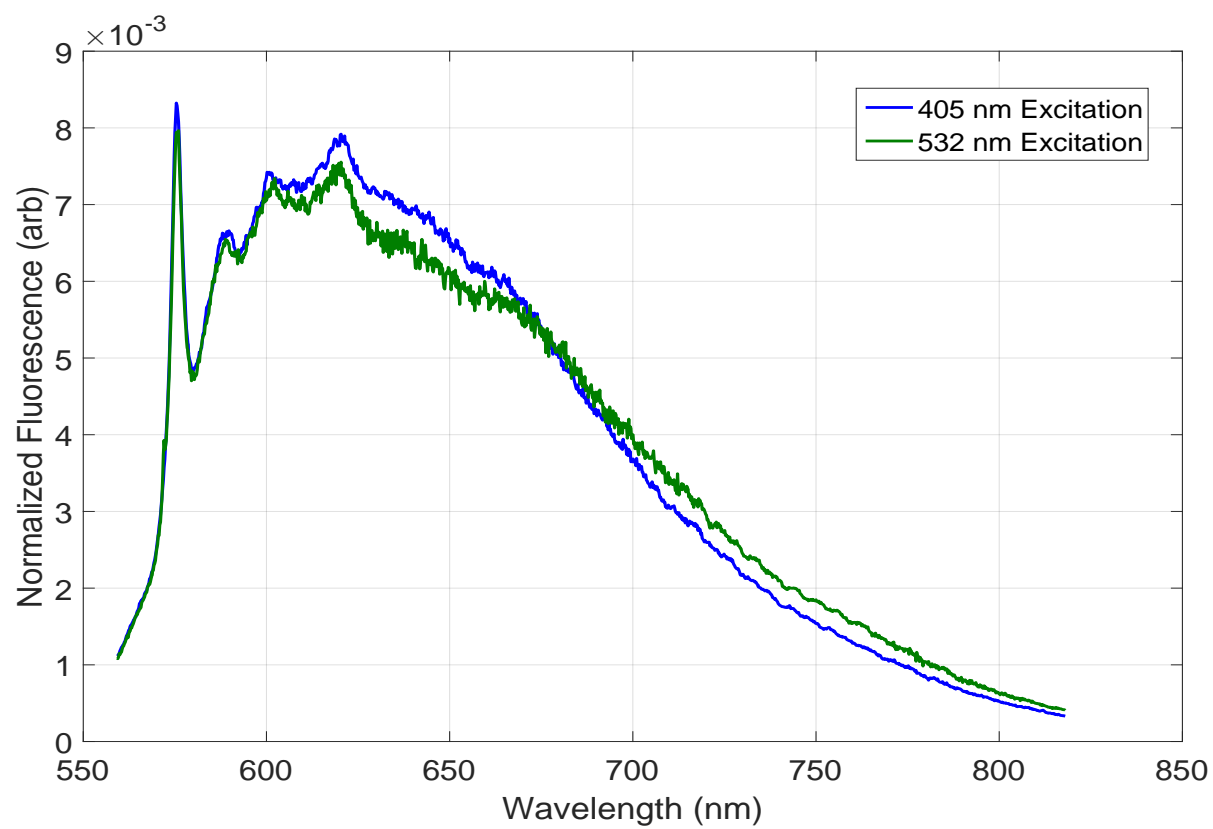


Figure B-4: PL spectra for Bascom ($5 \times 10^{17} \text{ e}^-/\text{cm}^2$, 850°C anneal) at 200 mW for 405 nm and 532 nm excitation.

coefficients:

$$c_- = \frac{\sum_i II_- \sum_i (I_0)^2 - \sum_i I_- I_0 \sum_i II_0}{\sum_i (I_-)^2 \sum_i (I_0)^2 - (\sum_i I_- I_0)^2}, \quad (\text{B.2})$$

$$c_0 = \frac{\sum_i II_0 \sum_i (I_-)^2 - \sum_i I_- I_0 \sum_i II_-}{\sum_i (I_-)^2 \sum_i (I_0)^2 - (\sum_i I_- I_0)^2}, \quad (\text{B.3})$$

where for clarity the functional dependence on λ_i is suppressed. The error of this fit, which is used to determine the error of the charge state fluorescence ratio and total fluorescence, is obtained from the following equations:

$$\sigma_I = \sqrt{\frac{1}{N-2} \sum_i (I - c_- I_- - c_0 I_0)^2}, \quad (\text{B.4})$$

$$\sigma_- = \sigma_I \sqrt{\frac{\sum_i (I_0)^2}{\sum_i (I_-)^2 \sum_i (I_0)^2 - (\sum_i I_- I_0)^2}}, \quad (\text{B.5})$$

$$\sigma_0 = \sigma_I \sqrt{\frac{\sum_i (I_-)^2}{\sum_i (I_-)^2 \sum_i (I_0)^2 - (\sum_i I_- I_0)^2}}, \quad (\text{B.6})$$

where N is number of wavelengths sampled ($N = 1340$ for this CCD).

Ratio and Fluorescence Calculations

To calculate the charge state fluorescence ratio R , we take the ratio of the calculated coefficients from the previous section:

$$R = \frac{c_-}{c_0}, \quad (\text{B.7})$$

where the error is given by standard error analysis:

$$\delta_R = R \sqrt{\left(\frac{\sigma_-}{c_-}\right)^2 + \left(\frac{\sigma_0}{c_0}\right)^2}. \quad (\text{B.8})$$

The fluorescence of each charge state is simply the coefficient for each basis function because the basis functions have an area of unity: $f_- = c_-$, $f_0 = c_0$, $\delta_- = \sigma_-$, $\delta_0 = \sigma_0$. The total fluorescence is then given by the sum of the coefficients:

$$f_{NV} = f_0 + f_-, \quad (\text{B.9})$$

where the error is the sum of the coefficient errors

$$\delta_f = \delta_- + \delta_0. \tag{B.10}$$

Appendix C

Coherence Time Measurement Procedure

Chapter 4 presented the results of coherence time measurements for T_2^* , T_2 , and T_1 . Before each of these measurements are taken, however, certain experimental procedures are executed to ensure the measured coherence times are limited by the concentration of nitrogen and other impurities in the diamond lattice and not by experimentally controllable sources of decoherence. These include anisotropic-hyperfine coupling to the ^{13}C nucleus by the NV center due to a misaligned static field and poorly calibrated proper pulse lengths and frequencies. In this appendix we explain the experimental methods used before coherence time characterization. Specifically, the methodology and experimental acquisition of continuous-wave magnetically detected optical resonance (CAW-ODMR), Rabi nutation, and re-pump optimization measurements will be explained.

C.1 Electronics

For coherence time measurements, the NV fluorescence collected by a 10- μm multimode fiber is sent to an avalanche photodiode single-photon counter (Excelitas SPCM-AQRH-FC). The registered counts are recorded by a DAQ (National Instruments, BNC-2120), which is in turn gated by a pulse generator (SpinCore Pulse Blaster ESR-PRO-500). The Pulse Blaster controls the timing of the optical excitation (by means of switching the AOM on/off), the

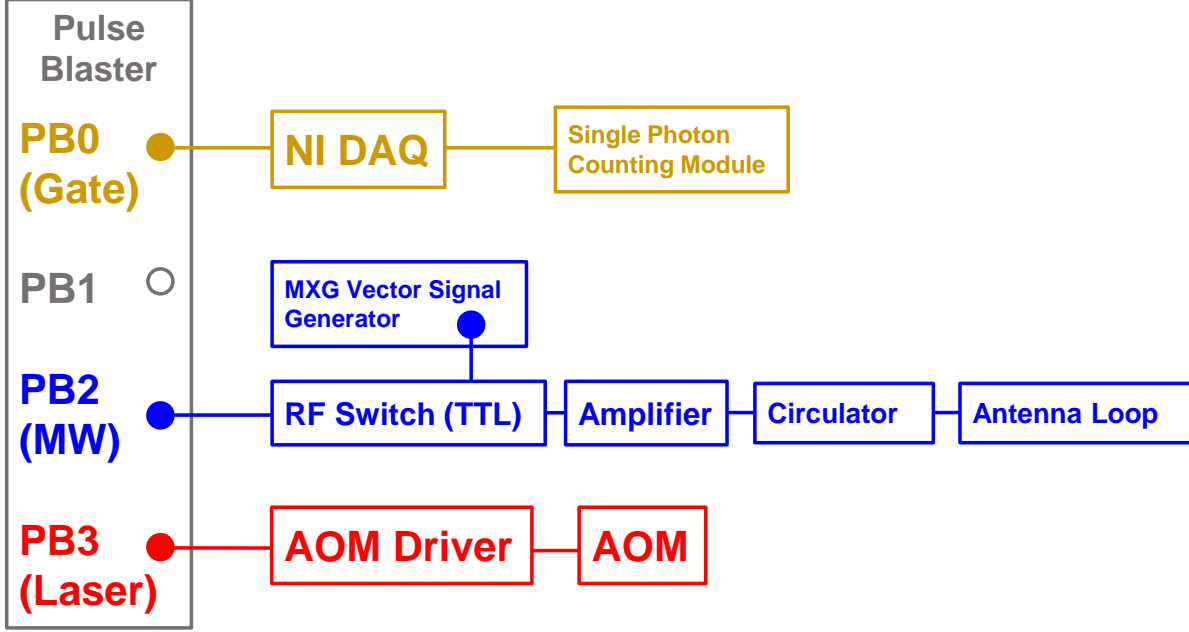


Figure C-1: Wiring diagram for coherent control of the NV center. PB0 controls collection of photons; PB2 controls the MW field delivered to the diamond; and PB3 switches the laser to excite and polarize the NV center.

MW excitation through the loop antenna, and the measurement of the photon counts via the DAQ. Figure C-1 shows the wiring of the SPCM, AOM, and MW drive; the “PB” labels correspond to different channels of the Pulse Blaster card controlling each instrument.

C.2 Static Magnetic Field Alignment

C.2.1 Initial Considerations

The crystal structure of diamond allows the NV center to be aligned along one of four crystallographic axes, giving rise to four ‘classes’, or orientations, of NV centers. In magnetometry schemes, the measurement sequences employed usually focus on only one class of NV centers. To isolate control of this NV class from the other three orientations, a static magnetic field is applied to break the degeneracy of the $|\pm 1\rangle$ spin manifold, where the splitting is proportional to the projection of the field along a given NV’s axis to zeroth order. Due to the natural abundance of ^{13}C in our samples (1.1%), the magnetic field must be aligned to the

desired NV class. If a component of the static field is transverse to this NV axis, anisotropic-hyperfine coupling between the NV electronic spin and proximal ^{13}C nuclei degrades the ensemble coherence time [73]. The degree of this ensemble coherence time degradation is dependent on the strength of the transverse field. Thus, stronger applied bias fields need to be better aligned to the NV axis compared to lower applied bias fields.

The field magnitude along the NV axis is another important consideration. It must not be too low: Ref. [81] illustrates that below 10 G, the contribution to NV decoherence from ^{13}C nuclei increases, thus degrading the value of T_2 for the diamond. Most importantly, though, is the effect it has on the signal we expect from a spin-echo measurement. The Larmor precession of the ^{13}C nuclei cause collapses and revivals in the signal from a spin-echo measurement as discussed in Chapter 4. The period of the Larmor precession (and thus the period of the observed collapses and revivals) is $T_{L,13C} = 1/(\gamma_{13C}B_0)$, where B_0 is the magnitude of the field experienced by the NV ensemble and γ_{13C} is the gyromagnetic ratio of the ^{13}C nucleus (1.071 kHz/G). In a spin-echo measurement, the fluorescent signal experiences a revival when the free precession time $\tau/2$ between the (MW) $\pi/2$ and π pulses is equal to an integer number of the ^{13}C Larmor period. To have enough points for an accurate fit of the signal we chose the field to induce at least 10 revivals in the signal, which means the total pulse sequence measurement time τ must be equal to $T_2/10$. Given typical T_2 for diamonds with $[N] \sim 0.15$ ppm and $^{13}\text{C} \sim 1.1\%$ are around $400 \mu\text{s}$, this corresponds to about 50 G. We have assumed here that the field doesn't vary considerably over the confocal volume so that all ^{13}C nuclei (barring any anisotropic hyperfine coupling due to transverse fields) precess at the same rate.

C.2.2 (100) Diamond Geometry and Initial Field Alignment

To begin field alignment, we place a diamond on the mount such that the magnet is roughly aligned along an NV axis, as shown in Figure C-2. This arrangement is preferred due to the (100) face and sides geometry of the diamond. The MW loop is positioned on top of the diamond with the focused laser spot in the center of the antenna loop. The loop is pressed against the diamond to maximize the MW power delivered to the NV ensemble. The diamond mount is adjusted to focus the confocal spot near the top of the diamond where

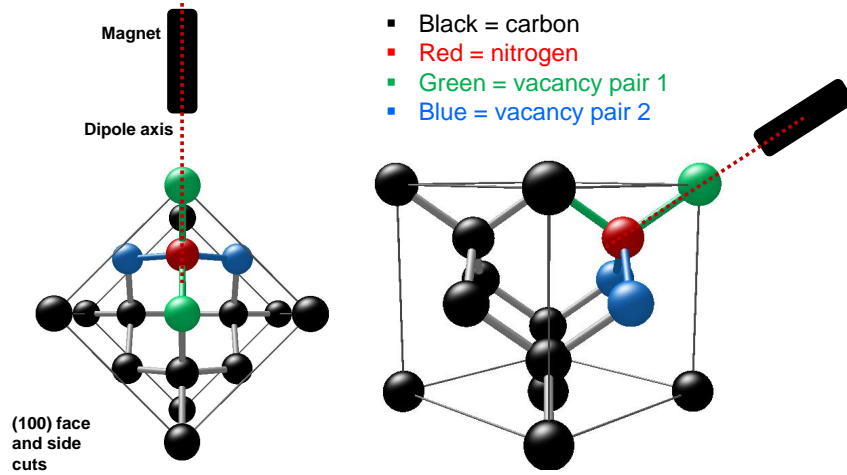


Figure C-2: Diagram of the dipole magnet and (100) diamond geometry. (Left) Top view of the magnet and diamond. The diamond is mounted in the setup such that the corner is bisected by the dipole axis. (Right) Side view of the diamond and magnet. The ideal alignment for this setup and diamond orientation is to have the field axis aligned along the NV class shown.

the MW loops is located (see Figure A-2 (left)). This arrangement is to optically address and detect only the NVs that are near the antenna loop to have strong MW drive field.

C.2.3 CAW-ODMR Measurements

Continuous-wave optically detected magnetic resonance (CAW-ODMR) measurements are performed to extract the resonances of the NV ensemble. As explained in Chapter 1, in CAW-ODMR, while under continuous laser excitation, the frequency of an applied MW field is swept through a range containing the NV ensemble resonances. When the MW field is not on an NV resonance, the fluorescence intensity is a maximum as the NV is polarized in the $|0\rangle$ state. If the MW is on an NV resonance, it drives the NV population which cycles between the $|0\rangle$ and $|\pm 1\rangle$ states. This causes a reduction in the fluorescence intensity due to the increased probability of these states to decay using the non-radiative intersystem crossing. Thus, the recorded fluorescence signal exhibits dips at the NV resonance frequencies. Figure C-3 (top) shows the pulse sequence used to obtain CAW-ODMR data. For the first fluorescence signal m_1 , the laser and MW are applied continuously while the “gate” pulse from the SPCM acquires a fluorescence signal. In the second half of the sequence, the MW is switched off and

the fluorescence m_0 is recorded. This serves as the baseline which the signal m_1 is normalized against, forming the CAW-ODMR contrast m_1/m_0 . In practice, we randomize the order of the frequencies applied to eliminate systematic noise (laser intensity drift, thermal drift, etc.).

If no static magnetic field is applied, the only transition detected is the degenerate $|0\rangle \leftrightarrow |\pm 1\rangle$ electronic resonance at the $D = 2.87$ GHz zero-field splitting. If a static field is applied with a projection B_{\parallel} along the NV axis, then to zeroth order the $|\pm 1\rangle$ states are split by $2\gamma_{NV}B_{\parallel}$, where γ_{NV} is the NV gyromagnetic ratio (2.8 MHz/G). CAW-ODMR then records resonances at $E = D \pm \gamma_e B_{\parallel}$. Furthermore, if the applied MW power is low (i.e. in the absence of power broadening), the hyperfine interaction with the ^{14}N nucleus of the NV center can be observed. The lineshape of the resonance in the measured fluorescence data depends on the intrinsic environment of the diamond and the applied excitation. A single spin coupled to a ^{13}C nuclear spin bath (valid for our low-nitrogen diamonds) gives a Gaussian lineshape, but power broadening from the MW and laser yield a Lorentzian lineshape [30]. The intrinsic linewidth $\Delta\nu$ of the Lorentzian curve is related to the inhomogeneous spin-dephasing time T_2^* by $\Delta\nu = 1/(\pi T_2^*)$.

For an NV ensemble in diamond, all four NV orientations are equally probable, giving rise to as many as eight electronic resonances in a CAW-ODMR spectrum. However, if the field is perfectly aligned to an NV class, the projection of the field along the other three classes will be the same, leading to a three-fold degeneracy. Figure C-3 (bottom) shows a measured CAW-ODMR spectrum where the field is aligned to a single NV class. In this case, the aligned NV resonances are the outermost left ($|-1\rangle \leftrightarrow |0\rangle$) and right ($|1\rangle \leftrightarrow |0\rangle$) transitions due to the maximal field projection along the NV axis, while the threefold degenerate resonances from the other three classes are less split due to a smaller field projection.

C.2.4 Laser Polarization-Assisted Field Alignment

To assist in alignment, we take advantage of the (100) face geometry of the CVD diamond and the linear polarization of the exciting 532 nm laser beam. The NV^- ground state is preferentially excited when the laser polarization is perpendicular to its symmetry axis [13].

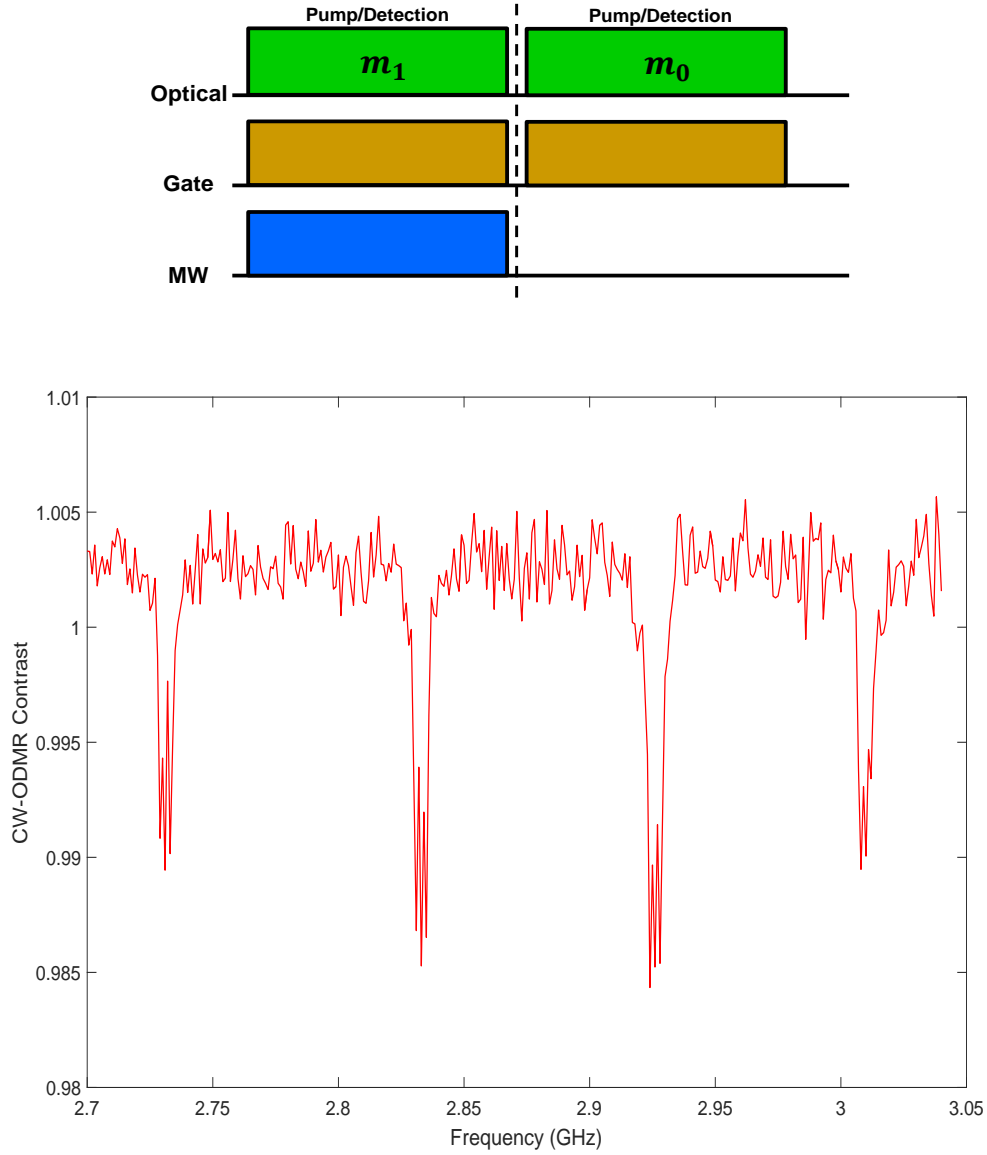


Figure C-3: Continuous-Wave Optically Detected Magnetic Resonance. (top) Pulse sequence to obtain CAW-ODMR data. (bottom) Measured CAW-ODMR spectrum of the diamond Noddack ($5 \times 10^{16} \text{ e}^-/\text{cm}^2$, 1250°C anneal). The signal m_1/m_0 shows the deviation from maximum fluorescence when the MW drives an NV orientation at or near resonance. This data was taken when the static field was aligned to one NV class (outermost resonance pair) and triply degenerate with the other three classes (innermost pair). The applied MW power is set low to observe the hyperfine splitting of each resonance due to interaction with the ^{14}N nucleus.

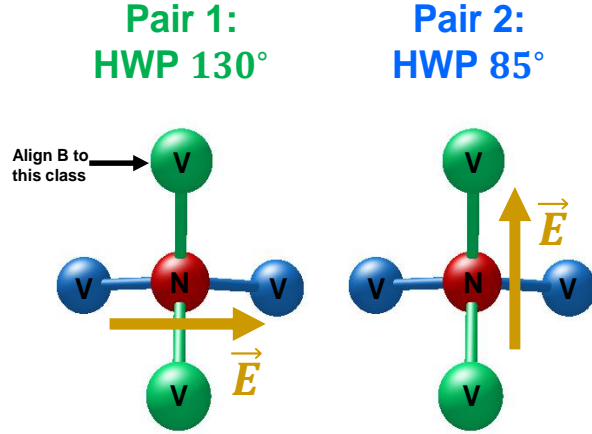


Figure C-4: The effect of laser polarization on NV class excitation. At one angle (130° with the axes set by the third HWP in the setup), the green-colored pair is maximally excited as the electric field is perpendicular to the NV axis. Rotating the HWP 45° in either direction maximally excites the other NV pair. Selectively exciting one pair over another aids in magnetic field alignment.

Since the laser has normal incidence on the diamond face, the polarization is in the same plane as the diamond face. Figure C-4 shows that when the electric field of the laser beam is in the orientation shown on the left, it preferentially excites one pair of NV classes since it is perpendicular the NV axis, while also minimally exciting the other pair of axes since it is mostly parallel to those axes. Rotating the third half-wave plate (HWP) (just before the dichroic mirror) in the experimental setup changes the laser polarization, which preferentially excites the other pair. Figure C-5 shows the CAW-ODMR spectrum at four different HWP angles. Around 850°C , one pair of NV classes is preferentially excited (shown by the large deviation in fluorescence), while around 130° , the other pair is preferentially excited. Going left to right in the figure, we denote the first and third NV resonance as pair 1 (preferentially excited at 85°), and the second and fourth as pair two (preferentially excited at 130°).

To align the field, first the NV classes in pair 2 are made degenerate with the static field by means of the translation stage. The resonances of both NV classes are recorded by fitting the resonance lineshapes to Lorentzians at four positions of the magnet on one axis of its translation stage. The intersection of these two lines yields the axis position that renders the two classes degenerate. Once the CW-ODMR signals from these two classes coincide (i.e.

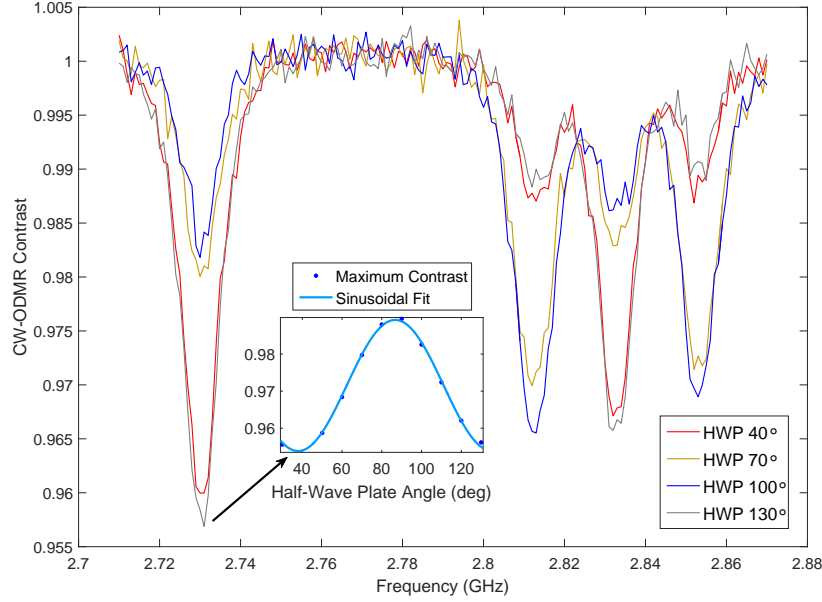


Figure C-5: CAW-ODMR spectrum of all four $|0\rangle \leftrightarrow |-1\rangle$ transitions for the diamond Hilbert ($5 \times 10^{15} \text{ e}^-/\text{cm}^2$, 1250°C anneal) for different half-wave plate angles. The magnetic field is mis-aligned here such that all four resonances are distinguishable. Inset: maximum deviation from the reference fluorescence of the left-most NV class as a function of the half-wave plate angle.

when the energy levels of the two NV classes are degenerate), the HWP is rotated 45° to maximally excite pair 1. The NV class in this pair that we are not aligning the magnetic field to is now made degenerate with the two NV classes in pair 2. When the resonances from the three non-desired NV classes overlap the field is aligned and anisotropic hyperfine coupling with the ^{13}C nuclei is eliminated. It should be noted that if the diamond were isotopically enhanced to remove the ^{13}C content, the alignment of the field would not be necessary for diamonds with ^{14}N .

C.3 Resonant Excitation and Field Projection

With the static magnetic field aligned to one NV class, we now only address this one orientation. To implement the measurement protocols for T_2^* , T_2 , and T_1 , we now measure both the resonance at which the fluorescence contrast is a maximum (to maximize signal-to-noise) and what MW pulse durations create specific NV spin states. To accomplish the first task, we

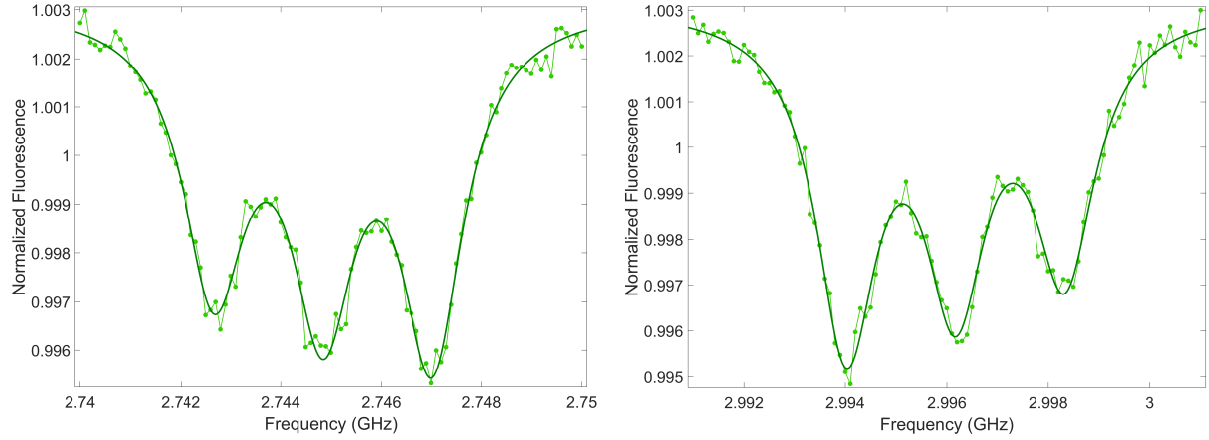


Figure C-6: CAW-ODMR spectra of the (left) $|0\rangle \leftrightarrow | - 1\rangle$ and (right) $|0\rangle \leftrightarrow |1\rangle$ electronic transitions for the diamond Ramon y Cajal ($1.6 \times 10^{18} \text{ e}^-/\text{cm}^2$, 850°C anneal). The three Lorentzian peaks arise from the hyperfine interaction with the ^{14}N nucleus, which can only be resolved when the NV ensemble is not power-broadened from the MW and optical drive. The slight polarization of the peaks closest to the zero-field splitting of 2.87 GHz arises from partial polarization of the nuclear spin.

take a high-resolution CAW-ODMR spectrum around the aligned NV's resonance for both electronic transitions. Figure C-6 shows CAW-ODMR spectra for both of these transitions, where each spectrum is fitted to a linear combination of three Lorentzians:

$$g(\nu) = A_0 + \frac{A_1}{(\nu - f - df)^2 + (\Gamma/2)^2} + \frac{A_2}{(\nu - f)^2 + (\Gamma/2)^2} + \frac{A_3}{(\nu - f + df)^2 + (\Gamma/2)^2}. \quad (\text{C.1})$$

Here $g(\nu)$ is the normalized CAW-ODMR signal, the A_i are amplitude fit parameters, $\nu = f$ is the resonance frequency of the central resonance, and df is the spacing between adjacent Lorentzians, usually 2 MHz for ^{14}N hyperfine-coupling (for ^{15}N only two Lorentzians fit the CAW-ODMR dip due to the spin-1/2 nature of the nucleus [82]). Both the lower resonance ν_- and higher resonance ν_+ are extracted, and from the Zeeman formula, the magnitude of the static field projection B_{\parallel} is calculated to zeroth order using

$$B_{\parallel} = \frac{\nu_+ - \nu_-}{2\gamma_{NV}}, \quad (\text{C.2})$$

where $\gamma_{NV} = 2.8 \text{ MHz/G}$ is the NV gyromagnetic ratio.

C.4 Rabi Oscillations

The pulse sequences used to measure the coherence time scales require different MW control pulses that need to be calibrated for duration. For measuring T_1 , for example, a MW π pulse is needed to rotate the NV spin from $|0\rangle$ to $|-1\rangle$. To measure the duration of this π pulse (and other control pulses for different measurement protocols), we fix the MW power and sweep the duration of an applied MW pulse. Figure C-7 (top) shows the pulse sequence used to measure population oscillations: after optical pumping, a resonant MW pulse of fixed power is applied for a variable time τ . During this time, the NV spin population precesses between the $|0\rangle$ state (low contrast) and $|-1\rangle$ state (high contrast). A readout laser pulse measures the fluorescence m_1 . The sequence is then repeated with no MW pulse to provide the reference signal m_0 . The fluorescence contrast, defined for this pulse sequence as m_1/m_0 , is then plotted against the MW pulse duration. The signal is eventually damped due to inhomogeneous broadening from coupling to the environment and from gradients in the MW field [37]. Figure C-7 (bottom) shows an example Rabi measurement for the diamond Bohr ($5 \times 10^{17} \text{ e}^-/\text{cm}^2$, 1250°C anneal). The shape of the curve is modelled as a sinusoidal function with a stretched exponential envelope:

$$g(\tau) = A_0 + A_1 e^{-(\tau/T_d)^p} \cos\left(\frac{2\pi}{T}(\tau - \tau_0)\right), \quad (\text{C.3})$$

where $g(\tau)$ is the fluorescence contrast, the A_i are amplitude and offset constants, p is an exponential stretch factor, T is the period of the oscillation, T_d is a decay time constant, and τ_0 is a phase shift. Theoretically, no phase shift is required for Rabi nutations; in this experiment, however, minor technical issues with the electronics resulted in an effective phase shift that was constant for all Rabi nutations measured for all diamonds.

To measure coherence times in this thesis we required three pulse times: a $\pi/2$ pulse that creates an equal superposition of the $|0\rangle$ and $|-1\rangle$ spin states, a π pulse that inverts the spin state from $|0\rangle$ to $|-1\rangle$, and a $3\pi/2$ pulse that creates another equal superposition state but with a different relative phase. These these times correspond to when the cosine has a phase of $\pi/2$, π , and $3\pi/2$ and we extract the times from the above fit. For the fluorescence signal in Figure C-7(b), the times are found to be $T_{\pi/2} = 12 \text{ ns}$, $T_\pi = 37 \text{ ns}$, and $T_{3\pi/2} = 61$

ns.

C.5 Polarization Time Optimization

We now turn to optimize the duration of optical pumping by the green laser. If the NV electronic spin is in the $|0\rangle$ state when excited by green light, it will fluoresce. If the spin is in $|\pm 1\rangle$, it will initially fluoresce less brightly, and any superposition of these two states will have an intermediate fluorescence [15]. Eventually the NV will be pumped and these signals converge into a steady state value. The duration of each applied green laser pulse is chosen to always repump the NV ensemble back to the $|0\rangle$ state. Figure C-8 (top) shows the pulse sequence used to determine the minimum re-pump time. After optically pumping the NV with a longer pulse duration that polarizes the spin, a resonant MW π pulse is applied followed by the re-pump laser pulse. After a variable time τ from the start of the re-pump pulse a fixed-length gate pulse measures the fluorescence m_1 . The sequence is repeated with no π pulse to measure fluorescence m_0 . Figure C-8 (bottom) shows the two fluorescence signals as a function of the gate pulse start time τ . The time where these two signals achieve the same steady state value is when the NV electronic spin is maximally polarized in the $|0\rangle$ state; this time serves as the minimum re-pump laser pulse duration.

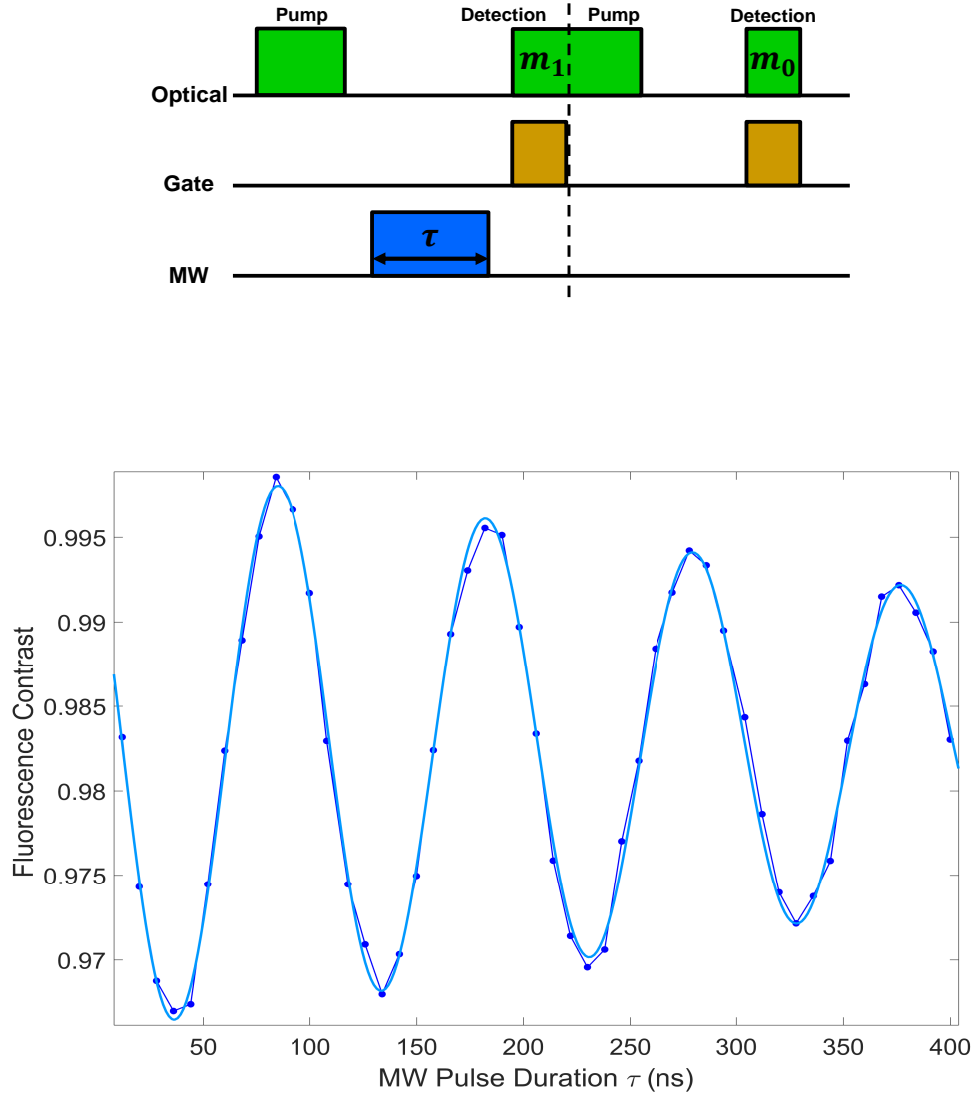


Figure C-7: Rabi nutation experiment. (top) Pulse sequence used to measure population oscillations under a resonantly applied MW field. (bottom) Fluorescence contrast m_1/m_0 as a function of MW pulse duration for the diamond Bohr ($5 \times 10^{17} \text{ e}^-/\text{cm}^2$, 1250°C anneal). The coherent population oscillations yield a sinusoidal fluorescence signal with a stretched exponential decay envelope.

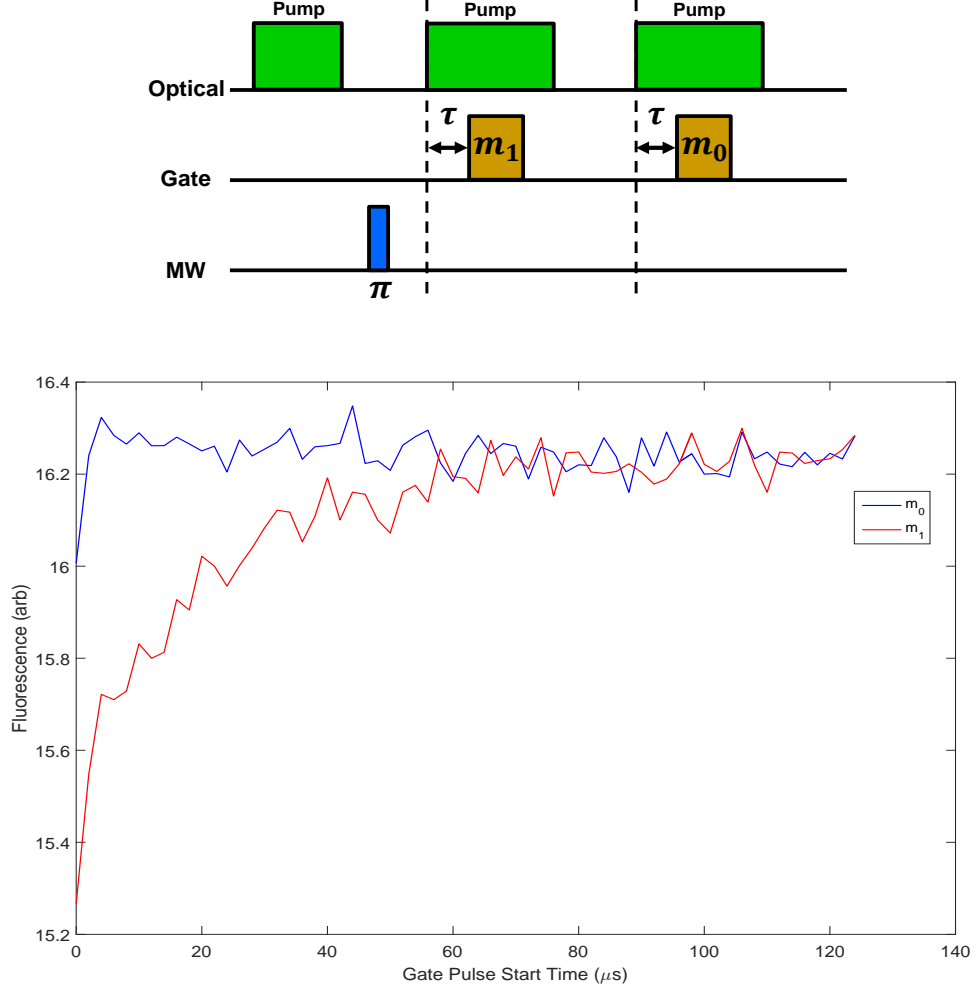


Figure C-8: Optical pumping pulse length determination (top) Pulse sequence used to measure the re-pump time necessary to optically polarize the NV into the $|0\rangle$ state. (bottom) Example signal from a pump measurement for the diamond Lorentz ($5 \times 10^{18} \text{ e}^-/\text{cm}^2$, 1250°C anneal). After optical pumping, a π pulse flips the spin population and a repump laser pulse is applied. After a time τ , the fixed-length gate pulse is turned on to measure the fluorescence m_1 . The sequence is repeated without the π pulse to give the signal m_0 . After sweeping the start time τ , the time after which both signals achieve their steady state values is chosen as the minimum duration of the repump pulse

Bibliography

- [1] M. V. Gurudev Dutt, L. Childress, L. Jiang, E. Togan, J. Maze, F. Jelezko, A. S. Zibrov, P. R. Hemmer, and M. D. Lukin. Quantum register based on individual electronic and nuclear spin qubits in diamond. *Science*, 316(5829):1312–1316, 2007.
- [2] J. B. Hewson. *A History of the Practice of Navigation*. Brown, Son and Ferguson Ltd, 1983.
- [3] H. Xia, A. Ben-Amar Baranga, D. Hoffman, and M. V. Romalis. Magnetoencephalography with an atomic magnetometer. *Applied Physics Letters*, 89(21):211104, 2006.
- [4] A. Jeffrey Spencer Tomasz Herbich. *Polish Archaeology in the Mediterranean XIX, Reports 2007*, chapter Tell El-Balamun Geophysical and Archaeological Survey, 20072008. Polish Centre of Mediterranean Archaeology, University of Warsaw 2010, 2010.
- [5] H. B. Dang, A. C. Maloof, and M. V. Romalis. Ultrahigh sensitivity magnetic field and magnetization measurements with an atomic magnetometer. *Applied Physics Letters*, 97(15):151110, 2010.
- [6] J. Maze, P. Stanwix, J. Hodges, S. Hong, J. Taylor, P. Cappellaro, L. Jiang, M. Gurudev Dutt, E. Togan, A. Zibrov, A. Yacoby, R. Walsworth, and M. Lukin. Nanoscale magnetic sensing with an individual electronic spin in diamond. *Nature*, 455(7213):644–647, 2008.
- [7] J. M. Taylor, L. Cappellaro, P. and Childress, L. Jiang, D. Budker, P. R. Hemmer, A. Yacoby, R. Walsworth, and M. D. Lukin. High-sensitivity diamond magnetometer with nanoscale resolution. *Nat Phys*, 4:810–816, Sep 2008.
- [8] Roger R. Fu, Benjamin P. Weiss, Eduardo A. Lima, Richard J. Harrison, Xue-Ning Bai, Steven J. Desch, Denton S. Ebel, Clément Suavet, Huapei Wang, David Glenn, David Le Sage, Takeshi Kasama, Ronald L. Walsworth, and Aaron T. Kuan. Solar nebula magnetic fields recorded in the semarkona meteorite. *Science*, 346(6213):1089–1092, 2014.
- [9] John F. Barry, Matthew J. Turner, Jennifer M. Schloss, David R. Glenn, Yuyu Song, Mikhail D. Lukin, Hongkun Park, and Ronald L. Walsworth. Optical magnetic detection of single-neuron action potentials using quantum defects in diamond. *Proceedings of the National Academy of Sciences*, 113(49):14133–14138, 2016.
- [10] A. M. Zaitsev. *Optical Properties of Diamond: a Data Handbook*. Springer-Verlag, first edition, 2001.

- [11] L. Du Preez. *Electron Paramagnetic Resonance and Optical Investigations of Defect Centers in Diamond*. PhD thesis, UNIVERSITY OF THE Witwatersrand, 1965.
- [12] C D Clark and C A Norris. Photoluminescence associated with the 1.673, 1.944 and 2.498 eV centres in diamond. *Journal of Physics C: Solid State Physics*, 4(14):2223, 1971.
- [13] G. Davies and M. F. Hamer. Optical studies of the 1.945 eV vibronic band in diamond. *Proceedings of the Royal Society of London A: Mathematical, Physical and Engineering Sciences*, 348(1653), 1976.
- [14] A. Gruber, A. Dräbenstedt, C. Tietz, L. Fleury, J. Wrachtrup, and C. von Borczyskowski. Scanning confocal optical microscopy and magnetic resonance on single defect centers. *Science*, 276(5321):2012–2014, 1997.
- [15] M. Doherty, N. Manson, P. Delaney, F. Jelezko, J. Wrachtrup, and L. Hollenberg. The nitrogen-vacancy colour centre in diamond. *Physics Reports*, 528(1):1 – 45, 2013. The nitrogen-vacancy colour centre in diamond.
- [16] J R Maze, A Gali, E Togan, Y Chu, A Trifonov, E Kaxiras, and M D Lukin. Properties of nitrogen-vacancy centers in diamond: the group theoretic approach. *New Journal of Physics*, 13(2):025025, 2011.
- [17] G. D. Fuchs, V. V. Dobrovitski, R. Hanson, A. Batra, C. D. Weis, T. Schenkel, and D. D. Awschalom. Excited-state spectroscopy using single spin manipulation in diamond. *Phys. Rev. Lett.*, 101:117601, Sep 2008.
- [18] L J Rogers, M W Doherty, M S J Barson, S Onoda, T Ohshima, and N B Manson. Singlet levels of the NV Λ centre in diamond. *New Journal of Physics*, 17(1):013048, 2015.
- [19] N. Aslam, G. Waldherr, P. Neumann, F. Jelezko, and J. Wrachtrup. Photo-induced ionization dynamics of the nitrogen vacancy defect in diamond investigated by single-shot charge state detection. *New Journal of Physics*, 15(1):013064, 2013.
- [20] A. Alkauskas, B. Buckley, D. Awschalom, and C. G. Van de Walle. First-principles theory of the luminescence lineshape for the triplet transition in diamond NV centres. *New Journal of Physics*, 16(7):073026, 2014.
- [21] J. E. Ralph. Radiation induced changes in the cathodoluminescence spectra of natural diamonds. *Proceedings of the Physical Society*, 76(5):688, 1960.
- [22] G. Davies. Dynamic Jahn-Teller distortions at trigonal optical centres in diamond. *Journal of Physics C: Solid State Physics*, 12(13):2551, 1979.
- [23] Y. Mita. Change of absorption spectra in type-IIb diamond with heavy neutron irradiation. *Phys. Rev. B*, 53:11360–11364, May 1996.

- [24] Alan T Collins. The fermi level in diamond. *Journal of Physics: Condensed Matter*, 14(14):3743, 2002.
- [25] S. Felton, A. M. Edmonds, M. E. Newton, P. M. Martineau, D. Fisher, and D. J. Twitchen. Electron paramagnetic resonance studies of the neutral nitrogen vacancy in diamond. *Phys. Rev. B*, 77:081201, Feb 2008.
- [26] G. Waldherr, J. Beck, M. Steiner, P. Neumann, A. Gali, Th. Frauenheim, F. Jelezko, and J. Wrachtrup. Dark states of single nitrogen-vacancy centers in diamond unraveled by single shot nmr. *Phys. Rev. Lett.*, 106:157601, Apr 2011.
- [27] X. Chen, C. Zou, F. Sun, and G. Guo. Optical manipulation of the charge state of nitrogen-vacancy center in diamond. *Applied Physics Letters*, 103(1):013112, 2013.
- [28] N. B. Manson, J. P. Harrison, and M. J. Sellars. Nitrogen-vacancy center in diamond: Model of the electronic structure and associated dynamics. *Phys. Rev. B*, 74:104303, Sep 2006.
- [29] A T Collins, M F Thomaz, and M I B Jorge. Luminescence decay time of the 1.945 ev centre in type ib diamond. *Journal of Physics C: Solid State Physics*, 16(11):2177, 1983.
- [30] A. Dréau, M. Lesik, L. Rondin, P. Spinicelli, O. Arcizet, J.-F. Roch, and V. Jacques. Avoiding power broadening in optically detected magnetic resonance of single nv defects for enhanced dc magnetic field sensitivity. *Phys. Rev. B*, 84:195204, Nov 2011.
- [31] D Budker, P. Kehayias, and K. Jensen. *High Sensitivity Magnetometers*, chapter 18: Magnetometry with Nitrogen-Vacancy Centers in Diamond. Springer Nature, 2017.
- [32] Linh My Pham. *Magnetic Field Sensing with Nitrogen-Vacancy Color Centers in Diamond*. PhD thesis, Harvard University, 2013.
- [33] L. M. Pham, N. Bar-Gill, C. Belthangady, D. Le Sage, P. Cappellaro, M. D. Lukin, A. Yacoby, and R. L. Walsworth. Enhanced solid-state multispin metrology using dynamical decoupling. *Phys. Rev. B*, 86:045214, Jul 2012.
- [34] H. Clevenson, M. Trusheim, C. Teale, D. Schroder, T. Braje, and D. Englund. Broad-band magnetometry and temperature sensing with a light-trapping diamond waveguide. *Nat Phys*, 11:393–397, Apr 2015.
- [35] V. M. Acosta, E. Bauch, M. P. Ledbetter, C. Santori, K.-M. C. Fu, P. E. Barclay, R. G. Beausoleil, H. Linget, J. F. Roch, F. Treussart, S. Chemerisov, W. Gawlik, and D. Budker. Diamonds with a high density of nitrogen-vacancy centers for magnetometry applications. *Phys. Rev. B*, 80:115202, Sep 2009.
- [36] C. E. Ashbaugh III. Gemstone irradiation and radioactivity. *Gems and Gemology*, 24(4):196–213, 1988.

- [37] R. Hanson, V. V. Dobrovitski, A. E. Feiguin, O. Gywat, and D. D. Awschalom. Coherent dynamics of a single spin interacting with an adjustable spin bath. *Science*, 320(5874):352–355, 2008.
- [38] T. Yamamoto, T. Umeda, K. Watanabe, S. Onoda, M. L. Markham, D. J. Twitchen, B. Naydenov, L. P. McGuinness, T. Teraji, S. Koizumi, F. Dolde, H. Fedder, J. Honert, J. Wrachtrup, T. Ohshima, F. Jelezko, and J. Isoya. Extending spin coherence times of diamond qubits by high-temperature annealing. *Phys. Rev. B*, 88:075206, Aug 2013.
- [39] F. P. Bundy, H. T. Hall, H. M. Strong, and R. H. Wentorf. Man-made diamonds. *Nature*, 176:51–55, July 1955.
- [40] F. P. Bundy, W. A. Bassett, M. S. Weathers, R. J. Hemley, H. K. Mao, and A. F. Goncharov. The pressure-temperature phase and transformation diagram for carbon; updated through 1994. *Carbon*, 34:141–153, January 1996.
- [41] M. Kamo, Y. Sato, S. Matsumoto, and N. Setaka. Diamond synthesis from gas phase in microwave plasma. *Journal of Crystal Growth*, 62(3):642 – 644, 1983.
- [42] J. Angus, H. Will, and W. Stanko. Growth of diamond seed crystals by vapor deposition. *Journal of Applied Physics*, 39(6):2915–2922, 1968.
- [43] G. Balasubramanian, P. Neumann, D. Twitchen, M. Markham, R. Kolesov, N. Mizuochi, J. Isoya, J. Achard, J. Beck, J. Tissler, V. Jacques, P. Hemmer, F. Jelezko, and J. Wrachtrup. Ultralong spin coherence time in isotopically engineered diamond. *Nat Mater*, 8:383–387, April 2009.
- [44] E. Kleinsasser, M. Stanfield, J. K. Q. Banks, Z. Zhu, W. Li, V. Acosta, H. Watanabe, K. Itoh, and K. C. Fu. High density nitrogen-vacancy sensing surface created via he+ ion implantation of 12c diamond. *Applied Physics Letters*, 108(20):202401, 2016.
- [45] R. M. Chrenko, H. M. Strong, and R. E. Tuft. Dispersed paramagnetic nitrogen content of large laboratory diamonds. *Philosophical Magazine*, 23(182):313–318, 1971.
- [46] R. Samlenski, C. Haug, R. Brenn, C. Wild, R. Locher, and P. Koidl. Characterisation and lattice location of nitrogen and boron in homoepitaxial cvd diamond. *Diamond and Related Materials*, 5(9):947 – 951, 1996.
- [47] I.I. Vlasov, V.G. Ralchenko, A.V. Khomich, S.V. Nistor, D. Shoemaker, and R.A. Khmel'nitskii. Relative abundance of single and vacancy-bonded substitutional nitrogen in cvd diamond. *physica status solidi (a)*, 181(1):83–90, 2000.
- [48] J. A. van Wyk, E. C. Reynhardt, G. L. High, and I. Kiflawi. The dependences of esr line widths and spin - spin relaxation times of single nitrogen defects on the concentration of nitrogen defects in diamond. *Journal of Physics D: Applied Physics*, 30(12):1790, 1997.
- [49] H. M. Strong and R. M. Chrenko. Diamond growth rates and physical properties of laboratory-made diamond. *The Journal of Physical Chemistry*, 75(12):1838–1843, 1971.

- [50] A. Secroun, A. Tallaire, J. Achard, G. Civrac, H. Schneider, and A. Gicquel. Photoconductive properties of lightly n-doped single crystal cvd diamond films. *Diamond and Related Materials*, 16, 2007. Proceedings of Diamond 2006, the 17th European Conference on Diamond, Diamond-Like Materials, Carbon Nanotubes, Nitrides and Silicon CarbideDiamond 2006.
- [51] T. Gaebel, M. Domhan, C. Wittmann, I. Popa, F. Jelezko, J. Rabeau, A. Greentree, S. Prawer, E. Trajkov, P.R. Hemmer, and J. Wrachtrup. Photochromism in single nitrogen-vacancy defect in diamond. *Applied Physics B*, 82(2):243–246, 2006.
- [52] B. Naydenov, F. Reinhard, A. Lämmle, V. Richter, R. Kalish, U. D’Haenens-Johansson, M. Newton, F. Jelezko, and J. Wrachtrup. Increasing the coherence time of single electron spins in diamond by high temperature annealing. *Applied Physics Letters*, 97(24):242511, 2010.
- [53] E. Kim, V. Acosta, E. Bauch, D. Budker, and P. Hemmer. Electron spin resonance shift and linewidth broadening of nitrogen-vacancy centers in diamond as a function of electron irradiation dose. *Applied Physics Letters*, 101(8):082410, 2012.
- [54] A. M. Edmonds, U. F. S. D’Haenens-Johansson, R. J. Cruddace, M. E. Newton, K.-M. C. Fu, C. Santori, R. G. Beausoleil, D. J. Twitchen, and M. L. Markham. Production of oriented nitrogen-vacancy color centers in synthetic diamond. *Phys. Rev. B*, 86:035201, Jul 2012.
- [55] J. Lomer and A. Wild. Electron spin resonance in electron irradiated diamond annealed to high temperatures. *Radiation Effects*, 17(1-2):37–44, 1973.
- [56] D. J. Twitchen, D. C. Hunt, M. E. Newton, J. M. Baker, T. R. Anthony, and W. F. Banholzer. Electron paramagnetic resonance (epr) and optical absorption studies of defects created in diamond by electron irradiation damage at 100 and 350 k. *Physica B: Condensed Matter*, pages 628 – 631, 1999.
- [57] B. Campbell and A. Mainwood. Radiation damage of diamond by electron and gamma irradiation. *physica status solidi (a)*, 181(1):99–107, 2000.
- [58] B. Campbell, W. Choudhury, A. Mainwood, M. Newton, and G. Davies. Lattice damage caused by the irradiation of diamond. *Nuclear Instruments and Methods in Physics Research Section A: Accelerators, Spectrometers, Detectors and Associated Equipment*, 476(3):680 – 685, 2002. Proc. of the 3rd Int. Conf. on Radiation Effects on Semiconductor Materials, Detectors and Devices.
- [59] M. A. Lobaev, A. M. Gorbachev, S. A. Bogdanov, A. L. Vikharev, D. B. Radishev, V. A. Isaev, V. V. Chernov, and M. N. Drozdov. Influence of cvd diamond growth conditions on nitrogen incorporation. *Diamond and Related Materials*, 72:1 – 6, 2017.
- [60] J. Koike, D. M. Parkin, and T. E. Mitchell. Displacement threshold energy for type iia diamond. *Applied Physics Letters*, 60(12):1450–1452, 1992.

- [61] G. Davies, S. Lawson, A. Collins, A. Mainwood, and S. Sharp. Vacancy-related centers in diamond. *Phys. Rev. B*, 46:13157–13170, Nov 1992.
- [62] A. C. Frangeskou, A. T. M. A. Rahman, L. Gines, S. Mandal, O. A. Williams, P. F. Barker, and G. W. Morley. Optical levitation of high purity nanodiamonds in vacuum without heating. *ArXiv e-prints*, August 2016.
- [63] S. Felton, B. L. Cann, A. M. Edmonds, S. Liggins, R. J. Cruddace, M. E. Newton, D. Fisher, and J. M. Baker. Electron paramagnetic resonance studies of nitrogen interstitial defects in diamond. *Journal of Physics: Condensed Matter*, 21(36):364212, 2009.
- [64] N.B. Manson and J.P. Harrison. Photo-ionization of the nitrogen-vacancy center in diamond. *Diamond and Related Materials*, 14(10):1705 – 1710, 2005.
- [65] S. Karaveli, O. Gaathon, A. Wolcott, R. Sakakibara, O. A. Shemesh, D.. Peterka, E. Boyden, J. Owen, R. Yuste, and D. Englund. Modulation of nitrogen vacancy charge state and fluorescence in nanodiamonds using electrochemical potential. *Proceedings of the National Academy of Sciences*, 113(15):3938–3943, 2016.
- [66] D. Farfurnik, N. Alfasi, S. Masis, Y. Kauffmann, E. Farchi, Y. Romach, Y. Hovav, E. Buks, and N. Bar-Gill. Enhanced concentrations of nitrogen-vacancy centers in diamond through TEM irradiation. *ArXiv e-prints*, February 2017.
- [67] J. Clarke and F. Wilhelm. Superconducting quantum bits. *Nature*, 453(20):1031–1042, 2008.
- [68] L Rondin, J-P Tetienne, T Hingant, J-F Roch, P Maletinsky, and V Jacques. Magnetometry with nitrogen-vacancy defects in diamond. *Reports on Progress in Physics*, 77(5):056503, 2014.
- [69] K. Fang, V.. Acosta, C. Santori, Z. Huang, K. M. Itoh, H. Watanabe, S. Shikata, and R. Beausoleil. High-sensitivity magnetometry based on quantum beats in diamond nitrogen-vacancy centers. *Phys. Rev. Lett.*, 110:130802, Mar 2013.
- [70] V. M. Acosta, E. Bauch, M. P. Ledbetter, A. Waxman, L.-S. Bouchard, and D. Budker. Temperature dependence of the nitrogen-vacancy magnetic resonance in diamond. *Phys. Rev. Lett.*, 104:070801, Feb 2010.
- [71] L. Childress, M. V. Gurudev Dutt, J. M. Taylor, A. S. Zibrov, F. Jelezko, J. Wrachtrup, P. R. Hemmer, and M. D. Lukin. Coherent dynamics of coupled electron and nuclear spin qubits in diamond. *Science*, 314(5797):281–285, 2006.
- [72] J. R. Maze, J. M. Taylor, and M. D. Lukin. Electron spin decoherence of single nitrogen-vacancy defects in diamond. *Phys. Rev. B*, 78:094303, Sep 2008.
- [73] P. L. Stanwix, L. M. Pham, J. R. Maze, D. Le Sage, T. K. Yeung, P. Cappellaro, P. R. Hemmer, A. Yacoby, M. D. Lukin, and R. L. Walsworth. Coherence of nitrogen-vacancy electronic spin ensembles in diamond. *Phys. Rev. B*, 82:201201, Nov 2010.

- [74] R. De Sousa. *Electron Spin Resonance and Related Phenomena in Low-Dimensional Structures*, chapter Electron Spin as a Spectrometer of Nuclear-Spin Noise and Other Fluctuations. Springer-Verlag Berlin Heidelberg, 2009.
- [75] A. Laraoui, F. Dolde, C. Burk, F. Reinhard, J. Wrachtrup, and C. Meriles. High-resolution correlation spectroscopy of ^{13}C spins near a nitrogen-vacancy centre in diamond. *Nature Communications*, 4, April 2013.
- [76] R. J. Epstein, F. M. Mendoza, Y. K. Kato, and D. D. Awschalom. Anisotropic interactions of a single spin and dark-spin spectroscopy in diamond. *Nat Phys*, 1:94–98, Nov 2005.
- [77] B. E. A. Saleh and M. C. Teich. *Fundamentals of Photonics*. John Wiley and Sons, Inc., second edition, 2007.
- [78] T. Wolf, P. Neumann, K. Nakamura, H. Sumiya, T. Ohshima, J. Isoya, and J. Wrachtrup. Subpicotesla diamond magnetometry. *Phys. Rev. X*, 5:041001, Oct 2015.
- [79] Jacques B. and G. Walker. Modal noise in high-resolution, fiber-fed spectra: A study and simple cure. *Publications of the Astronomical Society of the Pacific*, 113(785):851, 2001.
- [80] J. R. Taylor. *An Introduction to Error Analysis: the Studies of Uncertainties in Physical Measurements*, chapter Least-Squares Fitting. University Science Books, second edition, 1982.
- [81] L. T. Hall, J. H. Cole, and L. C. L. Hollenberg. Analytic solutions to the central-spin problem for nitrogen-vacancy centers in diamond. *Phys. Rev. B*, 90:075201, Aug 2014.
- [82] V. Jacques, P. Neumann, J. Beck, M. Markham, D. Twitchen, J. Meijer, F. Kaiser, G. Balasubramanian, F. Jelezko, and J. Wrachtrup. Dynamic polarization of single nuclear spins by optical pumping of nitrogen-vacancy color centers in diamond at room temperature. *Phys. Rev. Lett.*, 102:057403, Feb 2009.